UNIVERSITY OF CALIFORNIA SAN DIEGO

The Design of Mechanical Metamaterials for Nonlinear-Elastic Functional Structures and Surface Morphing

A Dissertation submitted in partial satisfaction of the requirements
for the degree Doctor of Philosophy

in

Materials Science and Engineering

by

Yujin Park

Committee in charge:

Professor Kenneth J. Loh, Chair
Professor Nicholas Boechler
Professor Shengqiang Cai
Professor Samuel Ward

2023

The Dissertation of Yujin Park is approved, and it is acceptable in quality and form for publication on microfilm and electronically.

University of California San Diego

2023

DEDICATION

This dissertation is dedicated to my family, and friends.

Thank you for your endless guidance and support.

TABLE OF CONTENTS

LIST OF FIGURES

LIST OF TABLES

LIST OF ABBREVIATIONS

2D	Two-dimensional
3D	Three-dimensional
FE	Finite Element
FDM	Fused Deposition Modeling
TPU	Thermoplastic Polyurethane
σ^{PK2}	The Second Piola-Kirchhoff Stress Tensor
Ψ_{mec}	The Helmholtz free energy density
λ_i	Principal Stretch
σ_i	Cauchy Stress Tensor
σ^{PK1}	The First Piola-Kirchhoff Stress Tensor
F	The deformation Gradient
I_1, I_2, I_3	The First, Second, and Third invariants
G	Gauge Length of Tensile Specimen
$L1$	Length of the Narrow Section of Tensile Specimen
$L2$	Length Overall of Tensile Specimen
D	Distance between Grips of Tensile Specimen
$W1$	Width of the Narrow Section of Tensile Specimen
$W2$	Width Overall of Tensile Specimen
$R1$	Radius of the Fillet of Tensile Specimen
$R2$	Outer Radius of Tensile Specimen
σ	Stress
λ	Stretch

LAS	Lateral Ankle Sprains
AFO	Ankle-Foot Orthosis
PLA	Polylactic Acid
ATFL	Anterior Talofibular Ligament
PTFL	Posterior Talofibular Ligament
CFL	Calcaneofibular Ligament
a	Side Length of Hexagon Metamaterial
w	Width of Hexagon Metamaterial
t	Thickness of Hexagon Metamaterial
d	Length of the Hexagon Meet
n	The Number of Hexagon Layers
ε_{th}	Strain Threshold
ε_{Max}	Strain at the Maximum Stiffness Point
SMA	Shape Memory Alloy
SMP	Shape Memory Polymer
SRP	Stimuli-Responsive Polymer
w_{BIAS}	Width of BIAS geometry
θ	Rig Angle of BIAS geometry
t_{BIAS}	Thickness of BIAS geometry
l	Length of the Slender Beam of BIAS geometry
DBS	Distance between Sepal Tips
DBP	Distance between Petal Tips
F_{cr}	Critical Force on the Slender Beam of BIAS geometry

P_{cr}	Critical Load
D_{cr}	Critical Displacement
n_1, n_2	Length of the Notch
h_1, h_2	Depth of the Notch
MOB	Man Overboard
SAR	Search and Rescue
WSN	Wireless Sensor Networks
RF	Radio Frequency
PNIPAM	poly(N-isopropylacrylamide)
NIPAM	N-isopropyl acrylamide
MBA	N-N'methylenebisacrylamide
w_{STAR}	Width of Active Skin with Five Tips
PDMS	Polydimethylsiloxane
UV	Ultraviolet
PVA	Polyvinyl alcohol

ACKNOWLEDGEMENTS

I would like to express my deepest gratitude to Professor Kenneth J. Loh for providing me with the incredible opportunity to conduct research and for consistently believing in my abilities throughout my time at UCSD. Without his assistance, I would not have been able to pursue my studies far away from home. As my advisor, he has consistently provided me with necessary guidance and support, even during challenging times, enabling me to grow into the scholar I am today. I am truly grateful for his mentorship and teachings, which have equipped me to venture into a broader world of knowledge.

I would also like to express my deep appreciation to Dr. Amy Slider, John J. Fraser, and Dr. Pinata Sessoms at the Naval Health Research Center. Their guidance and expertise in the field of biomechanics were instrumental in helping me comprehend the intricacies of the subject and conduct all the necessary biomechanical tests for the development of adaptive ankle braces. Their unwavering support and collaboration have been invaluable throughout my research journey.

I cannot express enough gratitude for the friendship and support I received from my friends at UCSD. Yening Shu, Hanjoo Lee, Morgan Funderburk, Gianmarco Vella, Shih-Chao Huang, Bomi Lee, Sijia Li, Taylor Pierce, Elijah Wyckoff, Yun-An Lin, Emerson Noble, Ting-Ya Chang, Vishnu Naidu, Sumit Gupta, Xinlun Zhao, Chih-Yen Wang, Prithviraj Desai, and Adam Kreutter, you all have been instrumental in making my time at UCSD memorable and fulfilling. Also, thank you so much for being my subjects and incredible friends, and I cherish the moments we have shared together.

Chapter 2, in part, is a reprint of the material as it appears in MRS Advances 2020, Park, Yujin; Loh, Kenneth J., Materials Research Society, 2020, and has been submitted for publication of the material as it may appear in Journal of Materials, 2023, Park, Yujin; Loh, Kenneth J. The dissertation author was the primary researcher and author of this paper.

Chapter 3, in full, is currently being prepared for submission for publication of the material. Park, Yujin; Zhao, Xinlun; Slider, Amy; Sessoms, Pinata; Fraser, John J., and Loh, Kenneth J. The dissertation author was the primary researcher and author of this material.

Chapter 4, in part, is a reprint of the material as it appears in MRS Advances 2020, Park, Yujin; Loh, Kenneth J., Materials Research Society, 2020, and has been submitted for publication of the material as it may appear in Journal of Materials, 2023, Park, Yujin; Loh, Kenneth J. The dissertation author was the primary researcher and author of this paper.

Chapter 5, in part has been submitted for International Workshop on Structural Health Monitoring (IWSHM) 2023, Naidu, Vishnu; Park, Yujin; Loh, Kenneth J. and currently being prepared for submission for publication of the material. Park, Yujin; Loh, Kenneth J. The dissertation author was the primary researcher and author of this material.

VITA

2015 Bachelor of Science, Pusan National University

2018 Master of Science, Pusan National University

2022 Doctor of Philosophy, University of California San Diego

PUBLICATIONS

1. Park, Y., Zhao, Y., Slider, A., Sessoms, P., Fraser, J. J., Loh, K. J. (2022) Variable Stiffness Honeycomb Metamaterials for Adaptive Ankle Brace Design, Structural Health Monitoring 2021, 36268

2. Funderburk, M. L., Park, Y., & Loh, K. J. (2022). Piezoelectric Rod Sensors for Scour Detection and Vortex-Induced Vibration Monitoring. *Structural Health Monitoring*, 21(3): 1031-1045

3. Park, Y., Loh, K. J. (2021). Controlling 3D Deformations of Bio-inspired Active Skins through Designed Geometrical Imperfections. *Proceedings of SPIE*, 1158906 (Chosen as one of the finalists for SPIE Best Student Paper)

4. Lin, Y. A., Zhao, Y., Wang, L., Park, Y., Yeh, Y. J., Chiang, W. H., & Loh, K. J. (2021). Graphene K-Tape Meshes for Densely Distributed Human Motion Monitoring. *Advanced Materials Technologies,* 6(1), 2000861

5. Park, Y., & Loh, K. J. (2020). Surface Morphing of Geometrically Patterned Active Skins. *MRS Advances*, 5(14-15), 743-750.

6. Park, Y., Loh, K. J. (2020). Active Metamaterial Skins for Friction Coefficient Control. *In TMS 2020 149th Annual Meeting & Exhibition Supplemental Proceedings*, 889-895.

7. Park, Y., Vella, G., & Loh, K. J. (2019). Bio-inspired Active Skins for Surface Morphing. *Scientific Reports*, 9(1), 1-10.

8. Park, Y., Vella, G., Loh, K. J. (2019). Active Metamaterial Skins for Actuation and Gripping, *Proceedings of the 14th International Workshop on Advanced Smart Materials and Smart Structures Technology (ANCRiSST)*

ABSTRACT OF THE DISSERTATION

The Design of Mechanical Metamaterials for Nonlinear-Elastic Functional Structures and Surface Morphing

by

Yujin Park

Doctor of Philosophy in Materials Science and Engineering

University of California San Diego, 2023

Professor Kenneth J. Loh, Chair

The overarching goal of this dissertation is to exploit the free-hinging motion of mechanism-based, flexible, mechanical metamaterials for designing (1) nonlinear-elastic functional structures and (2) shape morphing. Although there have been many attempts to achieve those unique behaviors by manipulating the chemical composition or microstructure of

materials, these approaches are only applicable to a certain class of materials. Meanwhile, mechanical metamaterials exhibit unique behaviors, such as negative Poisson's ratio or swelling ratio, by harnessing the free-hinging motion and response to mechanical forces (*i.e.,* buckling, snapping, or rotation) of slender elements in their unit cell geometry. In that regard, the goal of this dissertation is to design and control the unit cell geometry of mechanical metamaterials so that they can exhibit unique mechanical behavior without having to modify their chemical composition or microstructure.

First, adaptive stiffness metamaterial structures were designed and incorporated in elastic fabric to form next-generation ankle braces so that they enable free movement during low-intensity activities and provide significant biomechanical support during high-intensity activities. Current ankle braces that provide too much support to prevent lateral ankle sprains or reinjury are effective but uncomfortable during normal gait. On the other hand, braces that do not sufficiently support the ankle are comfortable but ineffective. The proposed adaptive stiffness metamaterials, instead, mimic the nonlinear mechanical properties of human ligaments and could provide both comfort and biomechanical support during different intensities of biomechanical movements, which was achieved using their nonlinear-elastic stress-strain properties. To begin, the nonlinear behavior of lateral ankle movements and inversion was investigated through optical motion capture biomechanical and BIODEX tests to identify the strained range and directions around the malleolus during inversion. Adaptive stiffness metamaterials in the form of patterned two dimensional geometries were designed to replicate the nonlinear behavior around the malleolus through parametric optimization. The designed hexagon geometry exhibited load-free shape change like how ligaments behave under low intensity activities until the diagonal elements fully straightened. Thereafter, the straightened elements engaged to bear loads with the

material being strained, which resulted in rapid stiffness increase to provide significantly higher biomechanical support during high-intensity activities. The effectiveness of the adaptive stiffness prototype brace was validated through BIODEX tests, and in comparison with other commercial braces.

Second, the design principles for these structures to exhibit two-dimensional (2D) to three-dimensional (3D) morphable behavior when subjected to uniaxial strains were established. Currently, the most common approach is to rely on heterogeneous composite materials and that their anisotropic properties can induce surface morphing. Instead, in this work, the localized compression generated from the free-hinging motion of a re-entrant auxetic geometry was used as a driving force to induce surface morphing in the form of out-of-plane deformations. The geometry was optimized to increase the instability of the geometry, which could lower the critical stress and strain for out-of-plane buckling. In addition, geometrical imperfections were introduced to facilitate controlled surface morphing, inducing programming buckling direction and selective deformations. The lower critical stress and strain also meant that shape morphing could be achieved using soft actuation methods such as pneumatic actuators or stimuli-responsive polymers. To demonstrate this concept, a temperature-responsive nanocomposite hydrogel was integrated with the designed geometries to demonstrate temperature-induced 2D-to-3D shape morphing (and sensing). Overall, this design principle validated that surface morphing could be achieved with a single material and without using anisotropic properties of composite materials. Moreover, this method could be extended to various configurations using other re-entrant auxetic geometries.

In summary, the significance of this thesis is that geometrical design enabled the material to attain unique advanced behaviors such as nonlinear elasticity and shape morphing. First,

adaptive stiffness metamaterials that behave like human ligaments (*i.e.,* nonlinear-elastic mechanical behavior) was achieved by designing patterned planar structures with embedded free-hinging motion mechanisms. Prototype ankle braces with these embedded metamaterials were designed to exhibit low-stiffness at low-strains before transitioning to high-stiffness at higher-strains. The strain threshold for which stiffness dramatically increases could be precisely designed by tuning the geometric parameters of these materials. The magnitude of the strain threshold is dependent on the ankle region where biomechanical support is needed and was determined from human participant ankle studies. Overall, these metamaterials could be designed to fit any biomechanical brace that require nonlinear elastic supports. Second, the free-hinging motion of a reentrant auxetic geometry was impregnated with designed imperfections to facilitate and control shape morphing response (*i.e.,* patterned out-of-plane deformations) when subjected to in-plane strains. This work is unique because it overcame the limitation of large-arrayed traditional mechanical materials that exhibit unpredictable behavior. The designed imperfections controlled their shape morphing response against external stimuli and made them resistant to manufacturing errors or other load perturbation. In addition, reducing the critical stress and strain enabled the geometry to be actuated through various actuation methods. Overall, these metamaterials could be architected to make exotic 3D configurations using a single elastic material.

CHAPTER 1: Introduction

Metamaterials have revolutionized material science by offering a new approach to designing materials with exceptional properties that are not found in nature. Unlike traditional materials science, which focuses on the properties of natural structures such as chemical composition, microstructures, and macroscopic features, metamaterials use artificially designed structures to create unique and unnatural properties. These structures are designed to yield desired properties, such as invisibility, suppression or amplification of acoustic waves, or a negative refractive index, by manipulating optical, acoustic, thermal, and mechanical fields. This approach paves the way for material creation by controlling atomic composition alone [105]. One example of the unique capabilities of metamaterials is their ability to manipulate the electromagnetic propagation of light, allowing objects to be concealed. A unit cell manipulating electromagnetic waves can create an invisible cloak around an object.

Mechanical metamaterials are a subset of metamaterials that exploit motion, deformations, stresses, and mechanical energy to achieve advanced functionalities, such as zero or negative material parameters, shape morphing, topological protection, instabilities, and nonlinear response. The unit cell geometry of mechanical metamaterial consists of slender elements prone to elastic instabilities [10]. The advanced functionalities are obtained from the deformation, rotation, buckling, folding, and snapping of these elements in response to mechanical forces. It is, therefore, important to consider the nonlinearities and instabilities generated by these slender elements to predict advanced functionalities.

Auxetic materials are an early example of the advanced functionality of mechanical metamaterials. The elastic property of these materials is characterized by Poisson's ratio, which

is the ratio of transverse strain to corresponding axial strain on a material when subjected to uniaxial stress. Most existing materials have a positive Poisson's ratio, nearly 0.33, while hyperelastic materials have a ratio of about 0.5 [61]. Auxetic metamaterials, however, have a negative Poisson's ratio. In other words, they expand under tension and shrink under compression. These materials have received much attention due to their unusual mechanical responses, such as dome-shaped curvature, enhanced indentation resistance, fracture toughness, and vibration damping, as well as their dramatic porosity when subjected to stretch. This dissertation introduces various metamaterial design principles to create new functionalities.

1.1 Mechanism-based metamaterials

Mechanism-based metamaterials use rigid elements connected by flexible hinges in response to external forces [10]. This design strategy leverages the mechanism of planar, spherical, or spatial rigid elements connected by flexible hinges to enable auxetic behavior, deployable structures, extreme stretchability, and even shape-transforming art. The mechanics of mechanism-based metamaterials are designed from linked elements to control the arbitrarily complex motion, with low-energy deformations assumed to be similar to the free motion of the underlying mechanism [22]. There are three primary metamaterials that leverage this design strategy to harvest exotic functions: origami-inspired metamaterials, Kirigami-inspired metamaterials, and flexible mechanism-based metamaterials.

1.2 Origami-inspired metamaterials

Origami is a design technique inspired by Japanese paper art that creates unique shape-transforming designs. Origami-inspired metamaterials are compact-folded thin sheets of interconnected 2D facets with fold lines, or creases, based on preconceived crease patterns like Miura-ori structure [5; 7; 62; 68], the square twist [50] and the box-pleat tiling [101]. Once the material is subjected to mechanical forces, the deformation occurs only at creases while the facets remain in 2D [34].

Origami-inspired metamaterials have two major objectives: to create novel reconfigurable and deployable systems by piling up these folded layers [97] or incorporating them in tubes [19; 35], and to develop multi-functional adaptive systems on various scales from nano- to macro-structures [16; 62; 68; 69; 103]. These materials have a wide range of applications, including deployable space structures such as antennas and solar panels [43; 80; 97; 133], flexible electronics that can be folded, bent, and twisted [103], flexible medical stents by changing their radius [94], and foldable telescope lenses [41]. In addition, the Miura-ori pattern has even been modified for thick materials using mathematical modeling to enable rigid-foldability [133]. Moreover, it can be developed into a 3D cellular structure that can be deformed uniformly by stacking 2D Miura-ori layers [97].

1.3 Kirigami-inspired metamaterials

Kirigami originated from a Japanese paper art form that utilizes its cut geometrical features to induce out-of-plane buckling without shearing or stretching the individual units. Kirigami-inspired materials exhibit auxetic behavior with zero or negative Poisson's ratio, allowing manipulation of elastic properties, and attaining large

strains and shape changes [10]. This design strategy has been applied to adjust the elasticity of stiff nanomaterials like graphene [99] and to develop stretchable and wearable electronics [32; 104; 122; 125], as well as soft robotics actuators [65; 92].

The most peculiar feature of Kirigami-inspired metamaterials is their ability to provide stretchability beyond the normal material's deformative while maintaining other features. For instance, the ultimate strain of Kirgami pattern induced rigid graphene sheets can be increased from 4 to 370% [99]. The flexibility of wearable sensors with Kirigami-inspired patterns can conformally follow the contour of curved surfaces [32; 104; 122; 125], while soft actuators with Kirigami-inspired skin can achieve reversible and deployable 3D features [65; 92]. In addition, the out-of-plane deformation of Kirigami-inspired metamaterials offers a promising way to create complex 3D surface morphing structures[18; 52; 81].

1.4 Soft instability-based metamaterials

The building block of the soft mechanism-based metamaterial consists of flexible hinges that allow for free-hinging motion and slender elements that rotate, buckle, or snap during the deformation. The hinges are soft and flexible, which means that the metamaterial can undergo significant structural deformation, even under low mechanical forces. Depending on how the hinges and slender elements are arranged, the unit cell of the metamaterial will display specific spatial structures when subjected to mechanical forces. These structures determine the metamaterial's functionalities, such as 2D and 3D auxetic properties and shape-shifting.

These materials are susceptible to elastic instabilities such as buckling and snapping, which allow for large deformations in response to small forces. As a result, the unit cell displays geometrical nonlinearities in macroscopic stresses and strains, regardless of the linearity of the materials. Instability-based metamaterials fall into three categories: buckling-based metamaterials, snapping-induced metamaterials, and programmable metamaterials, corresponding to the induced instabilities. Among them, buckling-induced metamaterials have gained significant attention because of their repeatable and reversible instabilities exhibited with elastic materials. Buckling refers to the sudden change in shape that occurs when a material is subjected to uniaxial compression that exceeds its capacity to withstand the applied forces. When compressed, the series of slender beams buckle homogeneously and return to their pristine state when the stress is removed.

The re-entrant geometry is a prominent example of a buckling-induced metamaterial. A re-entrant angle is an angle greater than 180° but smaller than 360° and is typically found in concave polygons. Unlike regular convex geometry, which exhibits in-plane isotropy, re-entrant geometry is highly anisotropic [74], meaning that it has different properties depending on the direction in which it is measured. For instance, re-entrant hexagonal geometry provides higher transverse elastic and shear moduli than regular hexagonal geometry. The mechanical properties of re-entrant geometry are determined by various geometrical parameters, such as rib angle, rib thickness, and slenderness ratio of linked elements [2; 15; 96].

There are several re-entrant auxetic structures, including the bowtie, arrowhead, star, lozenge grid, and square grid [59]. The re-entrant bowtie geometry is one of the

most studied auxetic geometries and offers nonlinear large deformation. It is used for meshes in stents, scaffolds, sports safety equipment, and sensors. Another well-known geometry is the re-entrant star, which is used as static inclusions in modeling fiber-reinforced honeycomb composites [111] and in dynamic studies for wave propagation [107], band gap [77], and acoustic super-lens design [17]. Moreover, the symmetrical configuration of re-entrant geometries allows for volumetric deformation and simplifies numerical modeling [17].

1.5 Research objective and dissertation outline

The objective of this dissertation is to design and control the unit cell geometry of mechanical metamaterials so that they can exhibit unique mechanical behaviors such as (1) nonlinearly elastic functional structures and (2) shape morphing without having to modify their chemical composition or microstructure. Chapter 2 introduces the experimentally calibrated finite element methods to design and optimize the unit cell geometries. Chapter 3 combines biomechanical testing methods and a hexagon geometry to develop an adaptive stiffness ankle brace. Chapter 4 leverages the star re-entrant geometry to design the bio-inspired active skin (BIAS) that exhibits 2D to 3D deformation under uniaxial tension. Chapter 5 demonstrates the versatility of designed BIAS geometry by showing the potential application of unit cell in soft robotics, pattern embedding and passive antenna tag. The overall study shows the potential capability of preconceived metamaterial design principles by extending and combining them to achieve various objectives.

CHAPTER 2: Mooney-Rivlin Hyperelastic Model

In this chapter, the theoretical foundation is described to predict the behavior of designed metamaterial geometries. A finite element (FE) model was created to investigate the deformation mechanism and stress distributions within the designed unit cell geometries when subjected to mechanical forces. Each designed geometry in this dissertation was fabricated using a fused deposition modelling (FDM) 3D printer. Thermoplastic polyurethane (TPU) 95A filament was used to print the design layer by layer. Unlike conventional bulk materials, the properties of 3D-printed samples largely depend on their fabrication parameters. Therefore, this necessitates determining the mechanical properties of 3D-printed TPU.

2.1 Mooney-Rivlin Model

The FE modeling in this dissertation adopted the Mooney-Rivlin model under uniaxial tension, considering five material parameters to describe the mechanical behavior of the TPU. The TPU material was assumed to be incompressible and hyperelastic, meaning that its volume remains constant during deformation, and it exhibits a nonlinear stress-strain relationship.

In the context of hyperelasticity, the Helmholtz free energy is a fundamental measure of the internal energy within a material system. It encompasses both thermal energy and mechanical strain energy. However, for the specific Mooney-Rivlin model

utilized in this study, the thermal energy part was neglected, given that the focus was solely on the mechanical strain behavior of the material.

To understand the internal stress distribution within the TPU material after deformation, the second Piola-Kirchhoff stress tensor (σ^{PK2}) was utilized. This tensor describes the internal stress state within the material. Obtaining the value of σ^{PK2} involves taking the derivative of the mechanical strain part of the Helmholtz free energy density (Ψ_{mec}) with respect to the elastic part (E^{el}) as following equation:

$$\sigma^{PK2} = \frac{\partial \Psi_{mec}}{\partial E^{el}} \quad (2\text{-}1)$$

Using principal stretch (λ_i), σ^{PK2} can be expressed as:

$$\sigma^{PK2} = \frac{\partial \Psi_{mec}}{\partial \lambda_i} \frac{\partial \lambda_i}{\partial E_i^{el}} = \frac{1}{\lambda_i} \frac{\partial \Psi_{mec}}{\partial \lambda_i} \quad (2\text{-}2)$$

The Cauchy stress tensor (σ_i) represents the true stress in a material at a specific location and time. The internal forces within the material can be calculated using σ_i. The first Piola-Kirchoff stress tensor (σ^{PK1}) gives information about a measure of stress in reference or undeformed configuration. Thus, σ_i and σ^{PK1} can be obtained by applying the deformation gradient (F) to σ^{PK2} as following equation:

$$\sigma_i = JF^{-T}\sigma^{PK2}F^{-1} \quad (2\text{-}3)$$

$$\sigma^{PK1} = F\sigma^{PK2} \quad (2\text{-}4)$$

Where *J* is the volume ratio. Under the assumption of incompressibility, *J* was always equal to 1. The principal stretch under uniaxial strain can be calculated as following equation:

$$\lambda = \lambda_1 = 1 + \varepsilon \quad (2\text{-}5)$$

$$\lambda_1\lambda_2\lambda_3 = 1 \quad (2\text{-}6)$$

$$\lambda_2 = \lambda_3 = \frac{1}{\sqrt{\lambda}} \quad (2\text{-}7)$$

The deformation gradient (*F*) is given by

$$F = \begin{pmatrix} \lambda & 0 & 0 \\ 0 & \frac{1}{\sqrt{\lambda}} & 0 \\ 0 & 0 & \frac{1}{\sqrt{\lambda}} \end{pmatrix} \quad (2\text{-}8)$$

Using the equation (2-1), (2-2), and (2-6), σ_i and σ^{PK1}can be expressed as:

$$\sigma_1 = \lambda^2 \sigma_1^{PK2} \quad (2\text{-}9)$$

$$\sigma^{PK1} = \lambda \sigma_1^{PK2} \quad (2\text{-}10)$$

Invariants provide a concise and coordinate-independent representation of the deformation state of the material. The invariants are the product of the deformation gradient tensor with its transpose. Using invariants allows for the formulation of constitutive equations that are invariant under coordinate transformations, ensuring the model's validity regardless of the choice of coordinate system. The first invariant (I_1) represents the trace of the deformation gradient tensor and provides information about the volumetric changes of the material. It is related to the relative change in volume or the dilatation of the material. The second invariant (I_2) is related to the square of the stretch ratios and provides information about the distortion or stretching of material elements in different directions. The third invariant (I_3) is related to the determinant of the deformation gradient tensor and represents the change in orientation or rotation of material elements. Each invariant can be expressed as:

$$I_1 = \lambda_1^2 + \lambda_2^2 + \lambda_3^2 \quad (2\text{-}11)$$

$$I_2 = \lambda_1^2 \lambda_2^2 + \lambda_2^2 \lambda_3^2 + \lambda_3^2 \lambda_1^2 \quad (2\text{-}12)$$

$$I_3 = \lambda_1^2 \lambda_2^2 \lambda_3^2 = J^2 \quad (2\text{-}13)$$

Using equation (2-3) and (2-5), each invariant under uniaxial tension can be expressed in terms of λ as:

$$I_{1,uni} = \left(\lambda^2 + \frac{2}{\sqrt{\lambda}}\right) \quad (2\text{-}14)$$

$$I_{2,uni} = \left(2\lambda + \frac{1}{\lambda^2}\right) \quad (2\text{-}15)$$

$$I_{3,uni} = 1 \quad (2\text{-}16)$$

The strain energy density for Mooney-Rivlin five-parameters model can be expressed as:

$$\Psi_{\text{mec}} = C_{10}(\bar{I}_1 - 3) + C_{01}(\bar{I}_2 - 3) + C_{20}(\bar{I}_1 - 3)^2 + C_{11}(\bar{I}_1 - 3)(\bar{I}_2 - 3) + C_{02}(\bar{I}_2 - 3)^2 \quad (2\text{-}17)$$

Using equation (2-2) and (2-9), σ can be expressed as:

$$\sigma_1 = \lambda_1^2 \sigma_1^{PK2} = \lambda_1 \frac{\partial \Psi_{mec}}{\partial \lambda_1} \quad (2\text{-}18)$$

$$\sigma_1 = \lambda_1 \left(\frac{\partial \Psi_{mec}}{\partial I_1} \frac{\partial \mathrm{I}_1}{\partial \lambda_1} + \frac{\partial \Psi_{mec}}{\partial I_2} \frac{\partial \mathrm{I}_2}{\partial \lambda_1} + \frac{\partial \Psi_{mec}}{\partial J} \frac{\partial J}{\partial \lambda_1} \right) \quad (2\text{-}19)$$

σ^{PK1} can be expressed as:

$$\sigma^{\mathrm{PK1}} = 2(1 - \lambda^{-3})(\lambda C_{10} + 2C_{20}\lambda(I_1 - 3)$$
$$+C_{11}\lambda(I_2 - 3) + C_{01} + 2C_{02}(I_2 - 3) + C_{11}(I_1 - 3)) \quad (2\text{-}20)$$

2.2 Experimental Procedure

2.2.1 Fabrication of tensile test specimens

TPU tensile test specimens, in accordance with the ASTM D638-16 Type IV standard [45], were 3D-printed to obtain their actual material parameters for the FE simulations (Figure 2.1a). The specimen features the following dimensions: gauge length (*G*) = 25 mm, length of the narrow section (*L1*) = 33 mm, the distance between grips (*D*) = 65 mm, length overall (*L2*) = 115 mm, the width of the narrow section (*W1*) = 6 mm, width overall (*W2*) = 19 mm, a radius of the fillet (*R1*) = 14 mm, and outer radius (*R2*) = 25 mm. The thickness of the specimen was 1 mm, as recommended thickness for a Type IV specimen is 4 mm or less. An example of the 3D-printed tensile test coupon is shown in Figure 2.1b.

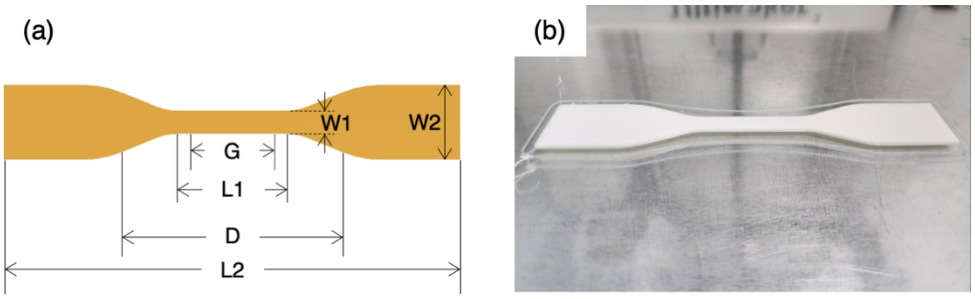

Figure 2.1: (a) Rendering of a tensile test specimen conformed to ASTM D638-16 Type IV standard, which is specifically intended for testing nonrigid plastic, is illustrated. (b) 3D-printed tensile test specimen is displayed.

2.2.2 Tensile tests

3D-printed tensile test specimens were subjected to uniaxial tensile tests conducted using a Test Resources 150R electromechanical load frame. The tensile test specimens were strained to 400%. In accordance with the ASTM D638-16 standard [45], Type IV samples should be subjected to strain rates of 0.2 min^{-1}, 2 min^{-1}, or 20 min^{-1}. In this dissertation, the strain rate was fixed at 0.2 min^{-1} to minimize the strain hardening effect of TPU. It allowed gradual application of force, ensuring that the material had adequate time to undergo deformation without rapidly hardening. Rapid strain rates can introduce abrupt force, making the material quickly resist deformation, which can exacerbate the hardening effect. The test was repeated five times, and samples used once were discarded.

2.3 Results and discussion

2.3.1 Nonlinear least-squares fit (TPU)

To derive the Mooney-Rivlin five parameters for TPU, the nonlinear least square method was applied to the stress-stretch profile obtained from tensile tests.

Initially, the circular points in Figure 2.2 depict the stress-stretch graph recorded after subjecting the tensile sample to tension. All five tensile tests exhibited little variation, and the value displayed in Figure 2.2 represents the median of these results. This profile was applied to equation (2-20) using the nonlinear-least fitting method. The results are displayed as a solid line in Figure 2.2, and the five derived parameters are listed in Table 2-1. These material parameters were subsequently incorporated into the COMSOL FE modeling process to delve

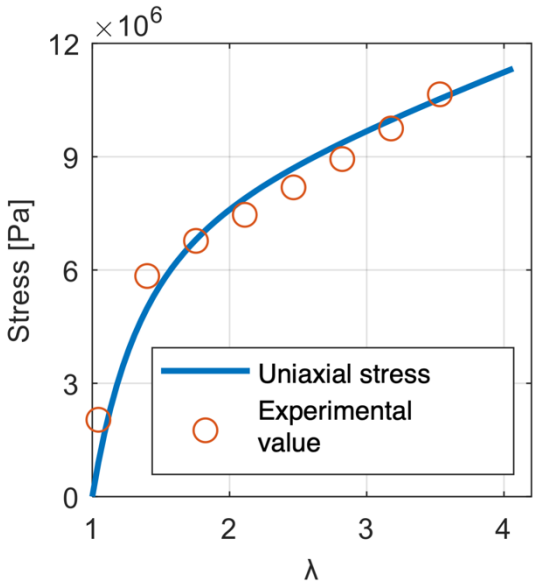

Figure 2.2: Stress (σ) and stretch (λ) from experimental data and fitted Mooney-Rivlin model of 3D printed TPU coupon are compared.

Table 2-1: Mooney-Rivlin Parameters of 3D-printed TPU

C_{01} [MPa]	C_{10} [MPa]	C_{11} [MPa]	C_{02} [MPa]	C_{20} [MPa]	Density [kg/m^3]
34.08	-23.94	-2.88	10.93	0.54	1179

deeper into the deformation mechanisms of the metamaterials discussed in this dissertation.

Furthermore, to validate the appropriateness of these parameters for FE modeling, the stress-stretch obtained from tensile test FE modeling using these parameters was compared with experimental results and depicted in Figure 2.3. While both values closely aligned in the elastic region, differences became more pronounced as they entered the plastic region. This is because the strain hardening effect was neglected in the model. Since the TPU in this dissertation was anticipated to undergo strain only within the elastic deformation range, it was proper to use the obtained parameters in the FE modeling.

Chapter 2, in part, is a reprint of the material as it appears in MRS Advances 2020, Park, Yujin; Loh, Kenneth J., Materials Research Society, 2020, and has been submitted for publication of the material as it may appear in Journal of Materials, 2023, Park, Yujin; Loh, Kenneth J. The dissertation author was the primary researcher and author of this paper.

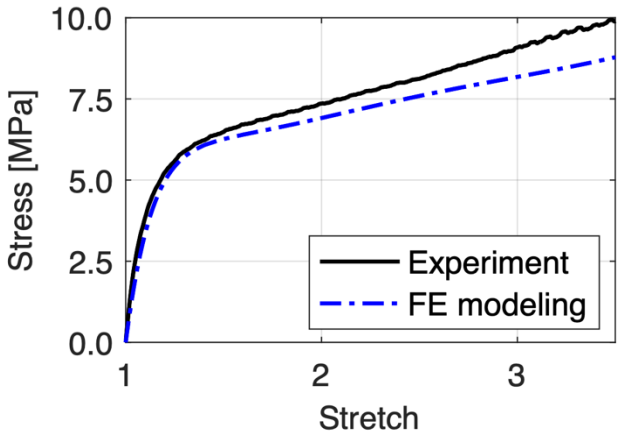

Figure 2.3: Stress-stretch response of TPU tensile samples were obtained from both experiment and FE modelling.

CHAPTER 3: Nonlinear Adaptive Stiffness Structures

3.1 Introduction

Lateral ankle sprains (LAS) are the most common lower-intensity musculoskeletal injury, particularly in individuals who engage in physical activity and sports [117]. LAS affects more than 25,000 individuals daily in the United States and has been reported as the highest trauma case to emergency departments [28], corresponding to a rate of 2.17 injuries per 1000 person-years [9; 116]. It substantially burdens on military service members who undergo significant physical demands and perform functions in diverse environments [93]. More specifically, LAS accounts for the highest musculoskeletal injuries among conventional and special warfare combatants [67; 110]. The prevalence of ankle sprains in military services is 5 to 8 times higher than that reported in the civilian population [14], ranging from 12.6 per 1000 person-years in male military officers to 34.6 per 1000 person-years in female enlisted members [38].

Up to 40% of individuals who have sustained LAS experienced persistent sequelae such as instability [28; 46], giving-way episodes, and recurring sprains within two weeks to eight years after the first injury, often referred to as chronic ankle instability [37; 93]. 78% of patients with chronic ankle instability have experienced functional limitations like ankle-joint degeneration and post-traumatic osteoarthritis that impoverish their long-term health-related consequences [70; 113; 115]. LAS is associated with a high recurrence rate and risk of developing chronic ankle instability, a significant cause of time loss during active military service [14]. In addition, direct loss from LAS ranges from one to three months of workdays with a healthcare burden of up to $8,000 per injury [46].

Biomechanical LAS involves excessive inversion and internal rotation generated from high-velocity supination of the ankle-foot complex [37]. The minimum inversion angle required to cause LAS varies depending on the inversion severity; however, less than 30º of inversion is typically considered safe and ethical [48]. Lateral ligamentous damage is typical following inversion injury [130]. Approximately 40% of inversion sprains involve microscopic, partial, or complete injury to the anterior talofibular ligaments (ATFL) [37]. The treatment for LAS includes immobilization to decrease swelling and pain and prevent additional damage [21], followed by remobilization to recover the full functional capacities of the ankle [75].

Functional supports, such as braces, tape, or pneumatic walking boots, are suggested to avoid further injury and pain during weight bearing. Most clinical practice guidelines recommend using functional supports that allow progressive weight-bearing on the lower limb, protecting the damaged tissues to encourage healing [130]. The use of an ankle brace shows the most remarkable effects in terms of ankle immobilization and recurrence rate compared with other types of functional supports [33]. For example, it has been demonstrated that non-rigid bracing prevented recurrent of ankle sprains, mainly when the risk of sprains decreased by 50% to 70% among people with a history of ankle sprain [76].

The effectiveness of functional supports has been demonstrated during risky activities like parachute jumps, basketball, or soccer [82]. Most ankle braces can be categorized as one of the following three brace designs: sleeves, lace-ups, or stirrups. Sleeve braces made of soft materials are comfortable and provide soft compression; however, they cannot adequately protect the ankle. On the other hand, lace-up and stirrup

braces made of rigid materials provide additional inversion and eversion control and have been widely adopted as prophylactic braces for first-time sprains and recurrent sprains for risky activities. However, for athletics and soldiers who need to perform dynamic activities, these types of ankle braces compromise compliance and can reduce their performance. Furthermore, limiting the ankle's range of motion stabilize the ankle joint; however, the load placed on the knee and hip joints is inadvertently increased, potentially leading to injuries to these joints. Therefore, a brace that can assist the nonlinear behavior of ankle inversion that allows movement in the low range of motion while restricting the ankle during the high range of motion could address the problem.

The ankle's response during inversion, especially external behavior, is crucial to design nonlinear adaptive ankle brace since ankle braces protect the ankle from the outside of the foot. Many existing studies have analyzed the nonlinear response of the ankle joint, including the dynamics of joint mobility [12; 37], muscle [118], tendon [102], and ligament [39; 100; 108]. In particular, these studies have focused on the strain-dependent nonlinear behavior of the ligaments, particularly in the area surrounding the malleolus where damage is concentrated.

The stress-strain curve of ligaments exhibits a toe region that easily deforms at low strains and then displays adaptive stiffness behavior with increased stiffness once the strain threshold is reached [112]. As a result, the ankle demonstrates unrestricted movement at a low range of motion while restricted movement at a high range of motion. Although there is considerable research on ligaments themselves, there is limited analysis available on the ankle's external nonlinear behavior, especially in the malleolus region where damage is most likely to occur.

Therefore, the objective of this work was to design the adaptive stiffness ankle brace to improve comfort level while providing sufficient support during low- and high-intensity activities. First, the nonlinear behavior of lateral ankle movements and an inversion was investigated through BIODEX multi-joint system and an optical motion capture system. BIODEX tests were performed to identify the directions yielding the large torque during the inversion and decide the location of supporting materials. The optical motion capture system measured the strain range during 0 to 30º of inversion to replicate the nonlinear behavior of the lateral ankle. Then adaptive stiffness metamaterial mimicking the corresponding mechanical properties was engineered via proper material selection and geometrical optimization. The prototype ankle braces allowed normal physiological movement during function; however, they had adequate mechanical support at the extremes of motion and likely exhibited greater compliance during wear.

3.2 Materials and Methods

3.2.1 Foot model and sample fabrication

Ankle-foot orthosis (AFO) model was used for the BIODEX multi-joint system to demonstrate the direction yielding the largest torque near the malleolus during inversion. First, the subject's lower right leg was scanned to manufacture a 3D-printed AFO using a Mark II structure sensor connected to the 3DFitMe application. The subject was assisted to stand in a neutral position. The scanned file was saved as an OBJ file, then uploaded in Autodesk Fusion 360 to modify the design, as shown in Figure 3.1a. The AFO model's ankle joint part was removed, dividing the AFO into foot and tibia parts. The ball joint was integrated

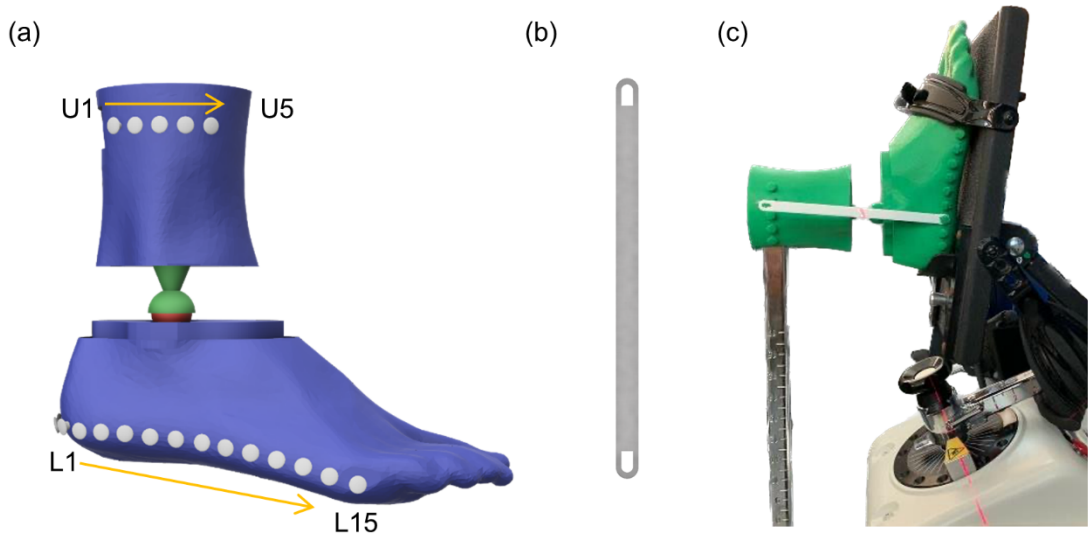

Figure 3.1: Rendering of (a) AFO model and (b) bridging coupon is illustrated. (c) 3d-printed AFO model was affixed on BIODEX multi-joint system.

with the AFO model to connect the foot and tibia models. A rectangular groove was created on the upper back of the tibia model to fix it well on the BIODEX machine without a strap. Furthermore, five buttons were placed on the tibia and 15 on the foot to attach the rectangular-shaped bridging coupon (see Figure 3.1b). Bridging coupons were designed to be fixed to the opposite side of the tibia or foot by connecting them to the buttons at different angles, as depicted in Figure 3.1c. The length matched the distance between the buttons, while the thickness and width were affixed at 2 mm and 10 mm, respectively. In addition, the hexagon geometries and prototype coupon with various geometrical parameters were designed in Autodesk Fusion 360 as well.

The AFO model and the coupons were exported as an STL mesh and sliced in Cura 6.1 for 3D printing. They were 3D-printed using Ultimaker 3+ FDM 3D printer. The AFO model was 3D printed using polylactic acid (PLA)

filament at 215 ℃ with an infill density of 50% and a line pattern infill geometry. The layer thickness used for printing was 0.3 mm. TPU 95A filament was used for bridging and hexagon geometry coupons. The printing temperature was 230 ℃, and the printing speed was 10 mm/sec.

3.2.2 BIODEX tests with the AFO model

The 3D-printed AFO model with the bridging coupon was fixed on the testing machine. As the tibia model was shorter than the actual length of a human leg and could not be secured by straps alone, a rectangular bar was inserted into the groove to secure it in place (see Figure 3.1c). The ankle's axis of rotation was aligned with the dynamometer shaft and strapped on the footplate. The tibia and foot models were connected with a TPU rectangular-shaped bridging coupon of the corresponding length. The testing speeds were set as 300º/sec, and the range of motion was 50º of inversion to 50º of eversion, which cannot be tested on humans. Each measurement was repeated five times.

3.2.3 BIODEX tests with human

BIODEX test was performed on human to demonstrate the effectiveness of the prototype ankle brace. During each session, participants were advised to wear comfortable training/workout clothing on the day of testing. During each session, participants were asked to sit on the positioning chair. Their leg was secured in the limb support with the foot on the footplate to align the ankle axis of rotation with the dynamometer shaft. Torque measurements were taken with

participants wearing no brace, prototype, and commercial braces. The testing speeds were set as 30, 60, 90, 150, and 300º/sec and repeated 10 times. The range of motion was increased within the range that participants felt comfortable with, from a minimum of 30º of inversion to 20º of eversion.

3.2.4 Motion capture test

Strains around lateral ankles during inversion were recorded using a 10-camera Vicon video-based motion capture system with a sampling frequency of 960 Hz. Participants were advised to wear shorts/leggings and no socks on the day of testing. During the experiment, each subject had seven retroreflective markers attached to each foot, one additional marker on their right leg, and two additional markers on their left leg to differentiate between the left and right sides (see Figure 3.2a). One marker was placed on the malleolus, and six markers were placed around it: three on the posterior talofibular ligament (PTFL), calcaneofibular ligament (CFL), and ATFL directions, one perpendicular to the ground (heel pad), one towards the fifth metatarsal, and one on the tarsometatarsal.

The markers attached above the ligaments were positioned according to the anatomy of the lateral ankle [108]. Specifically, they were attached at an angle of approximately 25º with respect to the horizontal plane for the ATFL and 40º for the CFL. The PTFL was oriented in a nearly horizontal plane. Subjects were instructed to march five times on the ground to neutralize their ankle position

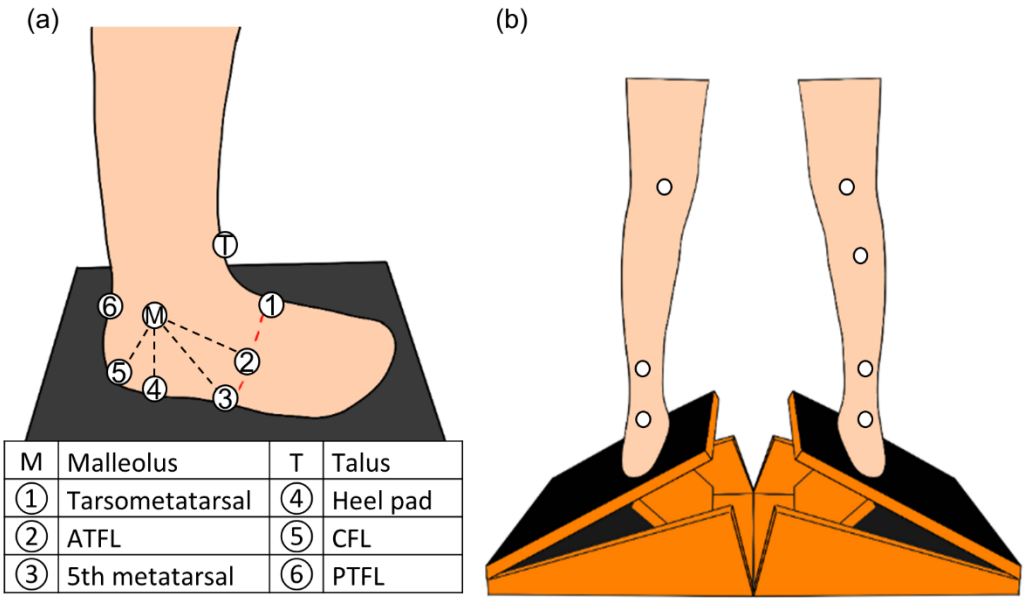

M	Malleolus	T	Talus
①	Tarsometatarsal	④	Heel pad
②	ATFL	⑤	CFL
③	5th metatarsal	⑥	PTFL

Figure 3.2: Location of markers on (a) lateral ankle and (b) legs are illustrated. The location of each marker is labelled with number.

before standing on inclined boards for measurements (Figure 3.2b). In addition, two force plates were installed underneath each board and connected to a monitoring system, providing real-time feedback of the forces on the left and right sides to ensure balance during the measurements. Each marker's location was recorded as the board increased from 0 to 30º for inversion. Then, subjects were instructed to walk freely. Each measurement was five times repeated. The measured data was post-processed after recording using Vicon Nexus 2.12. Markers were labeled, and marker trajectories were filtered using a Woltring filter (max gap length = 20) and fourth-order low pass Butterworth (cut-off frequency = 6 Hz). Then, post-processing for the strain was conducted using MATLAB.

3.2.5 Numerical modeling

Experimentally calibrated FE simulations were performed using COMSOL Multiphysics to predict the adaptive stiffness of the hexagon geometry when loaded. Mooney-Rivlin's five parameters of TPU are shown in Table 2-1. The load-displacement relationship was obtained by subjecting uniaxial tension on hexagon geometries with various geometrical parameters using Mooney-Rivlin parameters. The quadratic tetrahedral elements were used to mesh the hexagon geometries with a minimum element size of 0.1 mm and a maximum element size of 0.5 mm. Furthermore, the average element quality of mesh was always over 0.5 to ensure regularity of the mesh element's shape and avoid inverted mesh elements.

The load-displacement response of the geometries obtained through FE simulation was imported to MATLAB to obtain the end of the region and maximum stiffness of the geometry. The end of the toe region was obtained with 98% accuracy through linear regression, and maximum slope was calculated after the toe region.

3.3 Nonlinear behavior of lateral ankle

3.3.1 Strain direction around lateral ankle

The BIODEX multi-joint system was employed to identify the direction that produced the highest torque during the inversion. A 3D-printed AFO model was used for the test since the testing range of motion was 50º of inversion to 50º

of eversion, which exceeds the human ankle's general range of motion. The AFO model is based on a scanned image of an actual human foot with a ball joint on the talus to simulate the ankle's movement. In addition, buttons were printed on the lateral side of each foot and tibia of the AFO model to affix a TPU bridging coupon, which allowed the measuring of torque generated in the direction the coupon was connected during inversion and eversion movement.

In total, 15 buttons were printed on the foot model, and five buttons were printed on the tibia model with a distance of 2 cm between each button. The buttons on the foot model were initially placed vertically down from the malleolus, then positioned towards the heel of the fifth metatarsal. The button on the heel is labeled as L1, and the button on the fifth metatarsal is labeled as L15, as shown in Figure 3.1. Similarly, the buttons on the tibia model were first placed vertically above the malleolus, then positioned towards the Achilles tendon (U1) or tibia (U5). The bridging coupon was connected to the buttons overlaying the center of rotation as depicted in Figure 3.3, which are U1-L15, U1-L13, U1-L11, U1-L9, U3-L7, U5-L5, U5-L3, and U5-L1, with a length equivalent to the distance between each button.

Figure 3.4 displays the inversion torque generated from each bridging coupon. Regardless of direction, torque started to occur when inversion exceeded 30º and the value was greater than 10 Nm. The largest peak torque at inversion is shown in Figure 3.5, which reveals that the bridging coupons connected to U5-L3, U3-L7, and U1-L11 generated the greatest torque. U5-L3 and U1-L11 correspond to the positions of the CFL and ATFL ligaments, which easily being damaged

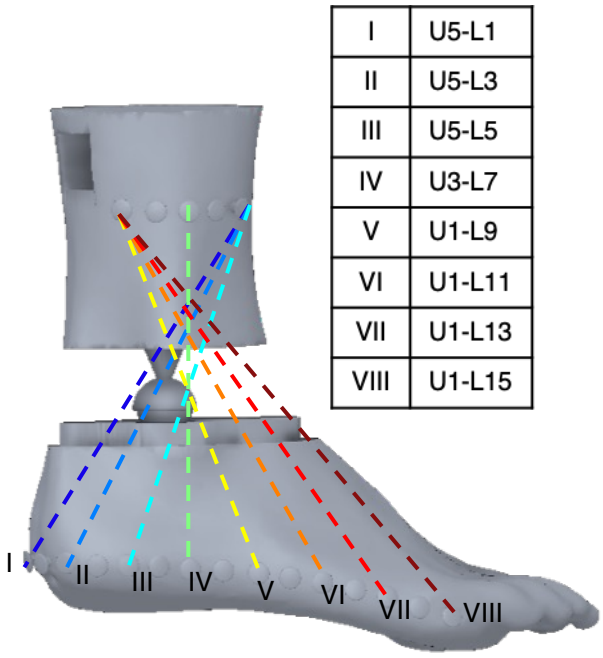

I	U5-L1
II	U5-L3
III	U5-L5
IV	U3-L7
V	U1-L9
VI	U1-L11
VII	U1-L13
VIII	U1-L15

Figure 3.3: Each line represents the pair of buttons where the bridging coupon was connected.

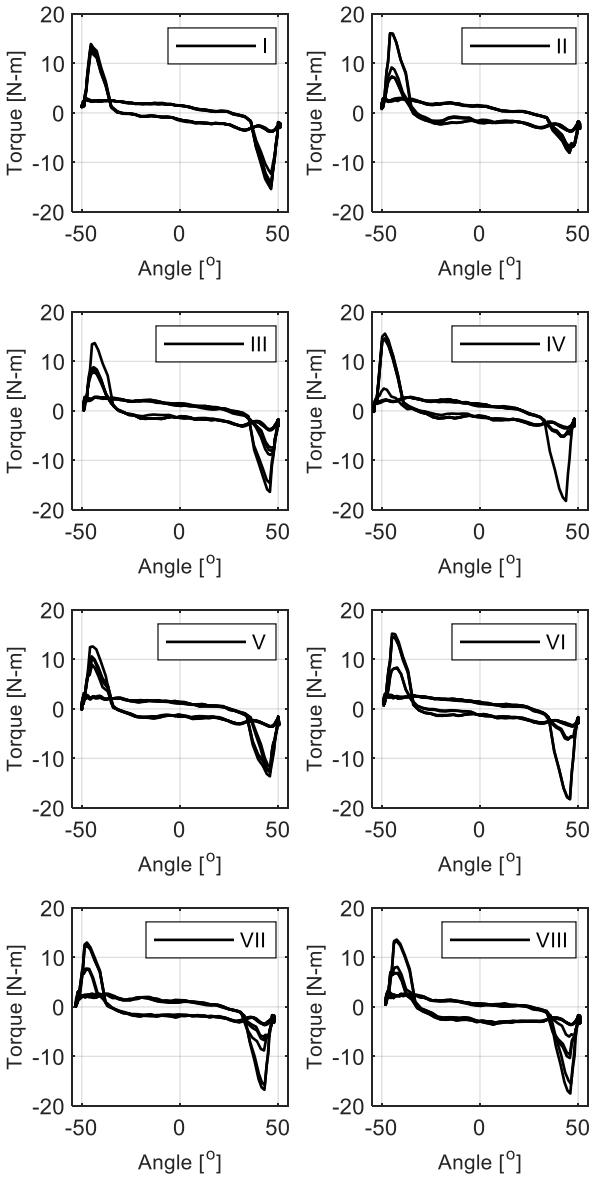

Figure 3.4: The torque generated during inversion when bridging coupon was attached to each pair of buttons is presented.

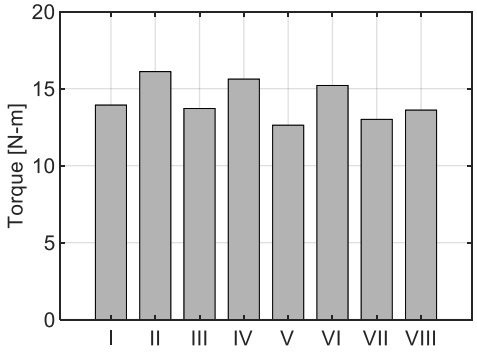

Figure 3.5: Maximum torque generated during inversion at corresponding directions is illustrated.

after LAS, and U3-L7 is the fulcrum of inversion, where high strain occurs, respectively.

3.3.2 Strain threshold around lateral ankle

Next, to determine the strain threshold at which the brace would allow free movement, the external strain on the lateral ankle during inversion was measured using a motion capture system. Ten participants were measured while standing on the ground and on an inclined board at 15º to 30º. The average strain between the malleolus and each marker was calculated using the distance between them, and the minimum and maximum values were also illustrated in Figure 3.6.

There was little variation of strain in the malleolus to PTFL and tarsometatarsal. On the other hand, the strain was observed in the malleolus to vulnerable ligaments, ATFL and CFL, where large torques were generated. The ATFL was strained by approximately 7% at 15º and up to 13% at 30º of

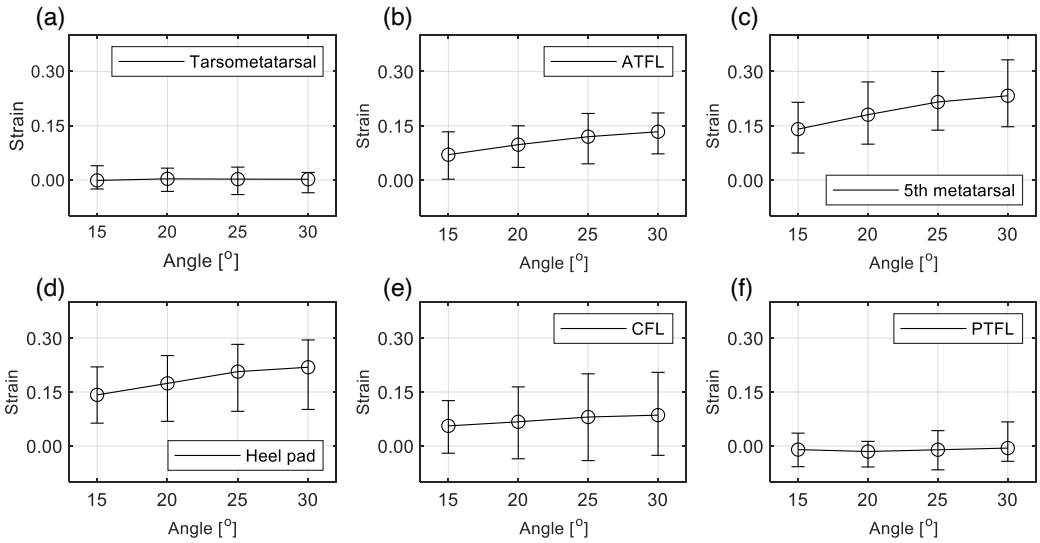

Figure 3.6: The average strains between malleolus to each marker at corresponding angle are presented. The baseline length was measured at the ground.

inversion, while CFL was strained less by approximately 5% at 15º and 8% at 30º of inversion. This corresponds with other studies that have shown that the toe region of the ATFL is longer than that of the CFL in low ranges of motion. The area with the most strain during inversion was in the direction of the fifth metatarsal and heel pad, which is the fulcrum of inversion, resulting in a large strain. Both of these areas showed approximately 15% strain at 15º and up to 23% strain at 30º of inversion. When examining the four directions with the most strain, it was observed that the degree of strain increased steadily up to approximately 25º of inversion but then increased less sharply from 25º to 30º of inversion. In other words, as the ankle's inversion angle approaches its maximum capacity to resist, the brace that allowed free movement needs to reach maximum stiffness at 25º to protect the ankle.

To summarize, the BIODEX and motion capture systems were used to identify the parts of the lateral ankle that require support in certain directions and determine the corresponding strain thresholds for unrestricted movement. Three directions that yielded large torque need support during inversion, especially direction towards two ligaments would need stiffer support after unrestricted movement. Although the heel pad direction did not yield large torque during BIODEX tests, supporting material would still be placed to control the strain since it was strained more than the ligament directions. Three different adaptive stiffness metamaterials would be designed as following: maximum stiffness at 8%, strong support for CFL, maximum stiffness at 12%, strong support for ATFL, maximum stiffness at 20%, mild support for heel pad and fifth metatarsal.

3.4 Design of adaptive stiffness metamaterial

3.4.1 Design principle of adaptive stiffness metamaterial

The principle of free-hinge motion of flexible mechanical metamaterials was leveraged to design adaptive stiffness metamaterial geometry. Mechanical metamaterials consist of slender elements, and their connection points act like free hinge when mechanical metamaterial geometry is fabricated with flexible materials like TPU. Unlike traditional solid materials, mechanical metamaterial displacement is composed of structural and material deformation. This study leveraged a hexagon geometry to harness the toe region similar to ligaments using structure deformation and increase stiffness through material deformation, as shown in Figure 3.7.

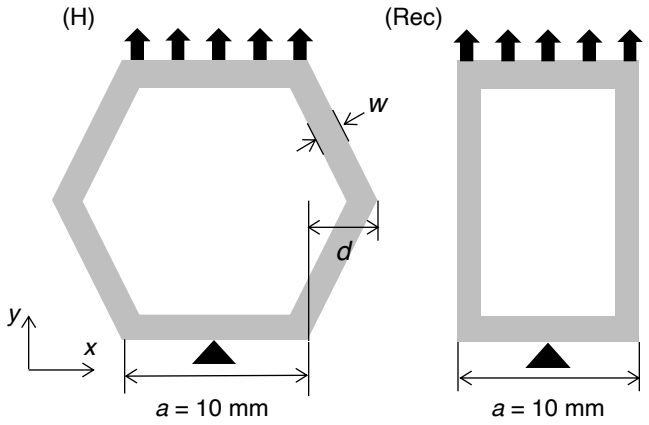

Figure 3.7: Schematics of regular hexagon and rectangle geometries are illustrated. The horizontally laid parallel sides of each geometry was 10 mm, and height was 17.3 mm.

When two parallel sides of a hexagon are laid horizontally, there are sides on either side, and these lateral sides will create the adaptive stiffness of the geometry. The lateral sides underwent structural deformation with a small force due to the free-hinge motion until the lateral sides were straightened when the hexagon geometry made of a flexible material was subjected to vertical tension. Then, material deformation dominated the deformation of the geometry, leading to the manifestation of the inherent stiffness of the flexible material and resulting in adaptive stiffness.

Figure 3.8 displays the load-displacement response of a regular hexagon with a length of horizontally laid sides (a) = 10 mm, width (w) = 1 mm, thickness (t) = 2 mm, and a rectangle with a = 10 mm, w = 1 mm, t = 2 mm and height = 17.3 mm. It shows the nonlinear behavior of hexagon geometry with a toe and stiffness increasing regions similar to ligaments.

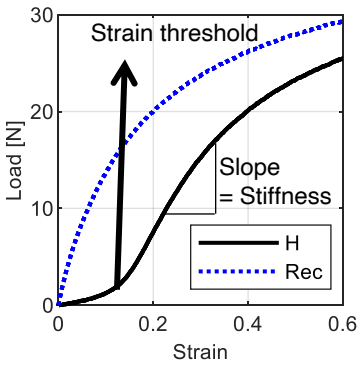

Figure 3.8: Load-strain response of hexagon and rectangle geometries are recorded.

3.4.2 Parametric optimization of adaptive stiffness metamaterial

The nonlinear behavior of hexagon geometries was fine-tuned using parametric optimization in FE modeling. The parameters that were controlled included the distance between the vertical side of the rectangle and the vertex where two adjacent sides of the hexagon meet (*d*), *w*, *t*, and the number of layers (*n*). Figure 3.9 overlaid on a reference Cartesian coordinate system, while relevant points associated with different portions of the hexagon geometry are labeled accordingly. *a* is affixed at 10 mm and vertexes A, and B can be expressed as:

$$A(A_x, A_y) = \left(\frac{a}{2}, \frac{\sqrt{3}a}{4}\right) \quad (3\text{-}1)$$

$$B(B_x, B_y) = \left(\frac{a}{2} + d, 0\right) \quad (3\text{-}2)$$

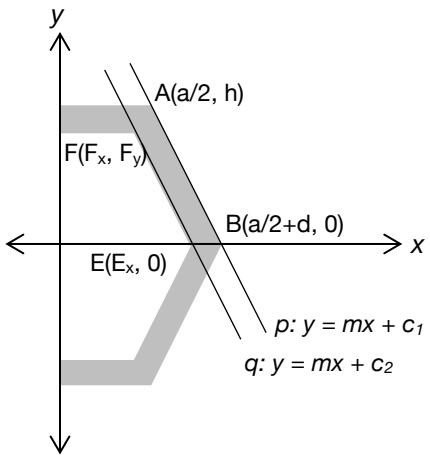

Figure 3.9: Right side of hexagon geometry is overlaid on Cartesian coordinate system. Vertexes are calculated using the linear equations.

The line (p) passing through vertices A and B can be represented by the slope denoted by m and the intercept denoted by c_1. The intercept of the offset line of p, denoted by q, is represented with c_2. The value of m, c_1 and c_2 can be expressed as:

$$m = \frac{B_y}{B_x - A_x} \quad (3\text{-}3)$$

$$c_1 = -mB_x \quad (3\text{-}4)$$

$$c_2 = c_1 - w\sqrt{m^2 + 1} \quad (3\text{-}5)$$

Then, vertex E and F can be expressed as following:

$$E(E_x, E_y) = \left(-\frac{c_2}{m}, 0\right) \quad (3\text{-}6)$$

$$F(F_x, F_y) = \left(\frac{F_y - c_2}{m}, B_y - w\right) \quad (3\text{-}7)$$

First, the strain threshold and maximum stiffness point were manipulated by varying *d* from 1 to 9 mm with a step size of 1 mm, while fixing *w* and *t* at 1 mm and 2 mm, respectively. Figure 3.10a illustrates the load-strain response of geometries with *d* = 1, 5, and 9 mm, indicating that the toe region lengthened as *d* increased. Strain threshold and maximum stiffness point of each geometry were obtained using linear regression and slope calculation and depicted in Figure 3.10b. While the geometry with *d* = 1 mm did not exhibit a toe region, the geometry with *d* = 2 mm and greater did. As *d* increased, the length of the lateral sides increased, resulting in a longer toe region and maximum stiffness occurring at higher strains. Figure 3.10c shows the corresponding stiffness at the maximum stiffness point, which decreased as *d* increased. The difference between the length of the outer hexagon and the inner offset line also increased as *d* increased. This caused material deformation to occur simultaneously with structural deformation, resulting in a decrease in stiffness at the maximum stiffness point. As mentioned earlier, the supporting material for CFL must provide its maximum support before 8% strained, so the hexagon geometry with *d* = 3 mm is suitable. Similarly, the material supporting the ATFL requires a geometry with *d* = 4 mm, and the heel pad and fifth metatarsal require a geometry with *d* = 5 mm.

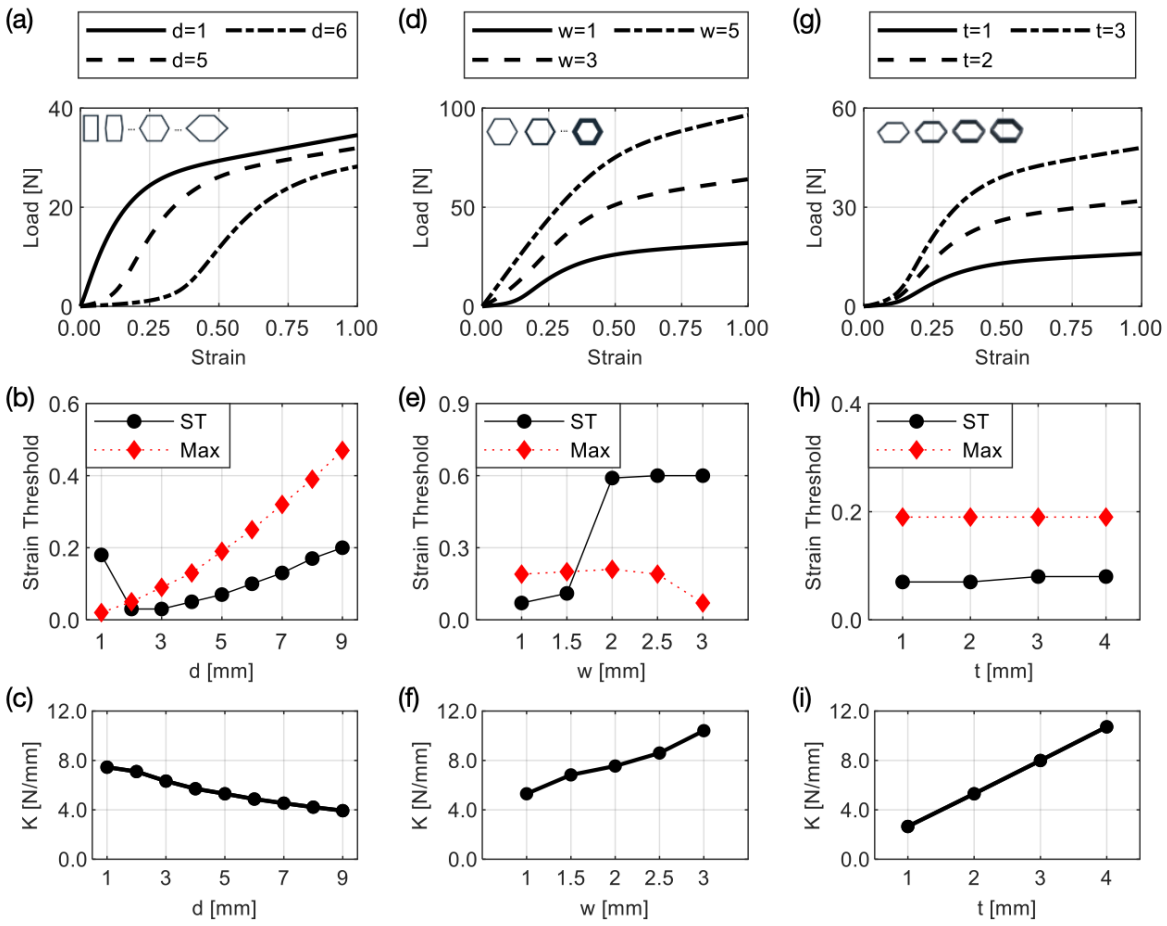

Figure 3.10: (a, d, g) The load-strain response of hexagon geometries when *d*, *w*, or *t* was varied is presented. (b, e, h) ε_{th} of each geometry and ε_{Max} was obtained through MATLAB and illustrated. (c, f, i) The maximum stiffness (K) of each geometry was calculated.

Next, *w* and *t* were adjusted to control the stiffness. The load-strain response, strain threshold (ε_{th}), and stiffness at the maximum stiffness point (ε_{Max}) of the geometry were analyzed by varying the *w* and *t* with a fixed hexagon size (d = 5 mm). Figure 3.10d-f show the results when *w* was varied from 1 to 3 mm with a step size of 0.5 mm while keeping *t* at 2 mm. Figure 3.10g-i show the results when *t* was varied from 1 to 4 mm with a step size of 1 mm while keeping *w* at 1 mm. As shown in Figure 3.10d and Figure 3.10g, stiffness increased as the cross-sectional area increased, so it is natural that stiffness increased as *w* or *t*

increases. However, excessive increase in *w* can make it difficult for the connection points to function as free-hinges, as the bending stiffness of adjacent lateral sides increased, resulting in absence of toe region as shown in Figure 3.10e. Therefore, geometries with *w* greater than 2 mm were not suitable for adaptive stiffness purposes. On the other hand, Figure 3.10h shows that the strain threshold and maximum stiffness point was maintained regardless of *t.* However, a thickness greater than 3 mm can compromise the user's compliance. In this study, the geometry with $w = 1$ mm would be used to maintain the toe region and $t = 2$ mm to ensure compliance.

As mentioned earlier, materials that would support ligaments require greater support than other directions. A hexagon composed of a double layer was designed to increase the stiffness of the geometry without affecting the toe region, as depicted in Figure 3.11a. Since the geometry maintains $w = 1$ mm, the geometry exhibits the nonlinear behavior, as shown in Figure 3.11b, and doubled the stiffness as the cross-sectional area increased, as shown in Figure 3.11c. Therefore, supports for ligaments that require greater restriction would leverage hexagons with a double layer.

3.4.3 Optimal shape of adaptive stiffness metamaterial

In addition to hexagon geometry, strain thresholds and stiffness were also evaluated by varying *d* for round, and diamond geometries to demonstrate the optimal structure for adaptive stiffness. Figure 3.12 show the strain threshold and

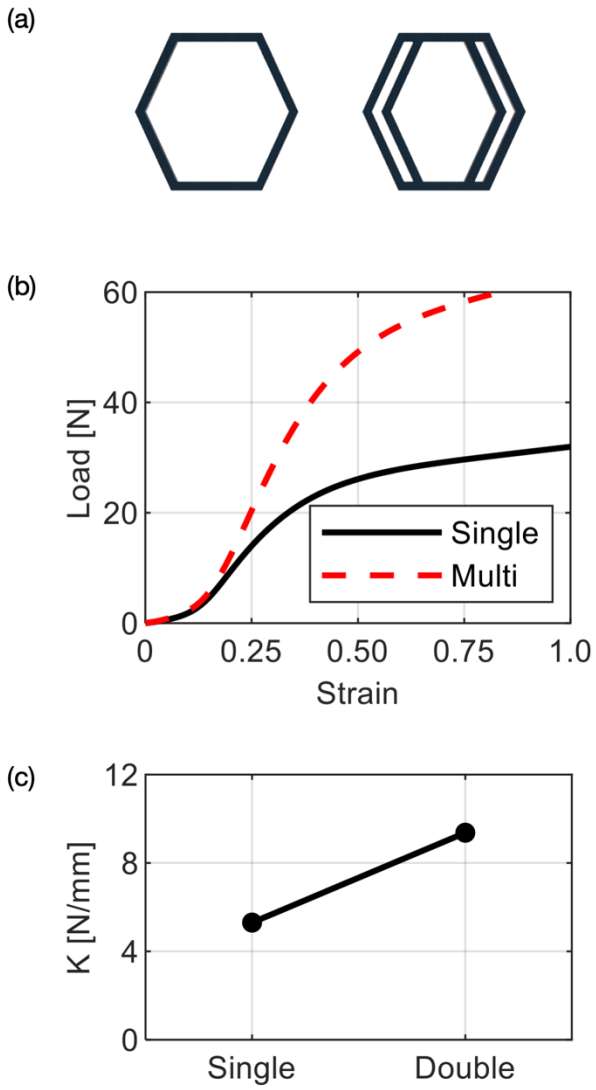

Figure 3.11: (a) Rendering of single and double layered hexagon geometries are depicted. (b) The load-strain responses of single and double layered hexagon geometries are presented. (c) The maximum stiffness of each geometry is plotted.

maximum stiffness for round and diamond geometries as *d* increased. The round shape had a larger increase on side length with increasing *d*, resulting in reaching the strain threshold and maximum stiffness point at a higher strain. The diamond geometry showed almost identical results as the hexagon geometry due to the

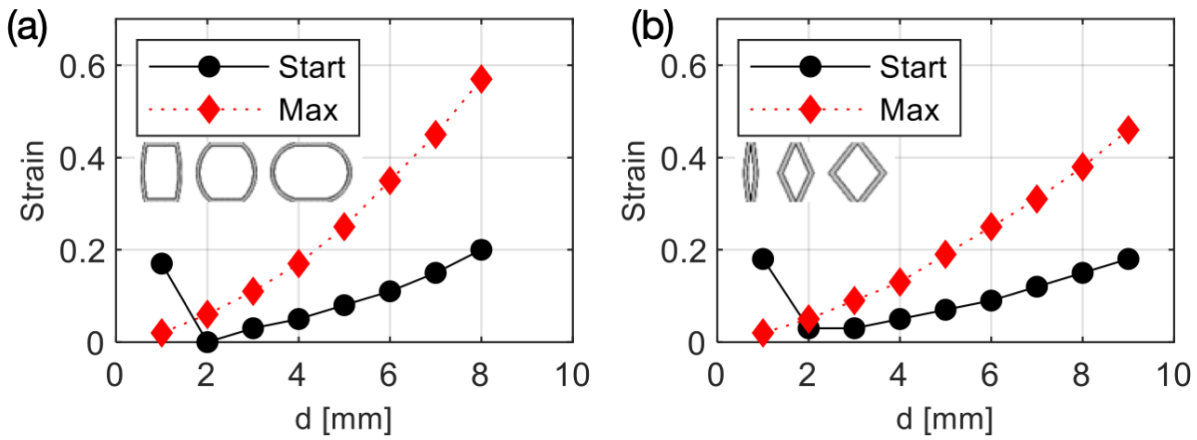

Figure 3.12: Strain threshold and maximum stiffness points of (a) round and (b) diamond shape with varying *d* is plotted.

same side length. Figure 3.13 shows the stiffness of hexagon, round, and diamond geometries with different *d*. The increase in the outer and inner side length of the round shape with *d* caused a significant decrease in stiffness at higher values of *d*. As a result, the stiffness that was similar to the hexagon geometry at $d = 1$ became lower than the stiffness of the diamond geometry at higher values of *d*. The diamond geometry always showed lower stiffness than the hexagon geometry because there are no horizontally parallel sides, resulting in stress concentration and earlier material deformation. Therefore, in this study, the hexagon structure was determined to be the most suitable geometry for adaptive stiffness, and a prototype would be created using this structure.

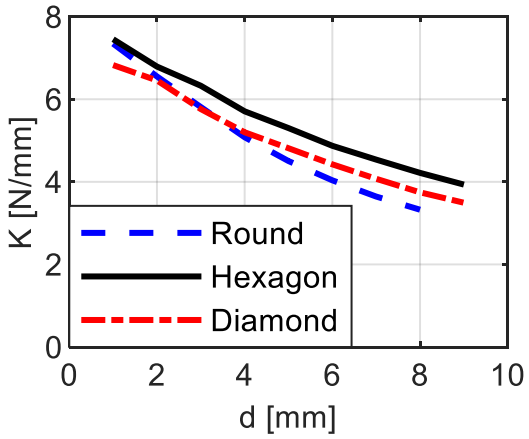

Figure 3.13: The maximum stiffness of round, hexagon and diamond shape is captured.

3.5 Design of prototype ankle brace

3.5.1 Design and fabrication of adaptive stiffness ankle brace

The prototype ankle brace coupon with designed hexagon geometries was attached to the neoprene sleeve brace and compared with commercial braces through BIODEX testing. Figure 3.14 presents a rendering of prototype coupon with a ring that fixed to the malleolus and designed hexagon geometries for CFL, heel pad, fifth metatarsal and ATFL in a counterclockwise direction from the left. The 3D-printed prototype coupon was attached to the neoprene sleeve ankle brace by stitching the malleolus ring and each of the parallel sides, as shown in Figure 3.15a. The neoprene ankle brace was not as stretchy as other sleeve braces that wrap around the foot to conform to its shape. Instead, it was designed to replicate the shape of the foot, making it easier to attach the coupon. Furthermore, since other sleeves may deform irregularly when worn, the neoprene ankle brace allowed for consistent strain on the prototype coupon. The torque generated

Figure 3.14: A rendering of prototype ankle brace coupon is captured.

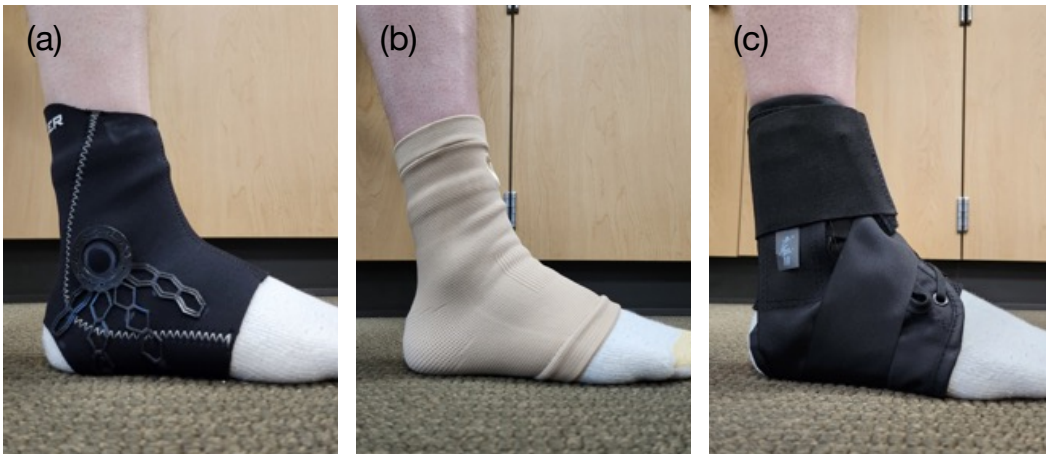

Figure 3.15: (a) The prototype coupon was 3D-printed, then stitched on commercial neoprene ankle brace. Model is wearing (b) a sleeve brace from Crucial and (b) an ASO lace-up brace

during the inversion was measured using the BIODEX multi-joint system for participants who were either not wearing a brace or were wearing the prototype, a commercial sleeve brace, or a commercial lace-up brace. The selected commercial braces were the most popular products on Amazon, with the sleeve brace known to exhibit nonlinear behavior (see Figure 3.15b), and the lace-up brace used as an ankle stabilizer (see Figure 3.15c).

3.5.2 Support capability of adaptive stiffness ankle brace

The BIODEX system was leveraged to evaluate the prototype brace's and commercial braces' support capability. Figure 3.16a illustrates the torque values recorded during inversion and eversion while subjects wore different braces. The lace-up brace, constructed with a stiffer material, exhibited higher torque values at all angles than the other braces. The sleeve brace showed minimal difference compared to not wearing a brace. Up to 25º of inversion, the prototype brace showed little difference in torque values compared to no brace or sleeve brace. However, a significant increase in measured torque values was observed beyond this point.

In addition, the effectiveness of the brace was assessed using injury prevention ability and time rate of tension development. The average power was calculated at each angle and presented in Figure 3.16b. The total work at each angle was divided by the time required to complete the work to obtain average power. This metric demonstrates how quickly the muscles or muscles in

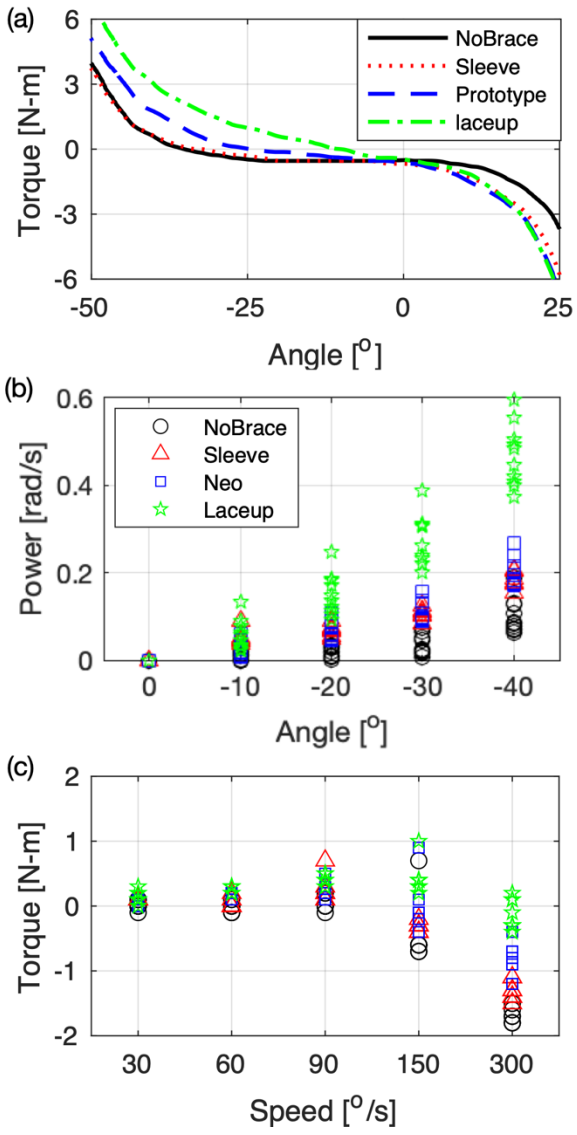

Figure 3.16 (a) A rendering of prototype ankle brace coupon is captured. (b) The prototype coupon was 3d-printed, then stitched on commercial neoprene ankle brace. Model is wearing (c) a sleeve brace from Crucial and (d) an ASO lace-up brace.

combination with the brace can generate force, indicating injury prevention ability. The lace-up brace exhibited significant power generation starting from 20º of inversion. On the other hand, the prototype brace initially produced similar power to the sleeve brace up to 20º; however, at larger angles, it generated greater

power than the sleeve brace. It indicates similar compliance during a lower range of motion and better ankle protection during a higher range of motion.

Furthermore, the time rate of tension development was assessed by measuring the torque generated at 0.2 sec for each inversion speed, as shown in Figure 3.16c. It takes approximately 0.2 sec for the leg extensions to develop enough force to support the body during normal ambulation upon heel strike. Therefore, the torque generated within 0.2 sec can be used to evaluate the tension developed in normal ambulation. The torque values measured at 0.2 sec consistently favored the lace-up brace, with the difference becoming more pronounced at higher inversion speeds, such as 150º/sec. At 300º/sec, the prototype brace generated less tension than the lace-up brace but performed better than the sleeve brace in tension development. Negative torque at higher speeds can be attributed to the passive stabilizing structures, such as ligaments or joint capsules, reaching their maximum stretch and providing less resistance to the inversion motion. In comparison to the state without wearing the brace, it can be observed that the prototype brace significantly contributes to the generation of tension.

3.6 Conclusion

In conclusion, the development and evaluation of the adaptive ankle brace yielded promising results, highlighting its potential for injury prevention and improved ankle performance. The incorporation of the innovative hexagon structure within the brace

design proved to be a key factor in achieving adaptive stiffness. By utilizing the hexagon structure, the brace was able to modulate its stiffness in response to applied strains, effectively enhancing ankle stability and reducing the risk of injuries. The BIODEX testing and motion capture analysis helped identify optimal material design parameters and metamaterial structure placement, ensuring effective resistance against inversion forces.

Parametric optimization using FE modeling resulted in a hexagon geometry with nonlinear behavior during ankle inversion. The controlled parameters, such as the distance between the rectangle and hexagon vertex (d), width (w), thickness (t), and number of layers (n), influenced the strain threshold and maximum stiffness point of the brace. Varying these parameters allowed for customization of the brace's support for ligaments, such as CFL and ATFL. The findings provided valuable insights for the design and optimization of adaptive stiffness metamaterials in ankle braces and potentially in other joint systems.

The prototype brace exhibited higher torque values and improved power generation, indicating its potential to effectively support the ankle joint during dynamic movements. Furthermore, the incorporation of adaptive stiffness metamaterials in the ankle brace opened up possibilities for their application in other joint systems, such as the knee or wrist, providing targeted support during high-intensity activities while allowing for comfortable movement during low-intensity activities.

Overall, the adaptive ankle brace demonstrated great promise in terms of injury prevention and improved ankle performance. The integration of Biodex testing, motion

capture analysis, and the innovative hexagon structure was instrumental in developing a prototype brace with superior mechanical properties and adaptability. Future research and development efforts should focus on further refining the brace design, conducting extensive clinical trials, and evaluating its long-term effectiveness in real-life scenarios. With continued advancements, the adaptive ankle brace has the potential to significantly enhance ankle support and contribute to the well-being and performance of individuals engaged in sports and physical activities.

Chapter 3, in full, is currently being prepared for submission for publication of the material. Park, Yujin; Zhao, Xinlun; Slider, Amy; Sessoms, Pinata; Fraser, John J., and Loh, Kenneth J. The dissertation author was the primary researcher and author of this material.

CHAPTER 4: Bio-Inspired Active Skin (BIAS)

4.1 Introduction

A striking feature of biological organisms is that they are born with exceptional capabilities and functionalities, such as the ability to change their properties depending on their needs and the surrounding environment. This unique behavior has inspired many researchers to mimic and develop bio-inspired artificial materials that exhibit exotic properties and variable surfaces. The current body of research on artificial materials focuses on replicating the capabilities of nature's creations, such as large levels of stretchability [88], enhanced fracture toughness [106], adhesion [25; 40; 49], super-hydrophobicity [11; 27; 66], and drag reduction [26; 29; 84]. For example, dry adhesives could be obtained by creating nano- and micro-structured fibrillar surfaces like the gecko's foot [25; 40; 42], and 3D printing flexible denticles can be used to reduce the drag-coefficient like the sharkskin [29; 30]. Shape morphing is one of the enticing characteristics of biological organisms. They can reversely, on-demand and effectively morph their shape for various purposes like locomotion camouflage, signaling, and hunting [89].

On-demand and reversible morphing of 2D surfaces into programmed 3D structures can enable the innovative design of active, functional structures for various engineering applications [71]. For example, they have been employed in biomimetic robots with motorless/gearless locomotion systems [20; 95; 120], as well as biomedical devices such as scaffolds [131; 132], stents [126], and drug delivery systems [121]. Currently, the most promising surface and shape morphing structures are based on smart

materials with anisotropic properties, such as shape memory alloys (SMAs), shape memory polymers (SMPs), and stimuli-responsive polymers (SRPs). On the other hand, composite materials formed using multiple isotropic materials have also been designed, where the relative positions and volume fractions of different materials generate eigen-strains in the composite structures to drive shape change [60]. They have been designed to achieve simple morphologies like rolling and bending, as well as more complex morphologies, including flower-blooming [1; 114] and box folding [73].

Despite the many innovations in this space, the search for smart materials that offer both a large degree of actuation and reversible mechanical behavior continues. The amount of actuation generated by SMAs is typically insufficient for shape morphing. Meanwhile, SMPs can achieve greater shape change than SMAs, but their response is often irreversible, and the material requires a mechanical programming process [71]. SRPs offer both reversible and large actuation; however, combining multiple materials to enable morphing in a controlled manner remains challenging [10].

Another approach to achieve surface and shape morphing is by using mechanical metamaterials. Mechanical metamaterials respond to mechanical inputs and exhibit unique behaviors such as auxetic [59], negative swelling ratio [128], and shape morphing [18; 52; 81]) by harnessing the motion and instabilities (*i.e.,* buckling, snapping, or rotation) of their 2D, lattice-like, patterned unit cell geometries. For example, origami and Kirigami, which are Japanese paper art forms, have inspired the creation of shape morphing designs used for deployable structures [43; 80; 97; 133], medical devices [63; 94], and soft robotics actuation systems [65; 92].

Another example is buckling-induced mechanical metamaterials, where they can achieve repeatable and reversible shape morphing while deforming within their elastic limit. When the material is compressed, the series of slender beams buckle, and it returns to its initial or pristine state when stress is removed [23; 36; 123]. Advancements in additive manufacturing have enabled the realization of complex, patterned, mechanical materials that exhibit shape morphing by incorporating smart materials with the geometry; however, they suffer from some drawbacks too. First, the unit cells can deform heterogeneously because of printing errors (*e.g.,* caused by oozing, blobs, zits, and tiny pores). Second, they always need mechanical loading to achieve morphing, which can limit their potential use cases. Last, when used in a large array, the mechanical loads needed to achieve shape morphing are considerably larger than for a single unit cell geometry. This emphasizes the importance of reducing the mechanical force for single unit cell actuation, even though it may seem relatively small, when considering its application within a larger system or structure.

This chapter presents a Bio-Inspired Active Skin (BIAS), which is a 2D to 3D morphable structure under uniaxial strain using a single material. It exhibits local and/or global programmable, rapid and reversible, out-of-plane surface texture morphing when actuated by in-plane tension. The objective was to establish the design principle for 2D to 3D morphable structure under uniaxial strain using a single material. The BIAS geometry leveraged the re-entrant star geometry as its foundation. By incorporating the pre-conceived auxetic geometry with the principle of buckling-induced instability, the designed geometry exhibits local and/or global programmable, rapid, and reversible, out-of-plane surface texture morphing when actuated by in-plane tension.

Although the focus of this work was on the star re-entrant geometry as shown in Figure 4.1, the design principle can be extended to other re-entrant auxetic designs that can morph into different 3D configurations. First, the deformation mechanism of the star re-entrant geometry was analyzed to harness the generated stress as a driving force for out-of-plane deformation. Second, a parametric optimization study was performed to identify the geometrical parameters that resulted in higher out-of-plane buckling instability so that shape morphing could be triggered by the least amount of stress and strain. Third, imperfections or notches of different sizes were introduced at different locations in the pattern to understand their role in controlling its shape morphing response. Last, optimized BIAS geometries were 3D-printed and tested to verify their expected shape morphing behavior.

4.2 Materials and Methods

4.2.1 Sample fabrication

Two types of samples were fabricated in this study. First, BIAS unit cell geometries with varying width (w_{BIAS}) and rib angle (θ), where θ is the acute angle between two slender beams, were designed using Autodesk Fusion 360; thickness (t_{BIAS}) of the unit cell geometry was fixed at 1 mm. The BIAS geometries were then exported as an STL mesh before being uploaded to Ultimaker Cura 5.4 for 3D printing. They were 3D-printed with TPU 95A filament using an Ultimaker 3+ FDM 3D printer. The printing temperature was 220 °C, and the printing speed was 10 mm/sec. Infill density was 100%, infill geometry was the line pattern, and layer thickness was 0.1 mm.

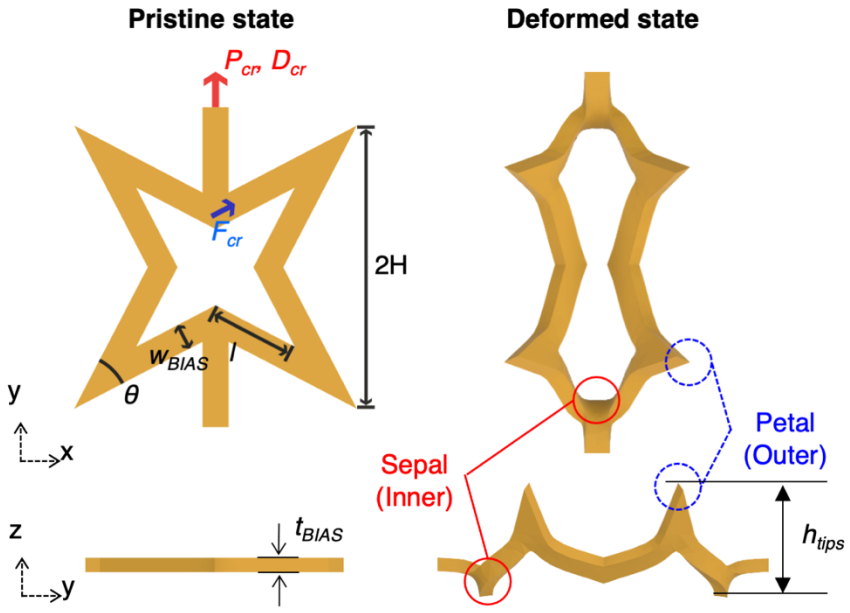

Figure 4.1: A rendering of the re-entrant star geometry is depicted.

4.2.2 Tensile tests

Both 3D-printed tensile test specimens and BIAS geometries were subjected to uniaxial tensile tests conducted using a Test Resources 150R electromechanical load frame. The BIAS geometries were strained to 100%, respectively. In this study, the strain rate was fixed at 0.2 min^{-1} to minimize the strain hardening effect of TPU. In this study, the strain rate was fixed at 0.2 min^{-1} to minimize the strain hardening effect commonly observed in the viscoelastic behavior of TPU. By using a slower strain rate, the study aimed to focus on TPU's elastic properties and reduce the rate-dependent effects during deformation.

4.2.3 Numerical simulations and parametric study

The stress distributions of BIAS geometries strained in tension were analyzed using the extracted experimental Mooney-Rivlin material model parameters. Figure 4.2 shows one-quarter of the BIAS geometry overlaid on a reference Cartesian coordinate system, while relevant points associated with different portions of the BIAS geometry are labeled accordingly. The coordinates of the outer tip (H, H) were fixed at (15, 15) mm, while the rest of the points (*i.e.,* I, J, K, and N) can be expressed as:

$$I(I_x, I_y) = \left(H\left(1 - \tan\left(\frac{90-\vartheta}{2}\right)\right), 0\right) \tag{4-1}$$

$$J(J_x, J_y) = \left(I_x - w/\cos\frac{90-\theta}{2}, 0\right) \tag{4-2}$$

$$K\left(K_x, K_y\right) = \left(-J_x/\left(\tan\frac{90-\theta}{2} - 1\right), -J_x/\left(\tan\frac{90-\theta}{2} - 1\right)\right) \tag{4-3}$$

$$\mathrm{N}\left(\mathrm{N_x}, \mathrm{N_y}\right) = \left(\frac{w}{2} + w/\sin\frac{90-\theta}{2}, \frac{N_x}{K_x}(K_x - J_x) + J_x\right) \tag{4-4}$$

Then, FE numerical simulations were performed using COMSOL Multiphysics, as mentioned earlier. The FE model of each BIAS unit cell was meshed using quadratic tetrahedral elements, each with a minimum element size of 0.1 mm and a maximum element size of 0.5 mm. The average element quality of the mesh, which represents the regularity of the mesh's shape, was always over 0.5 to avoid inverted mesh elements. To account for the thinness of the model relative to its width and length, the mesh density in the thickness direction was

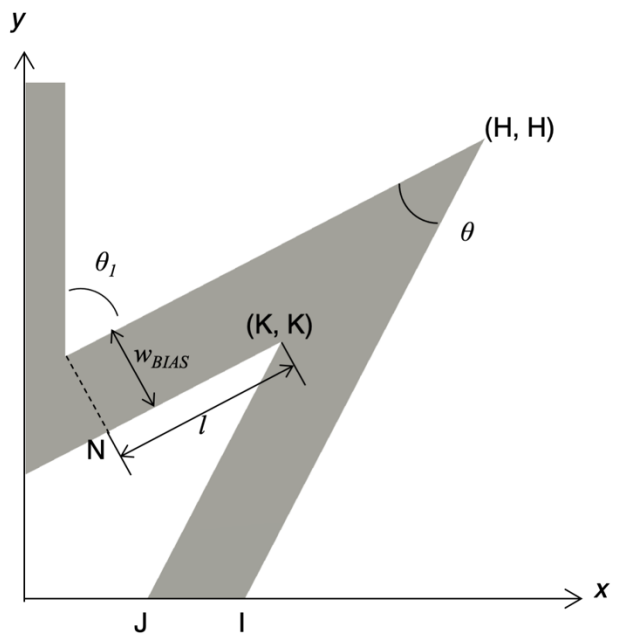

Figure 4.2: One tip of the BIAS geometry is recreated in a coordinate system. The dimension of each point is expressed in equation (4-1 to 4). The abbreviations used in the table denote w_{BIAS}, θ, and l.

doubled. Upon creating the model, it was strained by fixing one end of the BIAS geometry and then applying stress on its opposite end. Due to the nonlinear behavior of the BIAS geometry, an auxiliary sweep was employed.

4.3 Results and Discussion

4.3.1 Deformation mechanism of the BIAS unit cell

The deformation mechanism of a unit cell Active Skin geometry under uniaxial tensile strain is illustrated in Figure 4.3 and Figure 4.4. The stress-strain result shows that its mechanical response is nonlinear. In addition, images taken during the tensile testing and the stress distribution results from FE modeling

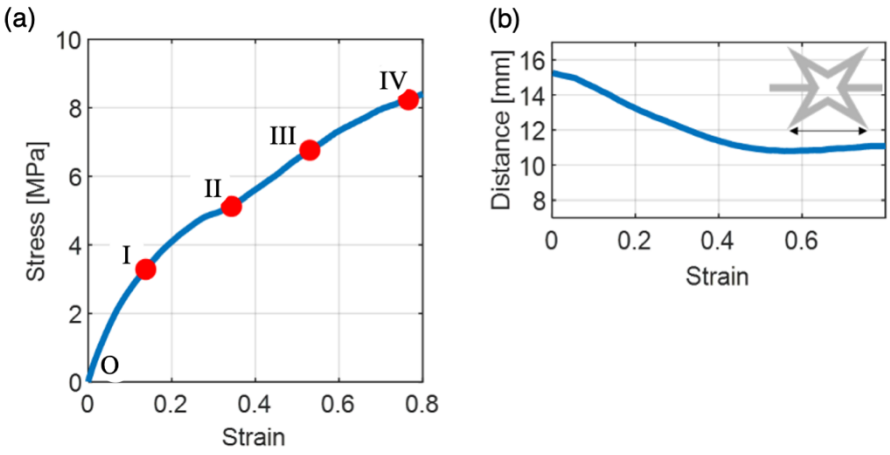

Figure 4.3: (a) The mechanical response of unit cell star geometries subjected to applied uniaxial tension is plotted. (b) The distance between petal (or outer) tips during uniaxial tension is plotted.

analyses, corresponding to the various points marked in the stress-strain plot, are depicted together to characterize the deformation process. The Active Skin specimen used for tensile testing was 1.5 mm thick, which is the same as its width to harvest buckling-induced instability of the thin substrate.

Analysis of the stress-strain plot shown in Figure 4.3 shows that, during the initial stage of loading, linear response was observed. The Active Skin exhibits in-plane auxetic behavior, which means the distance between sepal tips (DBS, or inner tips) increased, while the distance between outer tips (DBP, or outer tips) remained constant. The stress distribution result in Figure 4.4 for point I confirms that the movement of the sepal tips generated localized compression in the lateral elements right next to the sepal tips as θ_1 was increased. Once θ_1 reached 90º, the stress-strain curve exhibited nonlinearity, and the compressive stresses induced out-of-plane deformations of the sepal and petal tips (*i.e.,* at the

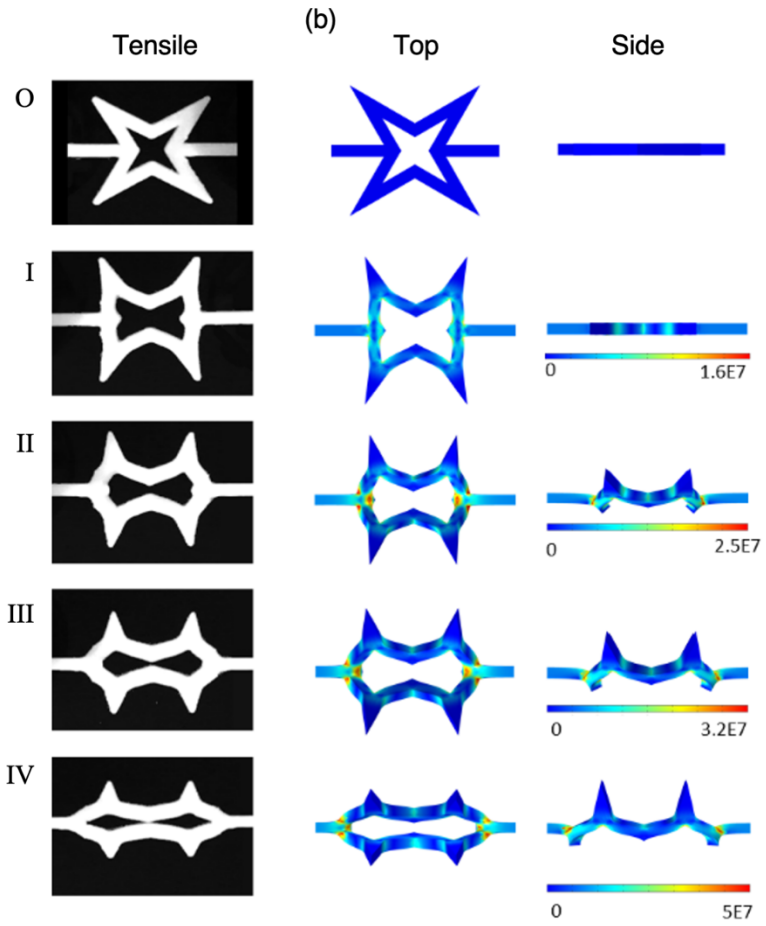

Figure 4.4: Images taken during (a) the tensile test and (b) stress distribution results from COMSOL FE modeling results that correspond to the labeled points in Figure 4.3 (a) are shown.

end of point I). This point coincides with the critical buckling point of the star geometry, where out-of-plane deformations began.

Nonlinear behavior transitions to linear when the ends of the sepal tips and petal tips are aligned (point II). During applied in-plane tensile strains to the unit cell, stress was concentrated not only near the two sepal tips, as was previously mentioned, but also near the four petal tips where the slender elements began to buckle outwards. Out-of-plane movement was enlarged through the seesaw-like

behavior of the petal and sepal tips, since they always buckled in opposite directions and pushed each other. Thus, the Active Skin reached its full-out-of-plane deformation at point III when DBP was at its minimum. After point III, DBP increased again, and the stress-strain curve became inelastic with plastic deformation observed. Overall, when applied strains were released, the Active Skins could return to its pristine flat orientation.

The instability of the star geometry could be magnified when substrate thickness was reduced, which means that the Active Skin produces out-of-plane deformations in response lower magnitudes of applied strains and stresses. However, since these slender elements are susceptible to extrinsic factors, thin Active Skins could deploy in random buckling directions, which is undesirable for surface morphing applications where precise control is needed. Figure 4.5 shows the critical locations where stresses are concentrated during out-of-plane deformations. These same locations were selected for introducing geometrical imperfections or notches to the Active Skins. The notches colored in red in Figure 4.5 would shift the neutral axis downwards, which effectively concentrated mechanical instabilities towards the desired direction. On the other hand, the notches in blue were introduced to facilitate bending.

The mechanical response of a notched Active Skin is depicted in Figure 4.6, and the points that segregate the deformation stages are also marked. The height-to-thickness ratio (h/t) was varied and selected as the parameter to evaluate the role of notch depth in affecting the Active Skin's critical buckling point. Figure 4.6 shows that Active Skins with deeper notches (h/t=2/3) were

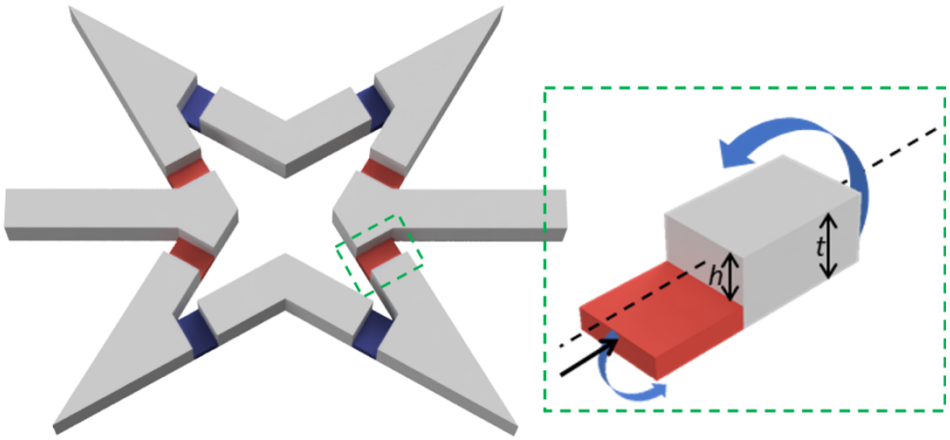

Figure 4.5: A rendering of the Active Skin with purposefully implemented notches is illustrated.

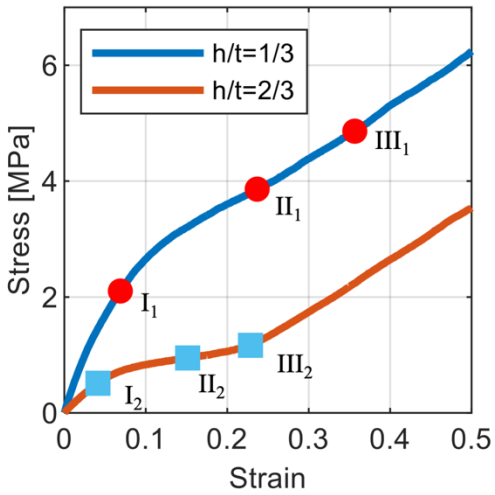

Figure 4.6: The mechanical responses of notched Active Skins were characterized.

energetically favorable in that they required a significantly lower critical buckling stress and strain to achieve pattern deployment.

Moreover, Figure 4.7 show that stress is effectively concentrated only at the notches, which facilitates easier bending of the petal tips. It can also be verified from the images taken during loading that deeper notch allowed for

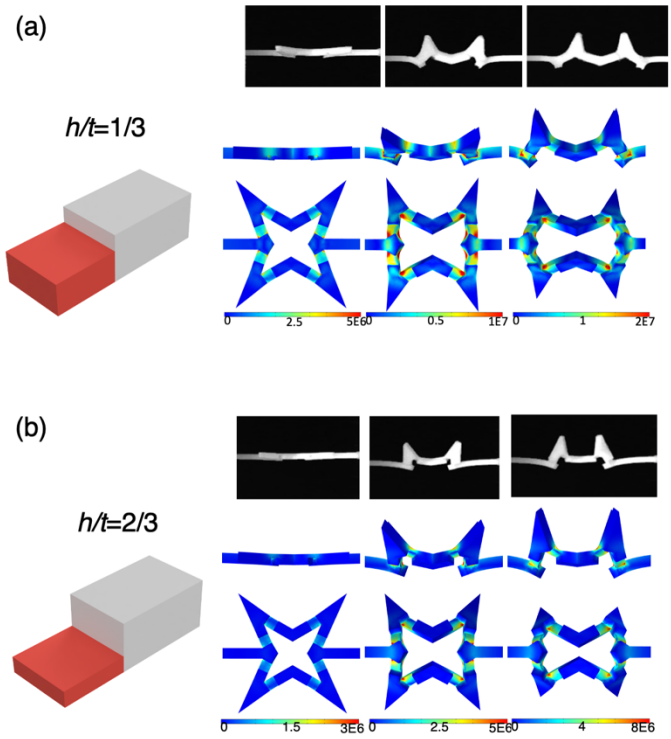

Figure 4.7: Images of Active Skins with h/t of (a) 1/3 and (b) 2/3 strained in uniaxial tension are presented.

reaching the minimum DBP at lower magnitudes of applied strains and stresses (*i.e.*, points C_2 versus C_1). Overall, this work demonstrated that designed imperfections enabled better control of the directionality of out-of-plane deformations of the star pattern. Furthermore, patterns with deeper notches needed lower critical buckling stresses and strains for triggering deployment of petal and sepal tips.

4.3.2 Parametric optimization of the BIAS unit cell

Parametric optimization was performed to increase the buckling instability of the slender elements in the BIAS geometry. The BIAS geometry was assumed to be a series of slender rectangular beams connected to free hinges, which meant that the critical buckling force of the beam could be used as the metric for assessing the instability of the beam. Parametric optimization was conducted by varying w_{BIAS} from 1.5 to 3.5 mm and θ from 20° to 35° (Figure 4.2). Figure 4.8 depicts the collection of the BIAS unit cells with different w_{BIAS} and θ considered. The beam length (l), which is the distance between points N and K (Figure 4.2) was determined using these geometric parameters. The unit cell geometry has the shortest length (l) when w_{BIAS} = 3.5 mm and θ = 20°; in contrast, the beam is the longest when w_{BIAS} = 1.5 mm and θ = 35°. Thus, each BIAS geometry could be uniquely defined according to its width and acute angle, which is represented as (w_{BIAS}, θ).

First, the load-displacement relationships obtained from the numerical model and tensile test were compared to validate the reliability of the model. Figure 4.9 overlays the experimental results and the numerically calculated load-displacement response of the (1.5 mm, 35°) BIAS geometry when strained in uniaxial tension. Initially, the geometry exhibited in-plane linear deformation before transitioning to a nonlinear behavior; out-of-plane deformation began when nonlinear mechanical behavior was observed and when the load-displacement response reached a critical point, which is defined as point C_{BIAS} in

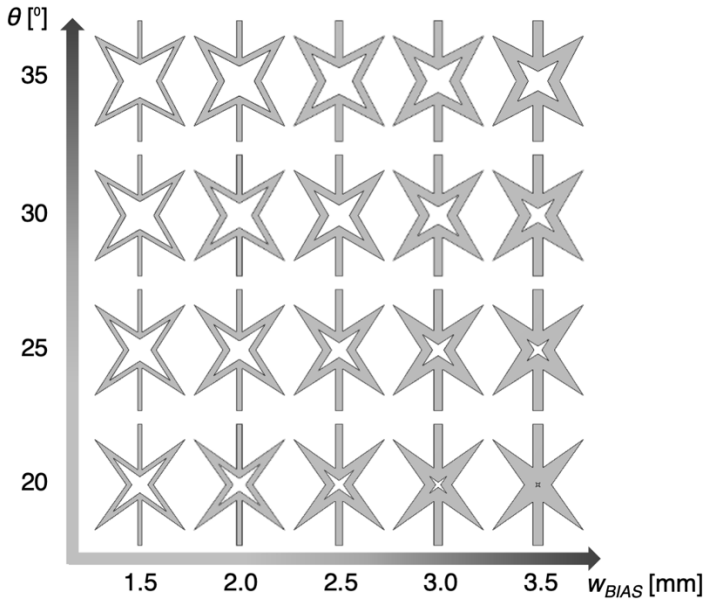

Figure 4.8: BIAS geometries with different w_{BIAS} and θ are illustrated.

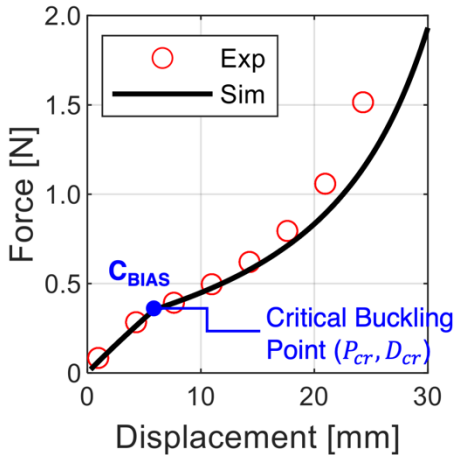

Figure 4.9: Load-displacement responses of the (1.5 mm, 35°) BIAS geometry during the uniaxial tensile tests are compared between experimental and calculated results.

Figure 4.9 [87]. Point C_{BIAS} was determined by fitting a linear regression model with a 99% confidence interval, which was also confirmed using image analysis of video frames of the specimens being strained [87]. Overall, as can be

seen from Figure 4.9, the simulation results coincided well with the experimental data until when shape morphing was completed (*i.e.,* full 2D-to-3D deformation of the outer tips) and when additional tensile strains only physically separated the deployed outer tips further apart. This portion of the force-displacement response, observed during deformation of the base-material (TPU), also corresponded to when strain-hardening effects were observed. However, strain-hardening did not have to be considered because, after this point, the BIAS geometry already completed shape morphing.

The instability of the rectangular beam of the BIAS geometry with various w_{BIAS} and θ was calculated and compared with results from the numerical model to identify that the shape of the beam determines the control of the BIAS geometry. As mentioned earlier, the free-hinging motion of BIAS slender rectangular beams generated localized compression that drove out-of-plane deformations. The localized compression generated on a slender beam at the critical buckling point is referred to as F_{cr} (see Figure 4.1). The corresponding load and displacement are denoted as P_{cr} and D_{cr}, respectively. F_{cr} of each geometry was calculated using the following equation:

$$F_{cr} = \frac{\pi^2 E w_{BIAS} t_{BIAS}^3}{12(2l)^2} \tag{4-5}$$

where E is the elastic modulus, w_{BIAS}, t_{BIAS}, and l are the beam's width, thickness, and length, respectively. The results of F_{cr} for BIAS geometries based

on different θ are plotted in Figure 4.10a, indicating that the instability of the beam with narrower w_{BIAS} and larger θ was larger when t was consistent. On the other hand, P_{cr} and D_{cr} for inducing out-of-plane deformations (labeled in Figure 4.2) were simulated and plotted in Figure 4.10b and c, respectively, both as a function of w_{BIAS}. The (3.0 mm, 20°) and (3.5 mm, 20°) results were omitted since they did not exhibit out-of-plane deformations. Figure 4.10b clearly shows that the BIAS geometry composed of beams with lower F_{cr} caused out-of-plane deformation under less P_{cr}. Thus, the instability of the geometry increased as it had a narrower w_{BIAS} and larger θ.

Meanwhile, the critical buckling displacement (D_{cr}) presented opposite trends against P_{cr} (see Figure 4.10c), which could be explained by Hooke's law and trigonometric functions. The compressing strain rate of the shorter beam was larger than that of the longer beam under the same displacement of the entire BIAS geometry. According to Hooke's law, the local compression generated in the compressed beam is proportional to the strain, and a lower instability (or a shorter beam length) can obtain a greater driving force for a smaller amount of total displacement. Consequently, a smaller D_{cr} was required as the w_{BIAS} decreased or θ increased. While shorter beams could generate relatively larger compression under the same D_{cr}, F_{cr} to be generated by D_{cr} increased as instability decreased. For instance, in the case of the geometry with w_{BIAS} = 1.5 mm, F_{cr} remains nearly the same regardless of the angle. Therefore, a larger D_{cr} was necessary as the length of the beam becomes longer (or θ becomes larger) when the length of the beam varies.

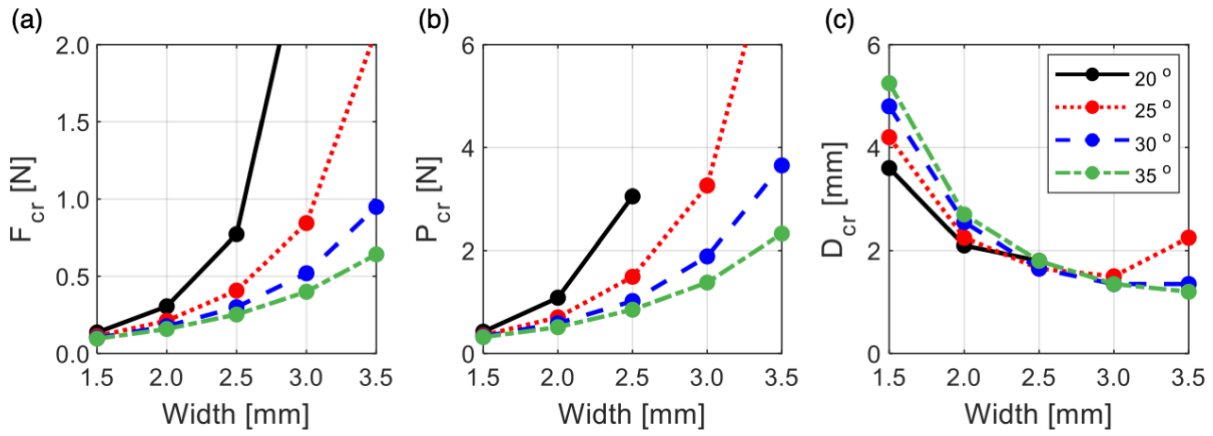

Figure 4.10: (a) The critical buckling force (F_{cr}) of each beam was calculated using equation (4-5) and is displayed. (b) The critical load (P_{cr}) and (c) displacement (D_{cr}) of each unit BIAS geometry were calculated through FE modeling in terms of w_{BIAS}.

On the other hand, in the case of w_{BIAS} = 2.5 mm, less F_{cr} is required as the length of the beam becomes longer. Therefore, the out-of-plane motion shows similar displacement regardless of the angle in the case of w_{BIAS} = 2.5 mm geometry due to the fact that the compression to be generated in the beam is less than that of the short beam geometry. The (3.5 mm, 25°) geometry showed exceptional behavior. Although a shorter beam generated larger localized compression, it was not enough to buckle the beam that required significantly larger F_{cr} as compared to other geometries. Similarly, the localized compression produced free hinge motion in the (3.0 mm, 20°) and (3.5 mm, 20°) geometries, which was not enough to produce out-of-plane deformation.

The critical point analysis revealed that the geometry with w_{BIAS} = 2.5 mm was the most optimized in terms of requiring relatively small F_{cr} and D_{cr} for out-of-plane deformation. Moreover, θ of 35° was considered optimal as it enhanced the instability of the geometry and D_{cr} remained small, regardless of θ. The

calculated P_{cr} and D_{cr} for star geometry when w_{BIAS} was fixed at 2.5 mm while θ was varied from 40° to 55° are presented in Figure 4.11 to investigate the effect of larger θ. D_{cr} of each geometry with w_{BIAS} = 2.5 mm was almost the same regardless of θ, while it actuated under the lowest P_{cr} with θ = 35°. Therefore, (2.5 mm, 35°) was used for the remainder of the study.

4.3.3 Notch geometry

Another particularly effective way to increase the instability of the geometry was by including artificial imperfections at key locations where the localized stresses were concentrated during deformation. Figure 4.12 shows the stress distribution of a slender rectangular beam without artificial imperfection. Since the stress distribution was horizontally symmetric, the orientation of out-of-plane deformation was random and was determined by other external stimuli (*i.e.,* load perturbation, burned residue, or pores). Our previous study showed that artificial imperfections, such as notches at key locations, manipulated the stress distribution, thereby enabling out-of-plane deformation in a controlled manner and reducing P_{cr} and D_{cr}. In particular, the notch was expected to be consistently below the beam's neutral axis, which enabled the beam to buckle in the direction of the unnotched structure, and a larger notch was assumed to decrease P_{cr} and D_{cr} more significantly.

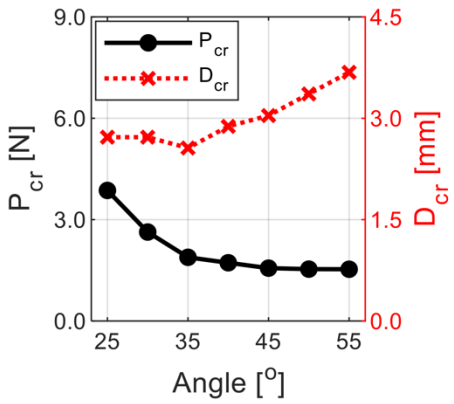

Figure 4.11: P_{cr} and D_{cr} of each unit BIAS geometry with larger θ based on w_{BIAS} = 2.5 mm was calculated.

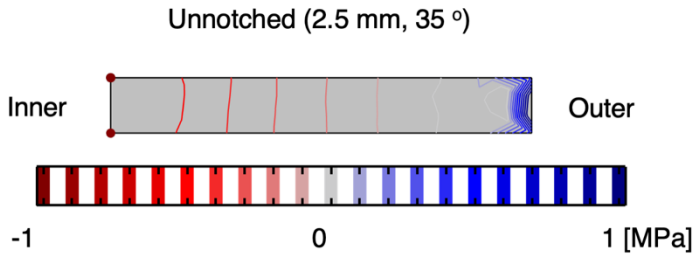

Figure 4.12: The stress distribution on the frontal surface of the unnotched beam is plotted. The image was captured at the end of in-plane deformation.

FE modeling models of the optimized BIAS geometry with different configurations and locations of notches were created to investigate the role of notches in their stress distribution. The BIAS geometry is symmetric, and Figure 4.13 shows the top-right portion of the geometry with notches placed at two key locations: the perpendicular plane at the intersection of the gripping bar and beam 1 (marked with a dashed rectangle) where the driving force was generated (marked by a red solid line), and the intersection plane between the outer tip and beam 2 (marked with a dash-dotted rectangle) where tension was concentrated during deformations (marked by a blue dashed line). The notch was of a cuboid

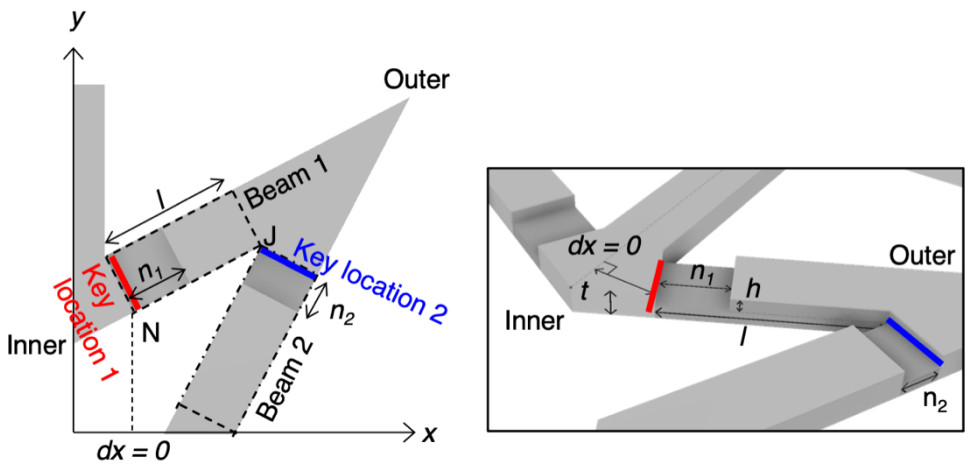

Figure 4.13: A rendering displays the top-right part of the outer tip of the BIAS geometry.

shape and had the same w_{BIAS} of the BIAS, while the length of the notch (n_1) was varied from 0.1 to 0.9 of the total beam length (l); depth (h_1) was varied from 0.25 to 0.75 of substrate thickness (t_{BIAS}). The location of the notch (dx) on beam 1 represents the horizontal distance between point N and the bottom-left point of the notch. The geometric detail of each notch is represented as (n_1, h_1, dx). The notch location on beam 2 was fixed at key location 2 and expressed as (n_2, h_2).

First, notches were induced on beam 1; n_1 and h_1 were varied while the location dx was fixed at 0 to demonstrate the effect of notch configuration on buckling behavior. Figure 4.14a and b show the corresponding P_{cr} and D_{cr} of each geometry. The triangle points indicate the buckling direction of each geometry when the notches were introduced on the upper surface. The geometries buckled in the direction of the notched surface (upwards buckling) when $n_1 = 0.2l$, regardless of h, as shown in Figure 4.15a. On the other hand, geometries buckled

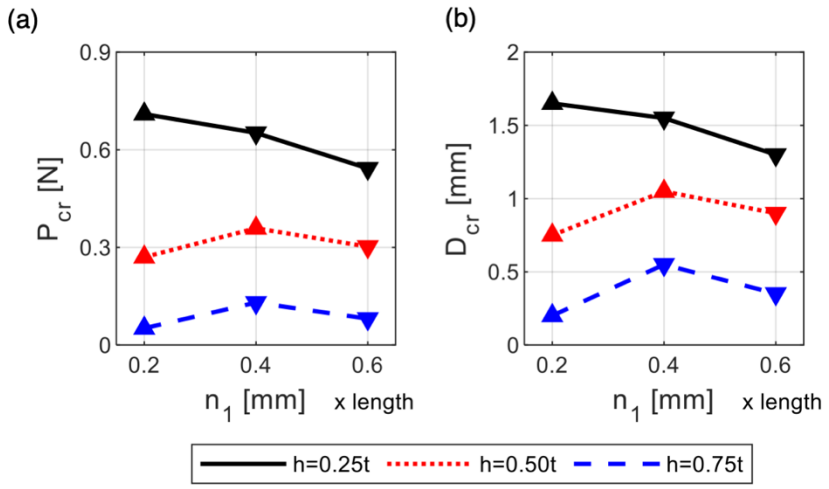

Figure 4.14: (a) P_{cr} and (b) D_{cr} of each unit geometry with different sized notches were calculated through FE modeling and are plotted. The triangle points reveal the buckling direction of each geometry when notch was induced on the top surface.

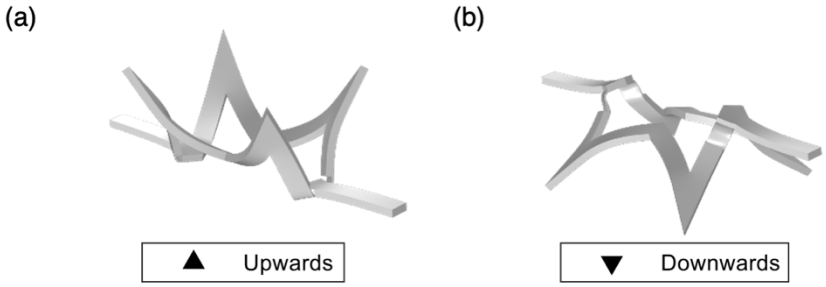

Figure 4.15: (a) The deformed (0.2l, 0.50t_{BIAS}, 0) and (b) (0.4l, 0.50t_{BIAS}, 0) BIAS geometries are illustrated.

in the opposite direction (downwards buckling) when $n_1 = 0.6l$, as shown in Figure 4.15b. These results revealed that the presence of notches alone is not sufficient for controlling the buckling direction. In addition, when the geometry buckled upwards, P_{cr} and D_{cr} increased as notches became wider, while they decreased when the geometry buckled downwards.

Buckling direction was determined by whether the notch could distribute the stresses evenly under the notch or concentrated on the indented surface. Figure 4.16 presents the stress distribution at the end of the in-plane deformation on a coronal plane of beam 1. Narrow notches ($n_1 = 0.2l$) augmented the stress concentration at key location 1 and hindered horizontally symmetrized stress distribution since the sharp edge notches led to abrupt stress changes near the indented surface. More significant stress was concentrated around the indented surface as compared to the bottom of the substrate and made the notched part buckle upwards. In other words, buckling direction was determined by the notched portion rather than the entire beam when stress was unevenly distributed under the notches. Therefore, although deeper notches such as ($0.2l$, $0.50t_{BIAS}$, 0) and ($0.2l$, $0.75t_{BIAS}$, 0) were able to reduce P_{cr} and D_{cr}, they could not move the neutral axis of the entire beam.

The geometry with $n_1 = 0.4l$ notches clearly shows the effect of notch depth on stress distribution. As the length of the notched part increased, the stress concentration on the surface reduced. This results in even stress distribution under notches lowering down the neutral axis of the entire beam. Thus, the geometry with $h = 0.25t_{BIAS}$ buckled downwards. When the geometry had deeper notches ($0.4l$, $0.75t_{BIAS}$, 0), stress concentration near the indented surface was significantly higher compared to stress on the bottom substrate, and the level of stress concentration increased with increasing notch depth, h. The notched beam of ($0.4l$, $0.75t_{BIAS}$, 0) geometry was thin and long, allowing uniform stress distribution to develop under the notch.

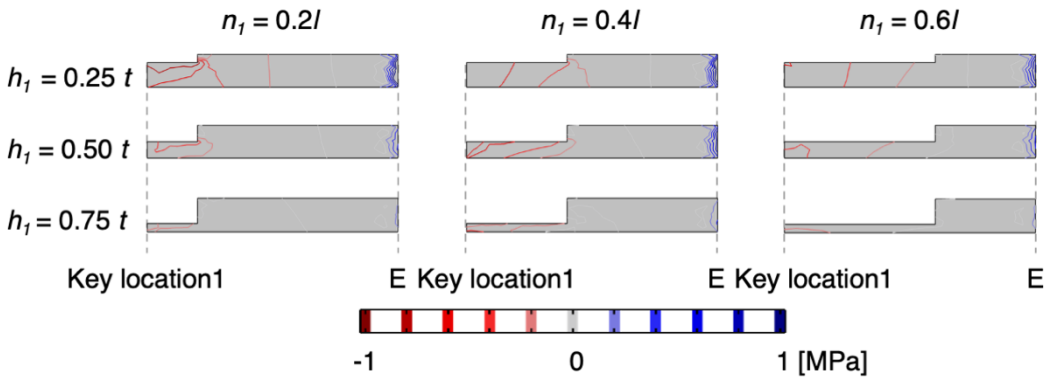

Figure 4.16: The stress distribution on the frontal surface of the beam 1 is plotted. The images were captured at the last moment of in-plane deformation

Meanwhile, although a longer length of the notched part reduced the stress concentration on the surface, increasing the depth of the notch to $h = 0.5t_{BIAS}$ resulted in a larger concentration compared to $h = 0.25t_{BIAS}$. As a result, the geometry buckled upward, while the geometry with a shallower notch buckled downwards. Additionally, the reduction in stress concentration on the notched region contributed to an increase in P_{cr} and D_{cr}. Once h was more than $0.5l$, the long notch prevented the abrupt stress change, and geometries buckled downwards. In addition, when the BIAS geometry exhibited upwards buckling, P_{cr} and D_{cr} increased as the notch became longer, decreasing when they showed downwards buckling.

Then, the distance between key location 1 and the notch was varied to reduce the stress concentration on the indented surface when narrow notches were employed, as depicted in Figure 4.17. Here, notches had $n_1 = 0.2l$ or $0.4l$, and $h = 0.5t_{BIAS}$, while dx was varied from 0 to 3 mm. Figure 4.18 presents that P_{cr} and D_{cr} increased as dx became larger when the BIAS geometry showed upwards

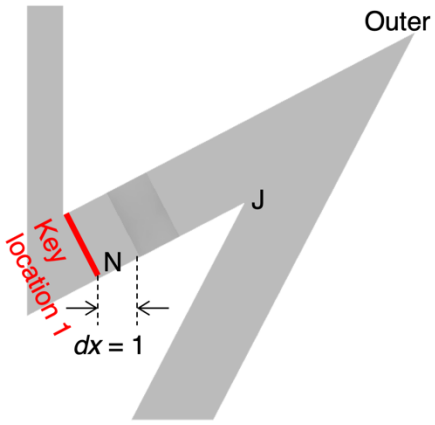

Figure 4.17: A rendering displays the top-right part of the BIAS geometry with the notch (0.2l, 0.5t, 1.0).

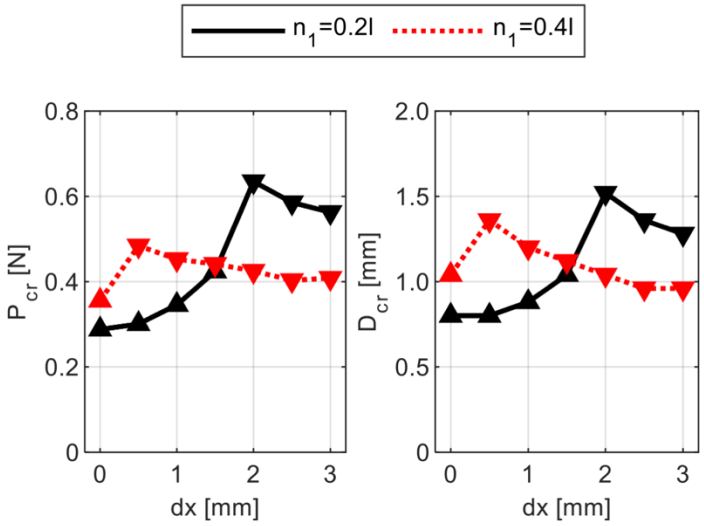

Figure 4.18: P_{cr} and D_{cr} of each unit BIAS geometry with notches on different locations were calculated through FE modeling and are plotted.

buckling, reached its maximum values when it exhibited downwards buckling, then decreased. The stress distribution in Figure 4.19 explains that inducing notches further away from the key location 1 distributed the localized

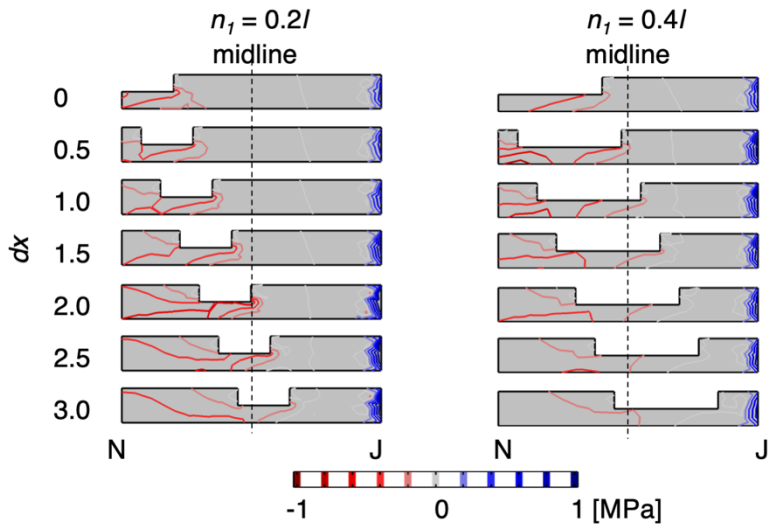

Figure 4.19: The stress distribution on the frontal surface of beam 1 is plotted. The image was captured at the last moment of in-plane deformation.

compression from the key location to the notch surface. The geometry buckled downwards when the stress was distributed over half of the beam (see (0.2l, 0.50t_{BIAS}, 2.0) and (0.4l, 0.50t_{BIAS}, 0.5) geometries in Figure 4.19). Therefore, even a slight increase in dx can make the BIAS with $n_1 = 0.4l$ buckle downwards. Although employing notches other than the key location can actuate the BIAS in a controlled manner, the efficiency in reducing P_{cr} and D_{cr} is significantly lower than employing on key location.

Last, notches were employed on the second key location on beam 2 to produce localized compression under the notches in beam 1. The location was fixed, and n_2 and h_2 of notches were varied. Notches on beam 2 decreased the stiffness and facilitated the out-of-plane deformation reducing P_{cr} and D_{cr} effectively as notches on beam 1, as depicted in Figure 4.20, since notches on facilitated the out-of-plane deformation. Moreover, all the geometries with

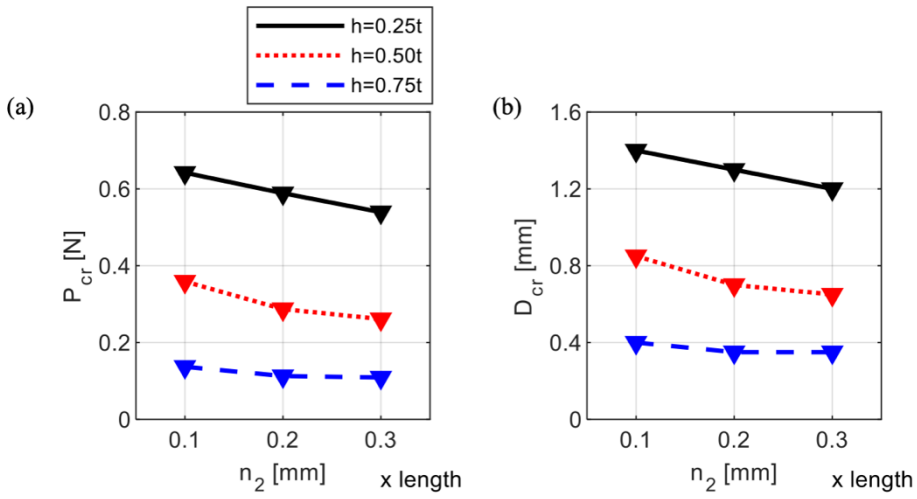

Figure 4.20: P_{cr} and D_{cr} of each unit BIAS geometry with different sizes of notches on beam 2 were calculated through FE modeling and are plotted. The BIAS geometry always buckled downwards.

notches on beam 2 buckled downwards regardless of the values for n_2 and h_2 since the localized compression was generated in the unnotched part as the notch partially allowed the free movement of beam 1, which was restrained by beam 2. (0.1l, 0.5t) in Figure 4.21 clearly shows that the localized compression was dispersed from the lower part of the beam.

4.3.4 Demonstration

The four different unit cells were used to 3D-print 8×8 BIAS arrays to demonstrate that the parametric optimization and geometrical imperfections could overcome undesirable effects such as random shape morphing directions and high critical mechanical loading due to large array configurations. The physical dimensions of the unit cell were scaled down by half since stretching an 8×8 BIAS array that large was difficult using the available load frame. Furthermore,

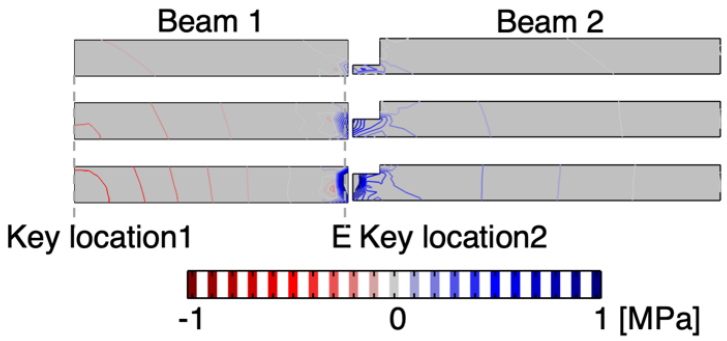

Figure 4.21: The stress distribution on the frontal surface of the beam 1 and beam 2 are plotted. The image was captured at the last moment of in-plane deformation.

print failures, such as tiny pores, burned residues, and rough surfaces, were ignored to show the dominance of notches compared to possible manufacturing defects and depicted in Figure 4.22.

The load-displacement response of a single (1 mm, 30°) BIAS geometry when it scaled down by half was calculated using FEM and plotted in Figure 4.23 to estimate the P_{cr} and D_{cr} of BIAS array. The single unit cell geometry required approximately 0.2 N of force and 0.05 of strain to exhibit out-of-plane deformation. When the number of columns in the array was increased, P_{cr} also proportionally increased. However, the number of rows in the array did not significantly affect P_{cr}. The critical strain for actuation was consistently measured at 0.05, regardless of the number of columns or rows. Based on these findings, it was estimated that the 8x8 array would need about 1.6 N of force and 6.7 mm of displacement to exhibit out-of-plane deformation.

Figure 4.22: Oozing and rough surface of printed BIAS array was captured and is illustrated.

The load-displacement response of a single (1 mm, 30°) BIAS geometry when it scaled down by half was calculated using FEM and plotted in Figure 4.23 to estimate the P_{cr} and D_{cr} of BIAS array. The single unit cell geometry required approximately 0.2 N of force and 0.05 of strain to exhibit out-of-plane deformation. When the number of columns in the array was increased, P_{cr} also proportionally increased. However, the number of rows in the array did not significantly affect P_{cr}. The critical strain for actuation was consistently measured at 0.05, regardless of the number of columns or rows. Based on these findings, it was estimated that the 8x8 array would need about 1.6 N of force and 6.7 mm of displacement to exhibit out-of-plane deformation.

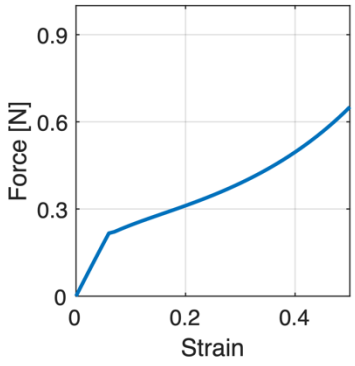

Figure 4.23: Load-displacement responses of the (1 mm, 30°) BIAS geometry when scaled down to half.

Each 8×8 BIAS array with the four different unit cells was subjected to uniaxial tension strains to 15% while simultaneously recording their load-displacement responses, which are plotted in Figure 4.24. The points indicate the critical buckling point of each geometry. The black solid line shows the mechanical responses of 8x8 array, which aligns well with simulation data. Nevertheless, there was a small mismatch between the experimental data and simulation results. In the experiments, the array did not deform homogeneously; instead, it exhibited heterogeneous deformation, with the middle row deforming earlier than the other rows.

Figure 4.25a and b depict the configuration of the large array of unnotched arbitrary geometry (2.0 mm, 30°) and unnotched optimized geometry (2.5 mm, 35°) before and after the deformation, respectively. Both geometries showed random shape morphing directions. P_{cr} of the arbitrary geometry was lower than the optimized geometry, while it needed more D_{cr}. As previously stated, there is a

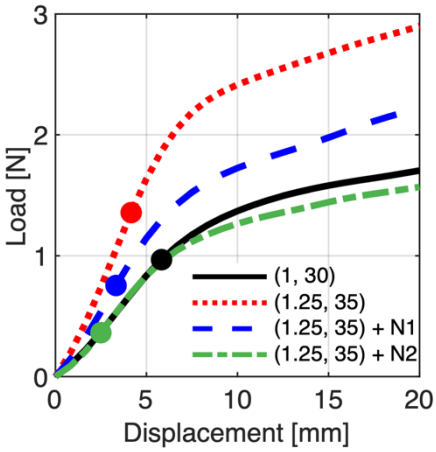

Figure 4.24: The experimental load-displacement responses of 8×8 array of BIAS with various geometries are plotted.

compromise between P_{cr} and D_{cr} due to the inverse proportionality of P_{cr} to the length of the slender element and the proportionality of D_{cr} to the length.

Employing notches at two key locations in each unit cell of a large array enabled out-of-plane deformations in a controlled manner while simultaneously reducing P_{cr} and D_{cr}. The BIAS geometry shown in Figure 4.25c had ($0.2l$, $0.5t_{BIAS}$, 0) notches on beam 1 and caused it to buckle upwards. Figure 4.25d had additional ($0.2l$, $0.5t_{BIAS}$) notches on beam 2 to cause it to buckle downwards. Although printing errors were present in a large-arrayed BIAS, the notches prevented the array from shape morphing in random directions. In addition, the presence of notches at one key location reduced P_{cr} by ~ 50% (*i.e.*, blue dashed line in Figure 4.24), while notches at both locations reduced P_{cr} by ~ 75% and D_{cr} by ~ 50% (*i.e.*, green dashed line in Figure 4.24).

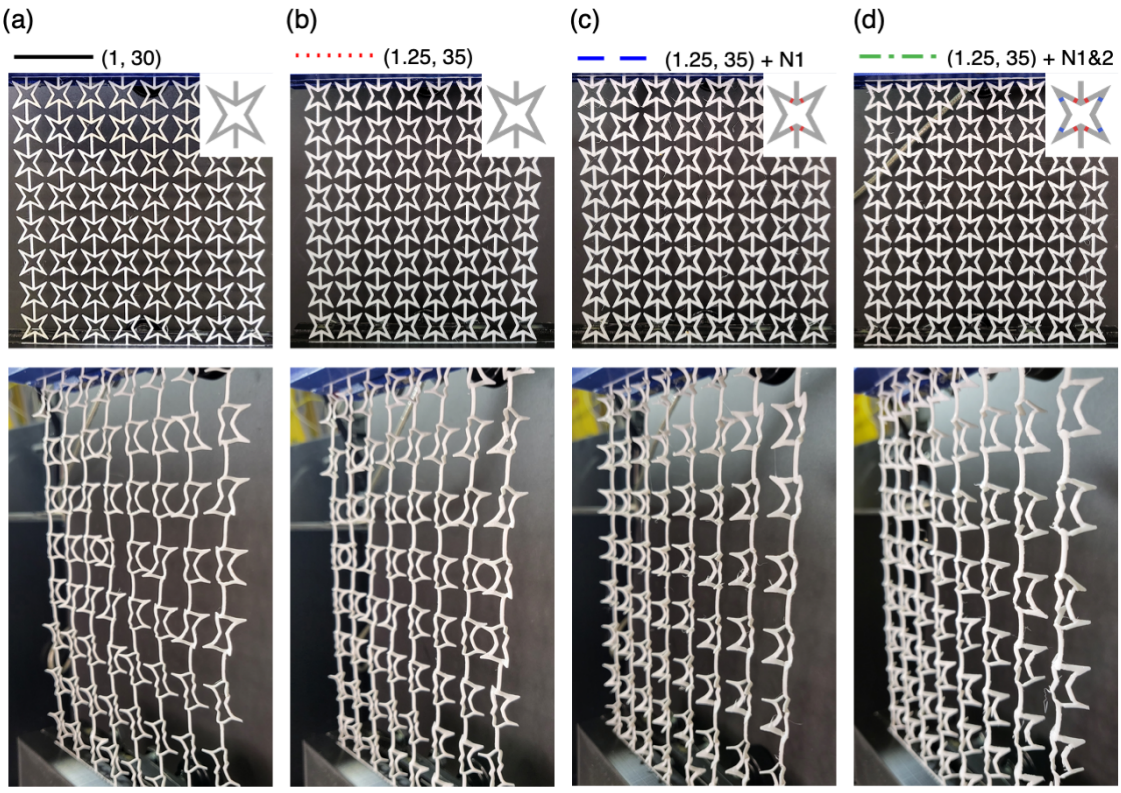

Figure 4.25: Pristine and deformed 8×8 array of BIAS with various geometries are plotted.

4.4 Conclusions

In conclusion, this chapter demonstrated a novel and effective approach to enhance the shape morphing capabilities of reentrant auxetic geometries through the judicious incorporation of designed imperfections. By introducing notches at specific key locations within the unit cells, the out-of-plane deformations of the structures were harnessed and directed, leading to controlled and predictable shape morphing responses when subjected to in-plane strains. This breakthrough was particularly significant as it addressed the long-standing challenge of unpredictable shape morphing behavior in large-array, mechanical metamaterials.

The use of designed imperfections represented a critical advancement in the field of mechanical materials. These imperfections not only enabled precise control over the shape morphing behavior but also conferred robustness against manufacturing errors and external load perturbations. This was a crucial aspect for practical applications where reliability and consistency were paramount. The ability to control the directionality and magnitude of out-of-plane deformations held immense potential for a wide range of engineering and technological applications.

One of the key achievements of this study was the optimization of BIAS geometries to achieve out-of-plane pattern deployment under minimal applied loads and displacements. This not only increased the efficiency of actuation but also opened up possibilities for alternative actuation methods beyond traditional load frames. The potential use of shape morphing materials, stimuli-responsive substances, or pneumatic actuators promised exciting avenues for future research and real-world applications.

In essence, this work pioneered a new frontier in the development of mechanical materials with controlled and programmable shape morphing responses. The ability to eliminate unpredictable behavior and reduce critical loading requirements presented transformative opportunities in fields such as robotics, aerospace engineering, architecture, and beyond. As this research set the stage for future investigations, further studies will explore the full potential of these optimized structures and delve into their applications across various domains. The synergistic integration of designed imperfections and advanced actuation methods has the potential to revolutionize shape morphing technology and lead to unprecedented breakthroughs in engineering and design.

Chapter 4, in part, is a reprint of the material as it appears in MRS Advances 2020, Park, Yujin; Loh, Kenneth J., Materials Research Society, 2020, and has been submitted for publication of the material as it may appear in Journal of Materials, 2023, Park, Yujin; Loh, Kenneth J. The dissertation author was the primary researcher and author of this paper.

CHAPTER 5: Design of Passive Antenna Tags using BIAS

5.1 Introduction

Man Overboard (MOB) is a significant and perilous event, consistently ranked among the top five primary accidents reported to the U.S. Coast Guard [4]. In 2020 alone, there were over 300 reported incidents, resulting in the loss of more than 300 lives or severe injuries. While the number of MOB incidents may be comparatively lower than other accidents like collisions and flooding, it is crucial to note that MOB incidents have the highest fatality rates. Survival chances in MOB situations are greatly influenced by time, as individuals can become unconscious within 30 min in cold water at 4.5 °C [78]. Therefore, immediate recognition of the MOB situation by individuals on board significantly increases the victim's chances of survival [47], while a lack of awareness drastically reduces those chances.

The complexity of search and rescue (SAR) operations is further compounded by the limited information available about the victim, such as their identity, time of fall, and precise coordinates. In addition, variables such as the height of the fall, water temperature, sea state, and weather conditions also impact the fatality rate [13]. Addressing this challenge involves empowering Navy sailors with the capability to promptly engage in SAR operations, providing immediate awareness of MOB situations, identification of the victim, accurate victim coordinates, and reliable signaling mechanisms without the need for battery power.

Conventional MOB detection systems typically rely on optical cameras, such as UAVs, DSLRs, and CCTV, to monitor predetermined positions within the security

perimeter [54]. However, these sensors face significant challenges in extreme weather conditions and adverse illumination, making it difficult to detect victims. Some computer vision systems have integrated thermal cameras to overcome these limitations [54]. Despite these efforts, detecting humans in the vast sea remains a challenging task due to poor visibility and interference.

To address these challenges, advanced SAR systems leverage wireless sensor networks (WSN) [98] or radio frequency (RF) technology [85]. These technologies enable contactless interrogation of sensors, making them suitable for operation in contested environments, anti-access, and area denial situations. They can trigger rescue alarms immediately after an MOB situation and provide essential victim information [47; 98]. While wireless sensors require batteries for operation, they can monitor various physical quantities, including humidity, temperature, pressure, and the victim's physiological performance [98]. Passive RF sensors, in particular, offer promise in harsh environments. They are battery-independent and can measure physical quantities with acceptable sensitivity and resolution, allowing for low-cost installation and real-time monitoring [8; 127]. Passive RF sensors have been successfully utilized in extremely cold/hot temperatures [79], and even underwater monitoring [109]. However, their effectiveness relies on strong signals from the reader, which can limit their potential [53].

This chapter aimed to develop a wearable, passive, antenna patch that changes shape (and thus its antenna signature) when a sailor falls overboard, and the identity, location, and condition of the sailor can be quickly determined using remote sensing. The antenna patch leveraged preliminary results that demonstrate feasibility of this concept. In particular, the design principles for additively manufacturing 2D patterned structures

that exhibit shape morphing in the form of out-of-plane deformations when subjected to uniaxial strains [86; 87] was leveraged. Termed Active Skins, these materials were optimized with designed imperfections that can exhibit 2D-to-3D shape transformation at low levels of critical stresses and strains. An advantage of lowering the stress/strain threshold for shape morphing is so that stimuli-responsive materials can be incorporated to promote stimuli-dependent shape morphing.

When activated by desired stimuli (*e.g.*, exposure to seawater, temperature change, and other physiological parameters), the morphed shape would result in a unique antenna electromagnetic signature that could be detected by a remote reader system mounted on a manned/unmanned ship, helicopter, aircraft, or buoy. Here, various smart materials (*i.e.,* stimuli-responsive hydrogels and SMPs) and corresponding shape morphing strategies will be introduced.

5.1.1 Temperature-responsive hydrogels

Hydrogels are three-dimensional polymer networks composed of hydrophilic polymer chains. These chains have the ability to reversibly swell or deswell in water until reaching a state of thermodynamic equilibrium [58]. The stimuli-responsive properties of hydrogels highly depend on the monomers and crosslinking methods incorporated into hydrogels. Among them, temperature-responsive hydrogels have gained significant attention for their potential applications in [57], tissue engineering [64], and drug delivery [90]. These hydrogels exhibit a reversible transition from a hydrophilic to hydrophobic state above/below a critical temperature leading to a significant shrinkage of gel.

Researchers have utilized this property to create locally programmable degrees of growth, enabling the development of 3D structures with specific morphologies and motions [83]. Additionally, composite hydrogel architectures containing oriented cellulose fibrils have been employed to create printed filaments with anisotropic stiffness, resulting in differential swelling behavior between the transverse and longitudinal directions [44]. Another approach is using a fiber-reinforced hydrogel that was designed by selectively photopolymerizing a sheet of poly(N-isopropylacrylamide) (PNIPAM) hydrogel to create a bending and rotation of the structure [119].

5.1.2 Magnetic-responsive hydrogels

Magnetically responsive materials offer a range of benefits, including safe, fast, reversible, and complex shape morphing. Recent advancements in magnetic field control have enabled the spatial distribution of magnetic micro/nanoparticles within soft compounds [3; 24; 51; 55; 56]. Above the Curie temperature, these magnetic materials undergo a significant change in their magnetic properties, allowing for the reorientation of embedded ferromagnetic particles [3]. This enables the directional actuation of each segment under a magnetic field, leading to nonuniform deformation. For example, a 3D-printed silicone-based soft materials that exhibited rapid transformation through magnetic actuation was obtained by placing a permanent magnet around the dispensing nozzle during printing to reorient the ferromagnetic particles within each domain [56].

5.1.3 Photo-responsive hydrogels

Photo-responsive polymers possesses remote control and rapid switching of properties. These polymers respond to absorbed light intensity, allowing for precise and delicate control. A 3D-printed photo-responsive shape memory devices has been achieved by mixing polyurethane filament with carbon black, which has excellent photothermal conversion efficiency. The material thickness and light density on programming the shape memory behavior determined the performance of these devices [124].

Although this approach has led to controllable shape-shifting, they are only limited to certain materials or chemical compositions [31]. Specifically, the achievable designs are limited and do not leverage the overall geometrical configuration for controlling their morphology, especially as these structures change how they interact with their variable surroundings. Therefore, mechanical metamaterials that leverage the geometrical instabilities can broaden the application of smart mart materials.

5.1.4 Shape memory polymers

Unlike stimuli-responsive polymer, SMPs require a programming process for volume change under stimulus [60]. During this process, the material is subjected under the mechanical stress at the temperature above a transition temperature to align the polymer chains along the direction of applied stress.

Then, the deformed structure is cooled down and remained until exposed to external stimulus to go back to its initial state.

Mao et al. [72] reported a hydrogel sandwiched structure between a layer of SMP and elastomer. The high stiffness of SMP and elastomer in cold water constrains the swelling of hydrogel, thus, the structure remains in as-printed state. The structure was bent in hot water, since the stiffness of SMP decreased and allows the large shape changes of hydrogel, while elastomer keeps constraining it. Then the structure was cooled down to program the SMP and maintain the deformed configuration until it was dried at high temperature to recover the as-printed shape.

Thermo-responsive polymers have wide application fields such as in intelligent medical devices [6], packages for sensor and micro-systems [91], and self-assembling systems [73; 129]. Manen et al. [114] programmed the 3D printed PLA that can shrink in longitudinal direction and expand in both other directions. The shrinkage rate of polymer in length can be manipulated by changing the printing parameters (*i.e.,* infill density, pattern, and layer thickness) and various 3D shapes was attained by combining this strategy with origami, and sequential shape shifting.

5.2 Materials and Methods

5.2.1 Fabrication of 3D-printed samples

The Active Skin skeleton geometries were first converted into STL mesh files and then imported into Ultimaker Cura 5.4 software for 3D printing. To create physical models, TPU 95A filament was used as the printing material, and an Ultimaker 3+ FDM 3D printer was employed. The printing temperature was set to 220 °C, and the printing speed was set at 10 mm/s. For maximum structural integrity, the infill density was set to 100%, utilizing a line pattern to achieve this configuration. A layer thickness of 0.1 mm was chosen to ensure fine and precise printing details.

5.2.2 Fabrication of PDMS

For obtaining hyperelastic material parameters of PDMS, a tensile test sample was prepared following ASTM D638 type IV standards. The goal was to use these parameters in finite element simulations for the BIAS star geometry used in the passive antenna. The PDMS base material was prepared by adding 1.8 wt% benzophenone to reduce its hydrophobicity. To facilitate mixing, the benzophenone, which is solid at room temperature, was liquefied at approximately 80 ℃ before being added to the PDMS. The mixture was then homogenized using a FlackTek speed mixer at 3,000 rpm for 2 minutes. Subsequently, 5 wt% PDMS cross-linker was added and mixed for 5 minutes at 1,000 rpm to prepare the PDMS prepolymer. To ensure air removal, the prepared

prepolymer was transferred into a syringe and centrifuged at 3,000 rpm for 20 minutes before being used for casting.

For the casting process, a custom-designed mold for each tensile specimen and BIAS star geometry was created using Fusion 360 software. The molds were 3D-printed using TPU 95A on an Ultimaker 3+ FDM printer. To facilitate demolding, a layer of petrolatum was applied to the mold before depositing the PDMS prepolymer. The PDMS was then cured at 80 ℃ for an hour to achieve the desired material properties.

5.2.3 Fabrication of NC-PNIPAM

To prepare the N-isopropyl acrylamide (NIPAM) solution (2 M) and N-N'methylenebisacrylamide (MBA) solution (0.13 M), NIPAM and MBA were separately dissolved in deionized water. The dissolution process occurred at room temperature, and the solutions were mixed using a speed mixer until all the chemicals were completely dissolved. Next, a mixture was prepared by combining 10 mL of the NIPAM solution (2 M), 120 μL of the MBA solution (0.13 M), 0.04 g of Irgacure 2959, and 1 g of Nano Clay (NC) in a 40 mL container from a FlackTek speed mixer. The mixture was then stirred at 2000 rpm for 5 minutes or longer until it achieved a homogeneous consistency, without any visible NC aggregates.

5.2.4 Numerical modeling

Experimentally calibrated FE simulations using COMSOL Multiphysics were created to determine the optimal width of the BIAS geometry for inducing 3D deformations. However, properties of the PDMS substrate were needed to define the COMSOL hyperelastic numerical model. Therefore, the tensile test load-displacement data of PDMS was converted to stress-stretch and fitted using nonlinear least-square regression to obtain the five Mooney-Rivlin parameters. The five Mooney-Rivlin parameters are listed in Figure 5.1 and were used for parametric optimization in COMSOL Multiphysics. One end of the BIAS star geometry was fixed, and uniaxial tension was applied to the opposite end to induce a 50% strain in the star geometry. The load-displacement behavior of each geometry was captured during this process.

5.3 Results and discussion

5.3.1 Optimization of different configurations

Various re-entrant geometries were employed to demonstrate the applicability of the design principles of the BIAS geometry to other re-entrant geometries. First, a re-entrant star geometry with five tips was utilized. Figure 5.1 illustrates the re-entrant geometry with five tips used in the FE model, where the length of r_1 was fixed at 10 mm while r_2 and w_{STAR} were varied. The angles formed by the five tips were maintained constant throughout. The

Table 5-1: Mooney-Rivlin Parameters of PDMS

C_{01} [MPa]	C_{10} [MPa]	C_{11} [MPa]	C_{02} [MPa]	C_{20} [MPa]	Density [kg/m^3]
0.023	0.035	-0.149	0.047	0.142	965

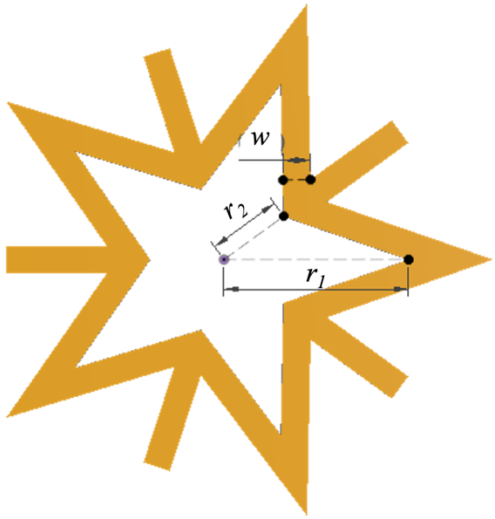

Figure 5.1: A unit cell Active Skin star geometry configuration is illustrated.

resulting geometries for different variations of r_2 and w_{STAR} are depicted in Figure 5.2. It was observed that the length of the slender elements was inversely proportional to the values of r_2 and w_{STAR}.

Critical displacements and forces required for 3D morphing were calculated using the FE model to determine the most optimal geometry. Four tips of the five-tip re-entrant geometry were fixed, while uniaxial tension was applied to a single tip. The displacements (D_{cr}) and forces (F_{cr}) when the tip of the five-tip re-entrant geometry moved in the out-of-plane direction were presented in Figure 5.3. F_{cr} increased when the re-entrant geometry has a longer r_2 and wider w_{STAR}.

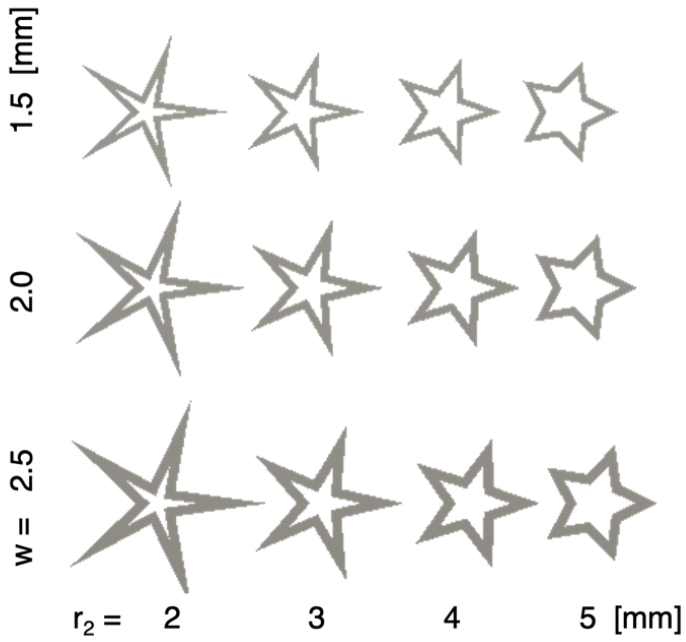

Figure 5.2: Active Skin geometries with different w_{STAR} and r_2 are illustrated.

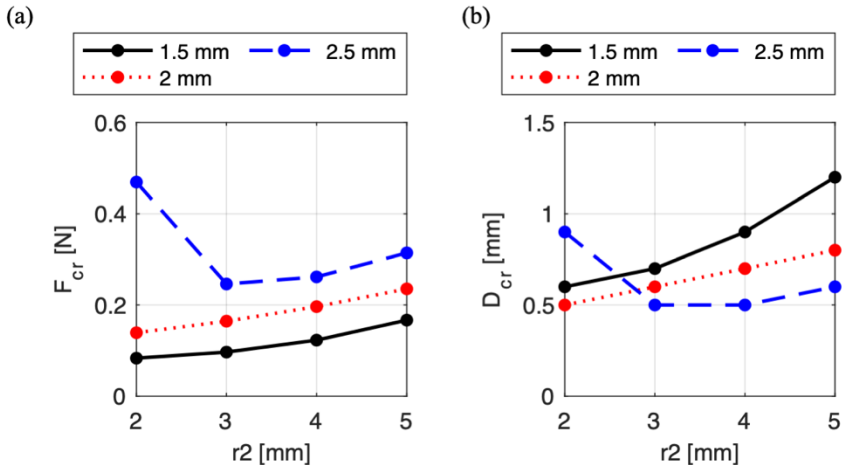

Figure 5.3: (a) P_{cr} and (b) D_{cr} of each unit Active Skin geometry with different sized notches were calculated through FE modeling and are plotted.

However, it was observed that the geometry with w_{STAR} = 2.5 mm and an r_2 = 2 mm did not follow this tendency. Instead, this particular geometry behaved more like bulk material, indicating that the free-hinge motion of the compressed bar was not isolated as expected and required large force and displacement for actuation.

On the other hand, D_{cr} increased when the re-entrant geometry had a longer r_2 and narrower w_{STAR}. In particular, when beams were designed shorter in length yet broader in width, they generated significantly larger forces even when the displacement remained constant. Moreover, as the value of r_2 increased, the angle formed between the two adjacent compressed beams also augmented. This relationship between r_2 and the angle played a pivotal role in producing larger forces at the same displacement. contributed to the generation of a larger force at the same displacement. These findings demonstrated the influence of the geometric parameters on the critical displacement and force of the re-entrant geometry.

In addition to optimization, notches were deliberately introduced onto the surface of the Active Skin to investigate their influence. The notches, which were larger than half the length of the slender elements, were induced on the Active Skin geometry with w_{STAR} = 2.5 mm and r_2 = 2 mm, which initially exhibited behavior similar to bulk material. Without notches, this geometry demonstrated random deformation, with the left and right tips buckling in opposite directions as shown in Figure 5.4a. However, by introducing notches like Figure 5.4b, the buckling direction of the Active Skin could be controlled (see Figure 5.4c).

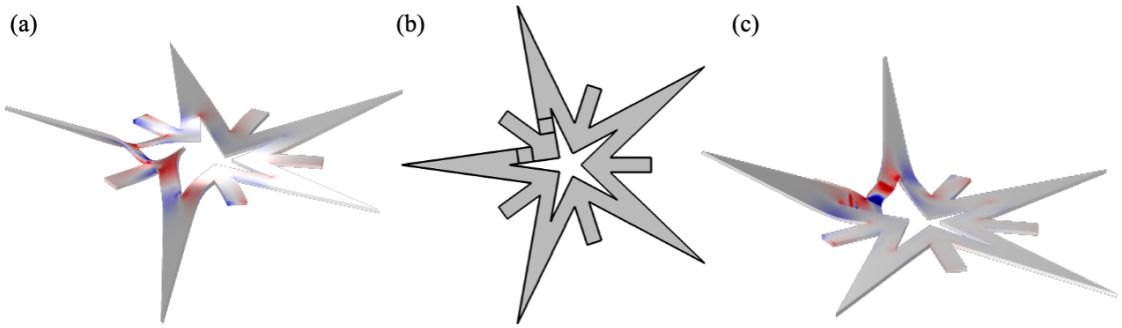

Figure 5.4: A rendering of (a) random deformation of Active Skin (w_{STAR} = 2.5 mm, r_2 = 2.0 mm) is depicted. (b) Active Skin with notches on slender beam is illustrated. (c) Active Skin deformed in controlled manner is presented.

Inducing notches on Active Skin resulted in a reduction in the critical force, displacement, and overall actuation force and displacement as shown in Figure 5.5. Additionally, the unnotched geometry, which behaved like bulk material (w_{STAR} = 2.5 mm, r_2 = 2.0 mm), was able to leverage the desired free-hinging motion. This experimental exploration highlighted the significance of notches in controlling the deformation behavior and actuation characteristics of the re-entrant geometry.

The simulation results were compared to experimental data in order to validate the reliability of the simulations. The selected geometry had w_{STAR} of 1.5 mm, while the value of r_2 was varied. Figure 5.6 presents the comparison between the simulation and experimental results for F_{cr} and D_{cr} of each geometry. It was observed that the critical displacement and force obtained from the experimental results closely corresponded to the simulation results. In addition, the deformed geometry observed in the experiments was found to be consistent with the simulated results (see Figure 5.7). This strong agreement between the

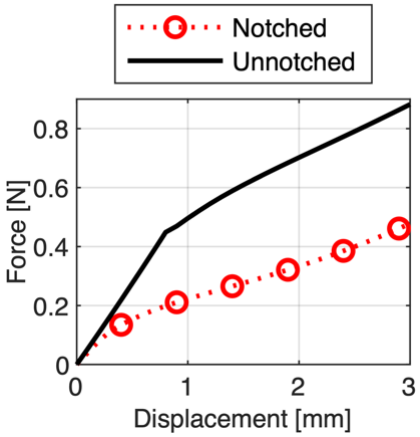

Figure 5.5: Force-displacement response of unnotched and notched Active Skins are illustrated.

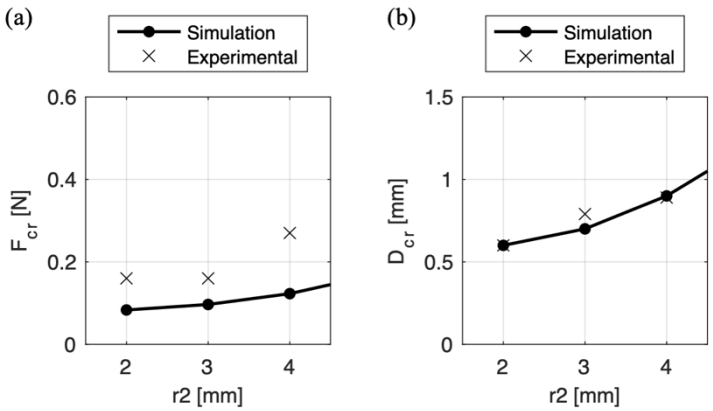

Figure 5.6: (a) P_{cr} and (b) D_{cr} of unit Active Skin geometry with w_{STAR} = 1.5 mm and different sized r_2 were calculated through FE modeling and measured.

experimental and simulation findings provide further validation of the simulation model's accuracy and demonstrates its ability to accurately predict the behavior of the tested geometries.

The design principle of Active Skin was further validated by applying it to the Navy Commander (O-4/O-5) oak leaf insignia, demonstrating its applicability to various re-entrant geometries. The oak leaf insignia, which consists of seven re-

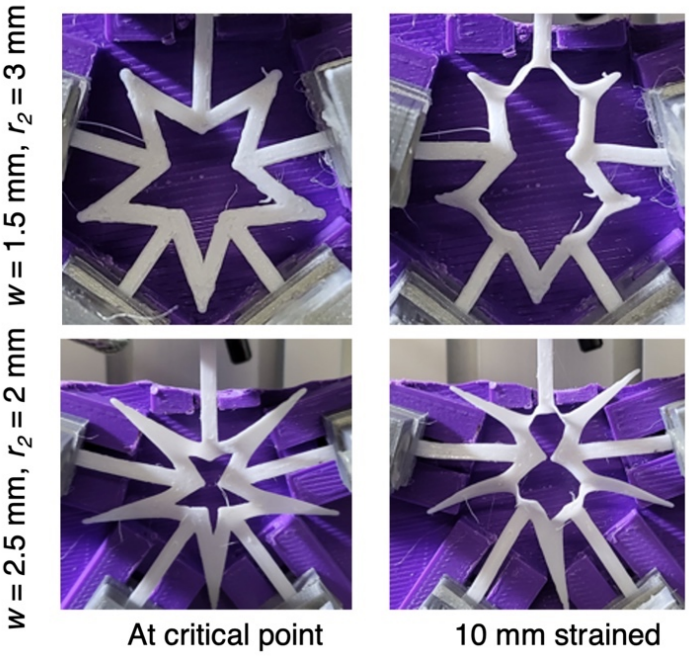

Figure 5.7: Images of Active Skin taken during the tensile test when four of five tips were affixed are illustrated.

entrant features, was modified by connecting each feature to a gripping bar. This enabled the application of tension to actuate the individual features. Figure 5.8 illustrates the oak leaf insignia with gripping bars, showcasing the response of the geometry when tension was applied to one, two, and three of the seven gripping bars. This validation is significant as it highlights the potential to design passive tags that can react to seven different stimuli by connecting each gripping bar to respond to a specific stimulus. This further supports the versatility and adaptability of the Active Skin design principle for creating responsive structures in various applications.

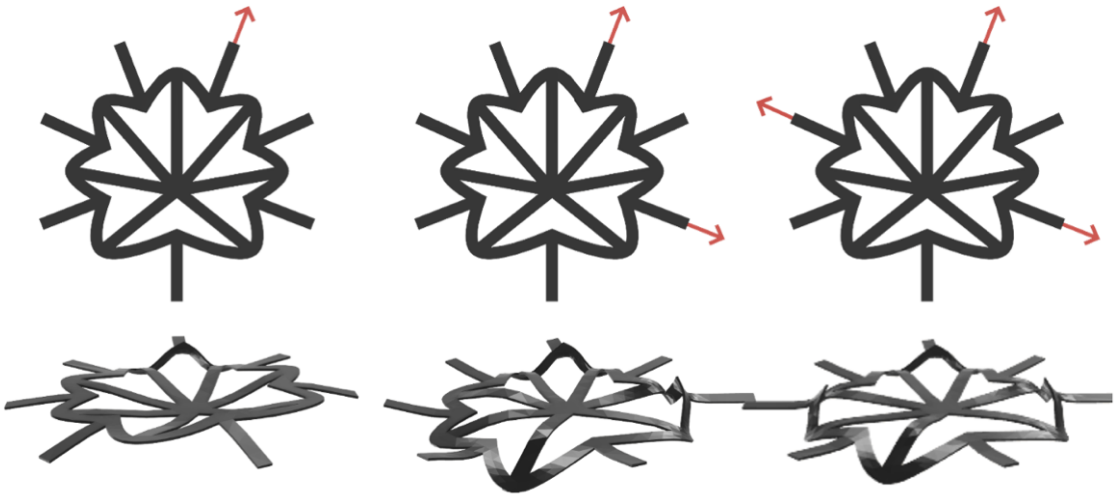

Figure 5.8: A rendering of Active Skin based on Navy oak leaf insignia when the tension was applied on one, two, three directions are illustrated.

5.3.2 Actuation method #1: Stimuli-responsive polymer

Various actuation methods were investigated to broaden the potential applications of Active Skin, a versatile material with shape-morphing capabilities. One notable approach involves utilizing SRP to apply tension to the structure. In this method, the gripping bars are connected to SRP, which exhibits contraction under specific stimuli (see Figure 5.9). By affixing the two ends of the SRP to the gripping bars, the contraction of the SRP can actuate the pattern and induce desired deformations in the Active Skin.

In this study, a specific combination of SRP was employed, namely PNIPAM mixed with Nano Clay (laponite-RD). PNIPAM is known to exhibit a volume change at around 32 ℃. However, due to its inherent low strength and brittleness, the inclusion of nano clay was necessary to enhance the ductility and mechanical properties of the material. The addition of Nano Clay improved the

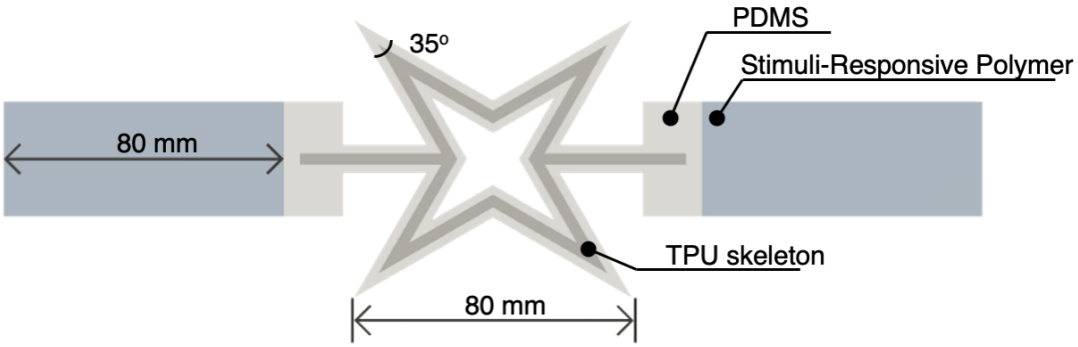

Figure 5.9: A schematic of the passive BIAS geometry using SRP is depicted.

overall performance of the Active Skin, enabling it to withstand higher levels of strain and deformation without compromising its integrity.

To fabricate the passive BIAS geometry, polydimethylsiloxane (PDMS) was utilized as the primary material. PDMS offers several advantages, including its flexibility, ease of fabrication, and compatibility with SRPs. To ensure effective bonding between PDMS and PNIPAM, a small amount (1.8 wt%) of benzophenone was added to initiate free radical polymerization upon exposure to ultraviolet (UV) light. This bonding process allowed for a strong and reliable connection between the two materials, enabling the integration of the SRP-based actuation mechanism into the BIAS geometry.

First, FE simulations were performed to identify the optimal width (w_{BIAS}) that promoted 3D deformations or shape morphing of the BIAS star geometry. Figure 4.1 shows the top and side views of both the pristine and deformed states of a BIAS star geometry, along with the dimensions used in the FE model. The outer tip spacing ($2H$), rib angle (θ), and thickness (t_{BIAS}) were fixed at 80 mm, 35°, and 3 mm, respectively. The 35° rib angle was determined as optimal in

previous chapter. When uniaxial strain was applied to the BIAS star geometry, localized compression was induced on the beam between the inner and outer tips. Buckling occurred when this compression exceeded the F_{cr} of the beam. When the w_{BIAS} was greater than the t_{BIAS}, buckling occurred in the out-of-plane direction, allowing for 3D deformations to occur. Previous chapter also showed that, when the length of the notch applied to the beam exceeded 50%, it was possible to control buckling orientation in the opposite direction of the indented surface. Therefore, in this chapter, notches with a length of 50% of the beam's length and a depth of 2/3 of the thickness were always created, followed by parametric optimization with respect to width.

The out-of-plane buckling instability of the BIAS star geometry was inversely proportional to w_{BIAS}. When the BIAS star geometry was stretched, the outer and inner tips move in the out-of-plane direction. The distance between these tips is referred to as h_{tips} (see Figure 4.1). As it strained, h_{tips} gradually increased, reached a maximum, and then decreased again. The point of reaching the maximum value is known as full deployment. Figure 5.10 displays the strain and force required for BIAS star geometry to reach full deployment. Geometries with w_{BIAS} = 3 and 4 mm did not reach full deployment at 50% strain. However, geometries with w_{BIAS} = 5 to 7 mm reached full deployment within 40% strain. The required strain decreased as w_{BIAS} increased, while BIAS star geometries with a wider w_{BIAS} required greater forces because of their higher stiffness. In addition, Figure 5.11 illustrates the deployment of BIAS geometries with w_{BIAS} = 4 and 6 mm as a function of strain. BIAS with a

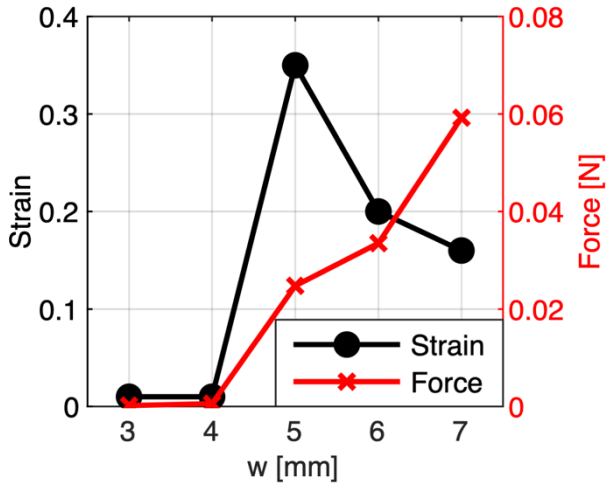

Figure 5.10: Strain and force required at full deployment of the BIAS star geometry with various w_{BIAS} is plotted.

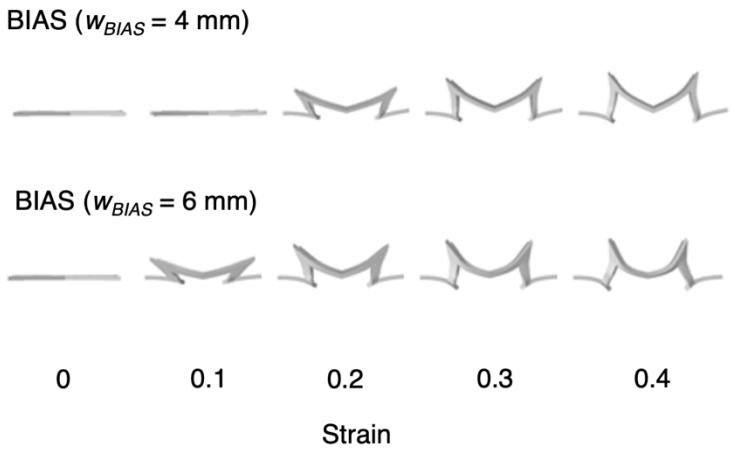

Figure 5.11: The deployment of BIAS star geometry with various w_{BIAS} was captured in a side view.

wider w_{BIAS} achieved full deployment and experienced out-of-plane deformation at a lower strain. Although all BIAS star geometries with w_{BIAS} ranging from 5 to 7 mm shape morphed at below 40% strain, the geometry with w_{BIAS} = 6 mm, which

demanded relatively lower strain and force, was identified as the most optimal geometry for the antenna application.

and submerged in room temperature water (20 ℃) for a duration of 24 hours. Subsequently, they were exposed to a temperature range of 22 to 42 ℃, as depicted in Figure 5.12. To prevent evaporation and potential sample dehydration, each hydrogel disk was placed and sealed within a Petri dish during the measurement process. Diameter measurements of the disks were taken at every temperature point to monitor and record any changes in size.

In the design of a passive BIAS pattern, the deswelling behavior of the hydrogel was carefully examined. Hydrogels were fabricated into 15 mm disks and submerged in room temperature water (20 ℃) for a duration of 24 hours. Then, they were exposed to a various temperature range of 22 to 42 ℃, as illustrated in Figure 5.12. Each hydrogel disk was placed and sealed within a Petri dish during the measurement process to prevent evaporation and potential sample dehydration. The diameter of each disk was measured across all temperature points to track changes in size.

Figure 5.13 clearly illustrates the hydrogel's contraction behavior. Between 22 and 27 ℃, there were minimal changes in the hydrogel's size. However, around the PNIPAM's LCST temperature of 32 ℃, the hydrogel began exhibiting size reductions of approximately 5 to 10%. When exposed to the highest temperature, 42 ℃, the hydrogel contracted by roughly 20%. As illustrated in Figure 5.9, the passive BIAS tag would be integrated two hydrogel segments, each mirroring the size of the BIAS geometry, connected to opposite

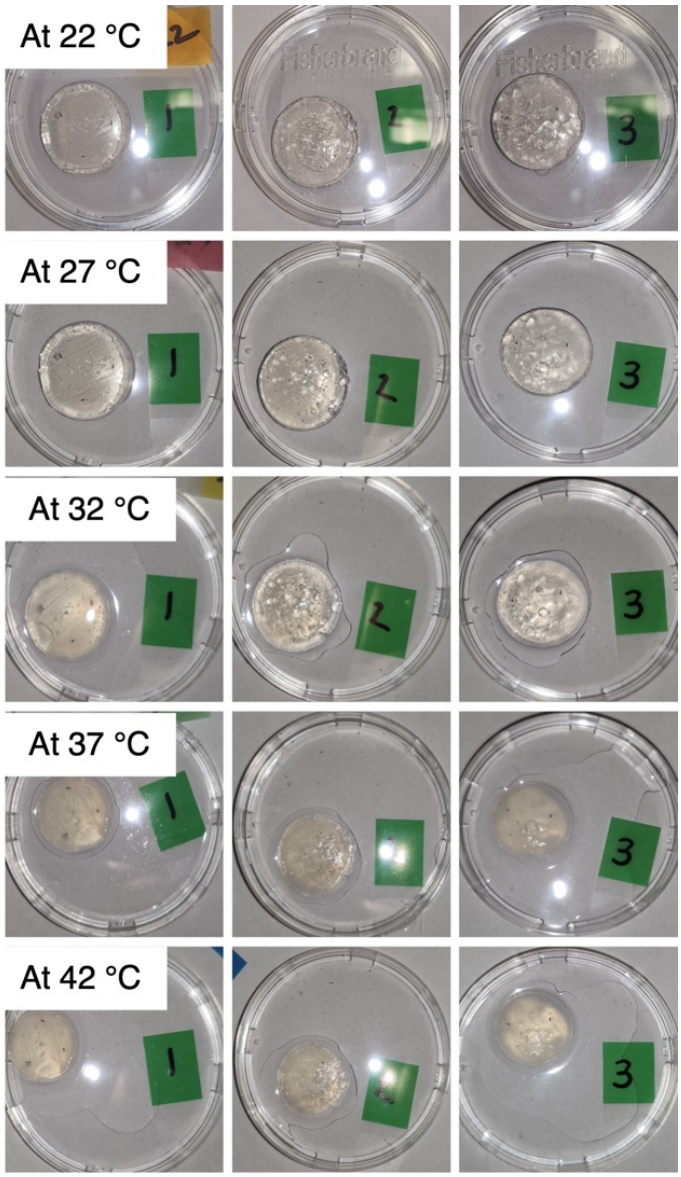

Figure 5.12: PNIPAM disks for deswelling test are showcased.

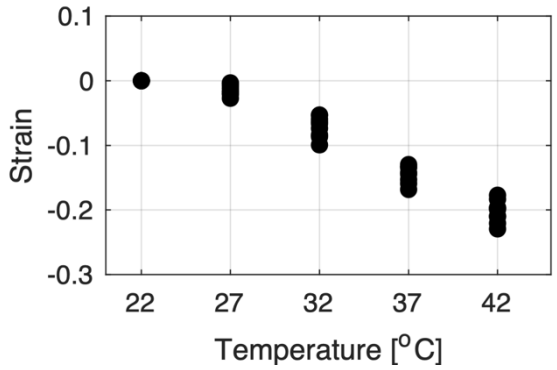

Figure 5.13: Strain of PNIPAM measured at various temperature are plotted.

sides of BIAS structure. With this design, a 20% contraction in hydrogel size could produce an effective strain of 40%, emphasizing the impressive actuation potential of the passive BIAS pattern.

The passive BIAS pattern, as presented in Figure 5.9, was fabricated using PDMS and PNIPAM, emphasizing the versatility of the design. First, the BIAS geometry was cast using PDMS and then connected to PNIPAM segments. Then, the pattern was left to immerse in room temperature water for 24 hours. After the duration, the PNIPAM segments were trimmed down to a length of 80 mm to ensure they aligned in length with the BIAS geometry. The two ends of the BIAS pattern were then securely affixed. The final pattern was subjected to temperature variations as presented in Figure 5.14, specifically 25, 32, and 40 ℃.

At 25 ℃, the BIAS pattern retained its flat configuration. However, as the temperature reached 32 ℃, the changing length of the PNIPAM began exerting strain on the BIAS, initiating its out-of-plane deformation. The deformation was even more pronounced at 40°C, indicating an increased strain compared to 32°C. Nevertheless, due to the intrinsic lower strength of the hydrogel compared to

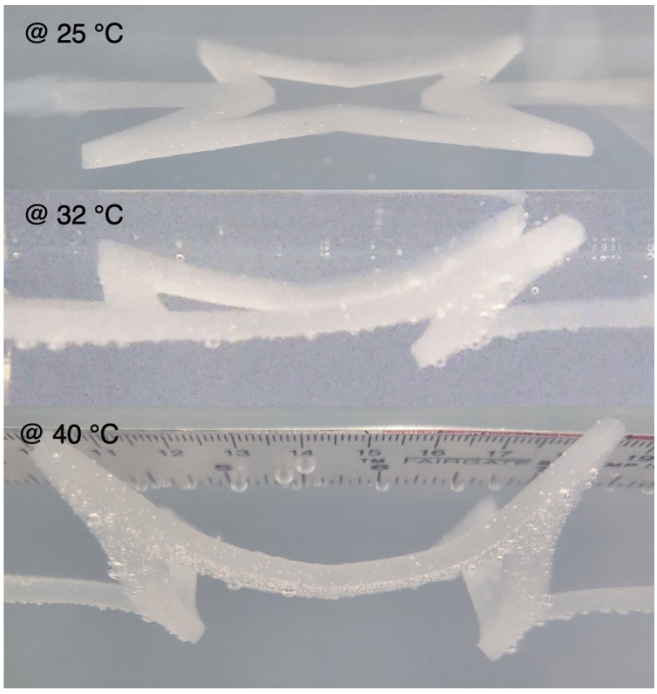

Figure 5.14: The passive BIAS pattern actuated in different temperature of water is illustrated.

PDMS, as the hydrogel contracted with the temperature increase, it also experienced a tensional force due to overall length decrease. Consequently, this real-world behavior deviated from simulation predictions, and the pattern did not achieve full deployment as anticipated.

Although the results did not fully align with the simulation predictions, these findings underscore the potential of various actuation techniques in broadening the applications of Active Skin. By employing SRP-based tensioning and utilizing PNIPAM mixed with nano clay, the material's actuation performance was greatly enhanced. The successful fabrication of the BIAS geometry using PDMS and the establishment of a strong bond between PDMS and PNIPAM further contribute to the development of Active Skin as a versatile and adaptable

material. The design of a passive BIAS pattern based on the deswelling behavior of the hydrogel exemplifies the potential for achieving controlled and reliable actuation responses under varying conditions. These advancements pave the way for the future utilization of Active Skin in various fields and applications.

5.3.3 Actuation method #2: notch integration

In addition to tension-based actuation, the use of notches provides an alternative method for actuating Active Skin. By introducing notches into the structure, F_{cr} and D_{cr} required for actuation can be reduced compared to an unnotched pattern. The reduction in force and displacement allowed for more efficient and controlled actuation. Moreover, infilling the notches with a material that can react to specific stimuli further enhances the actuation capabilities of the structure. In this study, polyvinyl alcohol (PVA) was selected as the infilling material for the notches as shown in Figure 5.15.

PVA is commonly used as a supporting material for FDM 3D printers due to its water-soluble nature. The notch of TPU coupons were filled with PVA at a density of 10% and then submerged in the room temperature water (20 °C) for 30 minutes to evaluate the dissolving rate of PVA (see Figure 5.16). Two distinct coupon designs were fabricated, one had a simple PVA infill in the notch, while the other was designed with two small tips on the notch to physically hold the PVA. The length of the PVA infill was observed and recorded throughout the immersion.

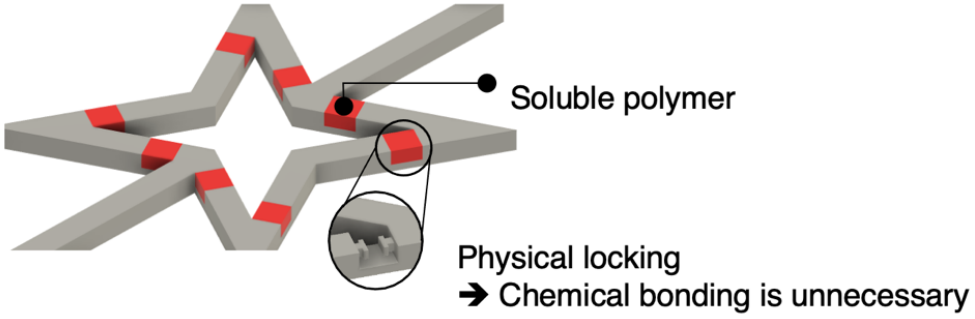

Figure 5.15: A schematic of the passive BIAS geometry using infilled notches is depicted.

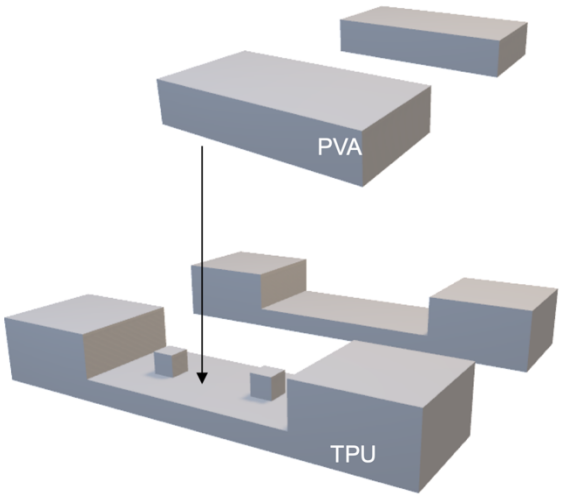

Figure 5.16: A rendeirng of PVA-TPU coupon for water dissolving test is illustrated.

Figure 5.17 displays dissolving rate of PVA in TPU coupons. The PVA remained anchored within the notch, independent of its physical retention. Both design variations exhibited consistent dissolving patterns. The initial 10 minutes showed negligible changes in the PVA length, but subsequent observations identified a progressive reduction. As the immersion period extended, the dissolution rate of PVA increased. By the end of the 30-minute interval, the PVA had not fully dissolved. The complete dissolving of PVA is not a prerequisite for actuating the notch effect. Even the mere dissolving of the PVA segment that supports the notch would permit the notch to govern deformation. Based on these findings, the use of PVA as an actuation mechanism is deemed viable.

Figure 5.18a showcases the resulting notched BIAS structure filled with PVA after fabrication. The pattern was pre-strained to 10% and both ends were affixed to ensure stability. The prepared structure was then immersed in room temperature water (22 °C). Figure 5.18b showcases the actuation process of BIAS. After 12 minutes, one tip of the BIAS structure was successfully actuated. Subsequently, after 20 minutes, another tip of the structure underwent actuation. These results demonstrate the effectiveness of the notched design and the use of PVA infilling in achieving controlled and sequential actuation of the Active Skin structure.

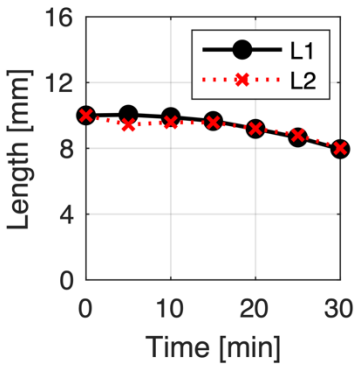

Figure 5.17: Dissolving rate of PVA was recorded at room temperature and is presented.

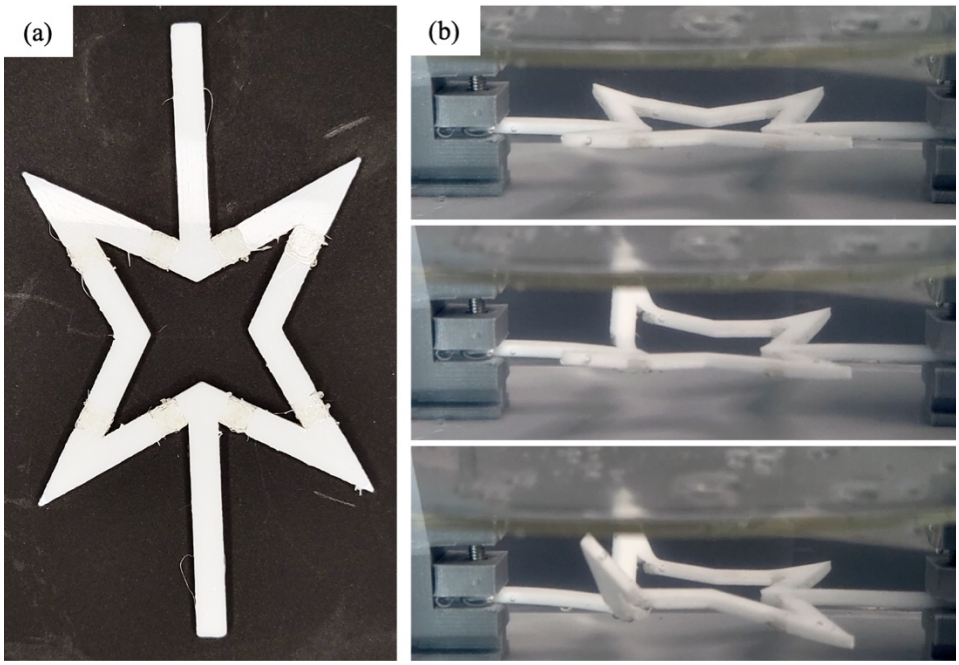

Figure 5.18: (a) Image of notched BIAS pattern with PVA infilled is illustrated. (b) Pre-strained BIAS pattern immersed in the water at 0, 13 and 20 min is showcased.

Overall, the combination of notches and infilling with PVA provides a promising approach to achieve actuation in Active Skin. The reduction in critical force and displacement, along with the stimuli-responsive nature of the PVA infill, allows for precise and controlled deformations of the structure. Further exploration of different infilling materials and notch designs can expand the capabilities of Active Skin in various applications that require tunable and responsive shape morphing.

5.4 Conclusion

In conclusion, the BIAS design principle has been successfully applied to various re-entrant geometries, demonstrating its versatility and potential for broadening the applications of Active Skin. Through the exploration of different actuation methods, such as tension application through the use of stimuli-responsive polymers, the Active Skin structure has shown the ability to undergo controlled shape morphing and actuation. The incorporation of notches and infilling with materials like PVA has further enhanced the actuation capabilities of Active Skin, allowing for reduced critical forces and displacements.

The results obtained from these investigations validate the effectiveness of the BIAS design principle in achieving desired actuation responses in different geometries. By connecting gripping bars to stimuli-responsive polymers or infilling notches with responsive materials, the Active Skin structure can be tailored to react to specific stimuli and environments. This opens up possibilities for the development of passive tags that can respond to multiple stimuli or conditions.

These findings contribute to the advancement of shape-morphing materials and their potential applications in fields such as wearable devices, robotics, and biomedical engineering. The ability to achieve controlled and sequential actuation in Active Skin structures holds promise for the development of adaptable and responsive systems. Further research and development in this area can lead to the creation of innovative devices and structures with enhanced functionality and performance.

In summary, the application of the BIAS design principle to various geometries and the exploration of different actuation methods have provided valuable insights into the capabilities of Active Skin. These findings pave the way for the design and development of intelligent materials that can adapt to changing conditions and stimuli, enabling new possibilities in diverse fields of technology and engineering.

Chapter 5, in part has been submitted for International Workshop on Structural Health Monitoring (IWSHM) 2023, Naidu, Vishnu; Park, Yujin; Loh, Kenneth J. and currently being prepared for submission for publication of the material. Park, Yujin; Loh, Kenneth J. The dissertation author was the primary researcher and author of this material.

CHAPTER 6: Conclusion

6.1 Summary of results

The overarching aim of this dissertation was to exploit the free-hinging motion of mechanism-based, flexible, mechanical metamaterials for designing novel nonlinear-elastic functional structures and shape morphing materials. The primary goal was to achieve these unique mechanical behaviors without having to modify the chemical composition or microstructure of materials. Through three comprehensive chapters, the research aimed to demonstrate the potential applications of these innovative materials in ankle braces and shape morphing structures, as well as to explore design principles for controlled actuation and predictable shape morphing responses.

Chapter 3 focused on designing adaptive stiffness metamaterials for ankle braces. By leveraging the free-hinging motion of mechanical metamaterials, the aim was to mimic the nonlinear mechanical properties of human ligaments. The novel approach involved parametric optimization of a hexagon geometry, leading to a brace that exhibited load-free shape change during low-intensity activities and rapid stiffness increase for significant biomechanical support during high-intensity activities. The prototype brace showed superior mechanical properties and adaptability, offering the potential for injury prevention and improved ankle performance.

Chapter 4 presented a pioneering design principle for mechanical materials, offering controlled and programmable shape morphing responses using re-entrant geometry. By optimizing the BIAS geometries and incorporating notches, this research addressed the long-standing challenge of unpredictable behavior in large-array mechanical metamaterials. The potential applications of this design algorithm are far-

reaching, promising transformative opportunities in fields such as robotics, aerospace engineering, architecture, and beyond. Further research in this area will explore the full potential of these optimized structures and delve into their applications across various domains, leading to unprecedented breakthroughs in engineering and design.

Chapter 5 aimed to validate the potential of the BIAS design principle introduced in Chapter 4. Re-entrant geometries, including the re-entrant geometry with five tips and the navy oak leaf insignia, were utilized, and optimization techniques confirmed their suitability for shape morphing applications. Various actuation methods, such as tension application with stimuli-responsive polymers and infilling notches with water-dissolvable materials, were explored to showcase the BIAS design principle's effectiveness. The experiments successfully demonstrated controlled shape morphing responses for the re-entrant geometries. These findings highlight the versatility of the BIAS design principle and its potential in enabling adaptable and responsive materials.

6.2 Future work

In the future, Chapter 3's research on adaptive stiffness metamaterials for ankle braces can be expanded through additional biomechanical studies and participant trials. Conducting real-life scenarios and various physical activity trials will help validate the effectiveness of the adaptive ankle brace and its potential for injury prevention and improved performance. Moreover, further research into customizing and personalizing the adaptive stiffness metamaterials will enable the creation of ankle braces tailored to individual biomechanical needs, ensuring optimal support and comfort for each user. Additionally, the concept of adaptive stiffness metamaterials can be extended to other

joint systems, such as the knee or wrist, to provide targeted support and comfort during a broader range of biomechanical movements.

In the future, the research on Active Skin materials from Chapters 4 and 5 can be further advanced through several avenues. First, exploring multi-stimuli responsiveness in Active Skin structures will be a crucial step. Investigating new materials and design modifications that enable Active Skin to respond to multiple stimuli or environmental conditions will enhance its versatility and adaptability, allowing for more diverse and responsive applications.

In addition, future research should focus on optimizing the BIAS design principle and designed imperfections to achieve more efficient and reliable actuation responses. Exploring alternative actuation methods, such as magnetic or electric fields, will broaden the possibilities for controlled shape morphing in reentrant auxetic geometries, unlocking new opportunities for Active Skin materials. Furthermore, investigating the combination of different re-entrant auxetic geometries with designed artificial imperfections could enable multi-dimensional shape morphing responses, catering to more complex and intricate applications in fields like architecture and advanced engineering.

REFERENCES

[1] Abdullah, A. M., Li, X., Braun, P. V., Rogers, J. A., & Hsia, K. J. (2018). Self-Folded Gripper-Like Architectures from Stimuli-Responsive Bilayers. *Adv Mater*, *30*(31), e1801669. https://doi.org/10.1002/adma.201801669

[2] Ai, L., & Gao, X.-L. (2018). An analytical model for star-shaped re-entrant lattice structures with the orthotropic symmetry and negative Poisson's ratios. *International Journal of Mechanical Sciences*, *145*, 158-170.

[3] Alapan, Y., Karacakol, A. C., Guzelhan, S. N., Isik, I., & Sitti, M. (2020). Reprogrammable shape morphing of magnetic soft machines. *Sci Adv*, *6*(38). https://doi.org/10.1126/sciadv.abc6414

[4] Arguin, W. R. (2021). *2020 Recreational Boating Statistics*.

[5] Balduini, F. C., & Tetzlaff, J. (1982). Historical perspectives on injuries of the ligaments of the ankle. *Clin Sports Med*, *1*(1), 3-12. https://www.ncbi.nlm.nih.gov/pubmed/6764753

[6] Baniasadi, M., Yarali, E., Foyouzat, A., & Baghani, M. (2021). Crack self-healing of thermo-responsive shape memory polymers with application to control valves, filtration, and drug delivery capsule. *European Journal of Mechanics a-Solids*, *85*. <Go to ISI>://WOS:000587837000018

[7] Baranger, E., Guidault, P.-A., & Cluzel, C. (2011). Numerical modeling of the geometrical defects of an origami-like sandwich core. *Composite Structures*, *93*(10), 2504-2510.

[8] Baumbauer, C. L., Anderson, M. G., Ting, J., Sreekumar, A., Rabaey, J. M., Arias, A. C., & Thielens, A. (2020). Printed, flexible, compact UHF-RFID sensor tags enabled by hybrid electronics. *Scientific Reports*, *10*(1). <Go to ISI>://WOS:000578475300011

[9] Bellows, R., & Wong, C. K. (2018). THE EFFECT OF BRACING AND BALANCE TRAINING ON ANKLE SPRAIN INCIDENCE AMONG ATHLETES: A SYSTEMATIC REVIEW WITH META-ANALYSIS. *Int J Sports Phys Ther*, *13*(3), 379-388. https://www.ncbi.nlm.nih.gov/pubmed/30038824

[10] Bertoldi, K., Vitelli, V., Christensen, J., & van Hecke, M. (2017). Flexible mechanical metamaterials. *Nature Reviews Materials*, *2*(11), 1-11. https://doi.org/10.1038/natrevmats.2017.66

[11] Bhushan, B., & Jung, Y. C. (2011). Natural and biomimetic artificial surfaces for superhydrophobicity, self-cleaning, low adhesion, and drag reduction. *Progress in Materials Science*, *56*(1), 1-108. https://doi.org/10.1016/j.pmatsci.2010.04.003

[12] Brockett, C. L., & Chapman, G. J. (2016). Biomechanics of the ankle. *Orthop Trauma*, *30*(3), 232-238. https://doi.org/10.1016/j.mporth.2016.04.015

[13] Cafarelli, D., Ciampi, L., Vadicamo, L., Gennaro, C., Berton, A., Paterni, M., Benvenuti, C., Passera, M., & Falchi, F. (2022). MOBDrone: a Drone Video Dataset for Man OverBoard Rescue. *arXiv preprint arXiv:2203.07973*.

[14] Cameron, K. L., Owens, B. D., & Deberardino, T. M. (2010). Incidence of Ankle Sprains Among Active-Duty Members of the United States Armed Services From 1998 Through 2006. *Journal of Athletic Training*, *45*(1), 29-38. https://doi.org/10.4085/1062-6050-45.1.29

[15] Carneiro, V., Puga, H., & Meireles, J. (2016). Analysis of the geometrical dependence of auxetic behavior in reentrant structures by finite elements. *Acta Mechanica Sinica*, *32*(2), 295-300.
[16] Castro, C. E., Kilchherr, F., Kim, D.-N., Shiao, E. L., Wauer, T., Wortmann, P., Bathe, M., & Dietz, H. (2011). A primer to scaffolded DNA origami. *Nature methods*, *8*(3), 221-229.
[17] Chen, M., Jiang, H., Zhang, H., Li, D., & Wang, Y. (2018). Design of an acoustic superlens using single-phase metamaterials with a star-shaped lattice structure. *Sci Rep*, *8*(1), 1861. https://doi.org/10.1038/s41598-018-19374-2
[18] Cheng, Y. C., Lu, H. C., Lee, X., Zeng, H., & Priimagi, A. (2020). Kirigami-Based Light-Induced Shape-Morphing and Locomotion. *Advanced Materials*, *32*(7), 1906233.
[19] Cheung, K. C., Tachi, T., Calisch, S., & Miura, K. (2014). Origami interleaved tube cellular materials. *Smart Materials and Structures*, *23*(9), 094012.
[20] Colorado, J., Barrientos, A., Rossi, C., & Breuer, K. S. (2012). Biomechanics of smart wings in a bat robot: morphing wings using SMA actuators. *Bioinspiration & biomimetics*, *7*(3), 036006.
[21] Cotler, H. B., Chow, R. T., Hamblin, M. R., & Carroll, J. (2015). The use of low level laser therapy (LLLT) for musculoskeletal pain. *MOJ orthopedics & rheumatology*, *2*(5).
[22] Coulais, C., Kettenis, C., & Van Hecke, M. (2018). A characteristic length scale causes anomalous size effects and boundary programmability in mechanical metamaterials. *Nature Physics*, *14*(1), 40-44. https://doi.org/10.1038/nphys4269
[23] Coulais, C., Teomy, E., De Reus, K., Shokef, Y., & Van Hecke, M. (2016). Combinatorial design of textured mechanical metamaterials. *Nature*, *535*(7613), 529-532.
[24] Cui, J., Huang, T. Y., Luo, Z., Testa, P., Gu, H., Chen, X. Z., Nelson, B. J., & Heyderman, L. J. (2019). Nanomagnetic encoding of shape-morphing micromachines. *Nature*, *575*(7781), 164-168. https://doi.org/10.1038/s41586-019-1713-2
[25] Das, S., Cadirov, N., Chary, S., Kaufman, Y., Hogan, J., Turner, K. L., & Israelachvili, J. N. (2015). Stick-slip friction of gecko-mimetic flaps on smooth and rough surfaces. *J R Soc Interface*, *12*(104). https://doi.org/10.1098/rsif.2014.1346
[26] Dean, B., & Bhushan, B. (2010). Shark-skin surfaces for fluid-drag reduction in turbulent flow: a review. *Philos Trans A Math Phys Eng Sci*, *368*(1929), 4775-4806. https://doi.org/10.1098/rsta.2010.0201
[27] Dodiuk, H., Rios, P., Dotan, A., & Kenig, S. (2007). Hydrophobic and self-cleaning coatings. *Polymers for Advanced Technologies*, *18*(9), 746-750.
[28] Doherty, C., Bleakley, C., Hertel, J., Caulfield, B., Ryan, J., & Delahunt, E. (2016). Recovery From a First-Time Lateral Ankle Sprain and the Predictors of Chronic Ankle Instability. *The American Journal of Sports Medicine*, *44*(4), 995-1003. https://doi.org/10.1177/0363546516628870
[29] Domel, A. G., Domel, G., Weaver, J. C., Saadat, M., Bertoldi, K., & Lauder, G. V. (2018). Hydrodynamic properties of biomimetic shark skin: effect of denticle size and swimming speed. *Bioinspir Biomim*, *13*(5), 056014. https://doi.org/10.1088/1748-3190/aad418
[30] Domel, A. G., Saadat, M., Weaver, J. C., Haj-Hariri, H., Bertoldi, K., & Lauder, G. V. (2018). Shark skin-inspired designs that improve aerodynamic performance. *J R Soc Interface*, *15*(139). https://doi.org/10.1098/rsif.2017.0828

[31] Erb, R. M., Sander, J. S., Grisch, R., & Studart, A. R. (2013). Self-shaping composites with programmable bioinspired microstructures. *Nat Commun*, *4*, 1712. https://doi.org/10.1038/ncomms2666
[32] Evke, E. E., Meli, D., & Shtein, M. (2019). Developable Rotationally Symmetric Kirigami-Based Structures as Sensor Platforms. *Advanced Materials Technologies*, *4*(12), 1900563.
[33] Feger, M. A., Donovan, L., Hart, J. M., & Hertel, J. (2014). Effect of ankle braces on lower extremity muscle activation during functional exercises in participants with chronic ankle instability. *International Journal of Sports Physical Therapy*, *9*(4), 476.
[34] Filipov, E., Liu, K., Tachi, T., Schenk, M., & Paulino, G. H. (2017). Bar and hinge models for scalable analysis of origami. *International Journal of Solids and Structures*, *124*, 26-45.
[35] Filipov, E. T., Tachi, T., & Paulino, G. H. (2015). Origami tubes assembled into stiff, yet reconfigurable structures and metamaterials. *Proceedings of the National Academy of Sciences*, *112*(40), 12321-12326.
[36] Florijn, B., Coulais, C., & van Hecke, M. (2014). Programmable mechanical metamaterials. *Physical review letters*, *113*(17), 175503.
[37] Fraser, J. J., & Hertel, J. (2019). Joint mobility and stability strategies for the ankle. *29.2 Neurology in Orthopaedics*.
[38] Fraser, J. J., MacGregor, A. J., Ryans, C. P., Dreyer, M. A., Gibboney, M. D., & Rhon, D. I. (2021). Sex and occupation are salient factors associated with lateral ankle sprain risk in military tactical athletes. *Journal of Science and Medicine in Sport*, *24*(7), 677-682.
[39] Funk, J. R., Hall, G. W., Crandall, J. R., & Pilkey, W. D. (2000). Linear and quasi-linear viscoelastic characterization of ankle ligaments. *J Biomech Eng*, *122*(1), 15-22. https://doi.org/10.1115/1.429623
[40] Gao, H., Wang, X., Yao, H., Gorb, S., & Arzt, E. (2005). Mechanics of hierarchical adhesion structures of geckos. *Mechanics of Materials*, *37*(2-3), 275-285. https://doi.org/10.1016/j.mechmat.2004.03.008
[41] Gardner, J. P., Mather, J. C., Clampin, M., Doyon, R., Greenhouse, M. A., Hammel, H. B., Hutchings, J. B., Jakobsen, P., Lilly, S. J., & Long, K. S. (2006). The james webb space telescope. *Space Science Reviews*, *123*(4), 485-606.
[42] Geim, A. K., Dubonos, S., Grigorieva, I., Novoselov, K., Zhukov, A., & Shapoval, S. Y. (2003). Microfabricated adhesive mimicking gecko foot-hair. *Nature materials*, *2*(7), 461-463.
[43] Gillman, A., Fuchi, K., & Buskohl, P. (2018). Truss-based nonlinear mechanical analysis for origami structures exhibiting bifurcation and limit point instabilities. *International Journal of Solids and Structures*, *147*, 80-93.
[44] Gladman, A. S., Matsumoto, E. A., Nuzzo, R. G., Mahadevan, L., & Lewis, J. A. (2016). Biomimetic 4D printing. *Nat Mater*, *15*(4), 413-418. https://doi.org/10.1038/nmat4544
[45] Gooch, J. W. (2011). ASTM D638. In J. W. Gooch (Ed.), *Encyclopedic Dictionary of Polymers* (pp. 51-51). Springer New York. https://doi.org/10.1007/978-1-4419-6247-8_856
[46] Gribble, P. A., Bleakley, C. M., Caulfield, B. M., Docherty, C. L., Fourchet, F., Fong, D. T.-P., Hertel, J., Hiller, C. E., Kaminski, T. W., & McKeon, P. O. (2016). Evidence review for the 2016 International Ankle Consortium consensus statement on the

prevalence, impact and long-term consequences of lateral ankle sprains. *British journal of sports medicine*, *50*(24), 1496-1505.
[47] Gürüler, H., Altun, M., Khan, F., & Whangbo, T. (2022). Man Overboard Detection System Using IoT for Navigation Model. *71*(3), 4955-4969.
[48] Ha, S. C., Fong, D. T., & Chan, K. M. (2015). Review of ankle inversion sprain simulators in the biomechanics laboratory. *Asia Pac J Sports Med Arthrosc Rehabil Technol*, *2*(4), 114-121. https://doi.org/10.1016/j.asmart.2015.08.002
[49] Han, Z., Mu, Z., Yin, W., Li, W., Niu, S., Zhang, J., & Ren, L. (2016). Biomimetic multifunctional surfaces inspired from animals. *Adv Colloid Interface Sci*, *234*, 27-50. https://doi.org/10.1016/j.cis.2016.03.004
[50] Hawkes, E., An, B., Benbernou, N. M., Tanaka, H., Kim, S., Demaine, E. D., Rus, D., & Wood, R. J. (2010). Programmable matter by folding. *Proc Natl Acad Sci U S A*, *107*(28), 12441-12445. https://doi.org/10.1073/pnas.0914069107
[51] Hu, W., Lum, G. Z., Mastrangeli, M., & Sitti, M. (2018). Small-scale soft-bodied robot with multimodal locomotion. *Nature*, *554*(7690), 81-85. https://doi.org/10.1038/nature25443
[52] Jin, L., Forte, A. E., Deng, B., Rafsanjani, A., & Bertoldi, K. (2020). Kirigami-Inspired Inflatables with Programmable Shapes. *Advanced Materials*, *32*(33), 2001863.
[53] Joshi, G. P., & Kim, S. W. (2008). Survey, nomenclature and comparison of reader anti-collision protocols in RFID. *IETE Technical Review*, *25*(5), 234-243.
[54] Katsamenis, I., Protopapadakis, E., Voulodimos, A., Dres, D., & Drakoulis, D. (2020). Man overboard event detection from rgb and thermal imagery: Possibilities and limitations. Proceedings of the 13th ACM International Conference on PErvasive Technologies Related to Assistive Environments,
[55] Kim, J., Chung, S. E., Choi, S. E., Lee, H., Kim, J., & Kwon, S. (2011). Programming magnetic anisotropy in polymeric microactuators. *Nat Mater*, *10*(10), 747-752. https://doi.org/10.1038/nmat3090
[56] Kim, Y., Yuk, H., Zhao, R., Chester, S. A., & Zhao, X. (2018). Printing ferromagnetic domains for untethered fast-transforming soft materials. *Nature*, *558*(7709), 274-279. https://doi.org/10.1038/s41586-018-0185-0
[57] Klouda, L. (2015). Thermoresponsive hydrogels in biomedical applications: A seven-year update. *Eur J Pharm Biopharm*, *97*(Pt B), 338-349. https://doi.org/10.1016/j.ejpb.2015.05.017
[58] Koetting, M. C., Peters, J. T., Steichen, S. D., & Peppas, N. A. (2015). Stimulus-responsive hydrogels: Theory, modern advances, and applications. *Mater Sci Eng R Rep*, *93*, 1-49. https://doi.org/10.1016/j.mser.2015.04.001
[59] Kolken, H. M. A., & Zadpoor, A. A. (2017). Auxetic mechanical metamaterials. *RSC advances*, *7*(9), 5111-5129. https://doi.org/10.1039/c6ra27333e
[60] Kuang, X., Roach, D. J., Wu, J. T., Hamel, C. M., Ding, Z., Wang, T. J., Dunn, M. L., & Qi, H. J. (2019). Advances in 4D Printing: Materials and Applications. *Advanced Functional Materials*, *29*(2). <Go to ISI>://WOS:000455097900004
[61] Lakes, R. (1987). Foam Structures with a Negative Poisson's Ratio. *Science*, *235*(4792), 1038-1040. https://doi.org/10.1126/science.235.4792.1038
[62] Li, S., & Wang, K. W. (2015). Fluidic origami: a plant-inspired adaptive structure with shape morphing and stiffness tuning. *Smart Materials and Structures*, *24*(10), 105031. https://doi.org/10.1088/0964-1726/24/10/105031

[63] Lin, C., Zhang, L., Liu, Y., Liu, L., & Leng, J. (2020). 4D printing of personalized shape memory polymer vascular stents with negative Poisson's ratio structure: A preliminary study. *Science China Technological Sciences*, *63*(4), 578-588.
[64] Lin, J. B., Isenberg, B. C., Shen, Y., Schorsch, K., Sazonova, O. V., & Wong, J. Y. (2012). Thermo-responsive poly(N-isopropylacrylamide) grafted onto microtextured poly(dimethylsiloxane) for aligned cell sheet engineering. *Colloids Surf B Biointerfaces*, *99*, 108-115. https://doi.org/10.1016/j.colsurfb.2011.10.040
[65] Liu, B., Ozkan-Aydin, Y., Goldman, D. I., & Hammond, F. L. (2019, 14-18 April 2019). Kirigami Skin Improves Soft Earthworm Robot Anchoring and Locomotion Under Cohesive Soil. 2019 2nd IEEE International Conference on Soft Robotics (RoboSoft),
[66] Liu, Y., Tang, J., Wang, R., Lu, H., Li, L., Kong, Y., Qi, K., & Xin, J. (2007). Artificial lotus leaf structures from assembling carbon nanotubes and their applications in hydrophobic textiles. *Journal of Materials chemistry*, *17*(11), 1071-1078.
[67] Lovalekar, M., Abt, J. P., Sell, T. C., Wood, D. E., & Lephart, S. M. (2016). Descriptive Epidemiology of Musculoskeletal Injuries in Naval Special Warfare Sea, Air, and Land Operators. *Military Medicine*, *181*(1), 64-69. https://doi.org/10.7205/milmed-d-14-00655
[68] Lv, C., Krishnaraju, D., Konjevod, G., Yu, H., & Jiang, H. (2014). Origami based mechanical metamaterials. *Sci Rep*, *4*, 5979. https://doi.org/10.1038/srep05979
[69] Ma, J., Song, J., & Chen, Y. (2018). An origami-inspired structure with graded stiffness. *International Journal of Mechanical Sciences*, *136*, 134-142.
[70] Mailuhu, A. K., Oei, E. H., van Putte-Katier, N., van Ochten, J. M., Bindels, P. J., Bierma-Zeinstra, S. M., & van Middelkoop, M. (2018). Clinical and radiological predictors for persistent complaints five years after a lateral ankle sprain: a long-term follow-up study in primary care. *Journal of Science and Medicine in Sport*, *21*(3), 250-256.
[71] Mao, Y., Ding, Z., Yuan, C., Ai, S., Isakov, M., Wu, J., Wang, T., Dunn, M. L., & Qi, H. J. (2016). 3D printed reversible shape changing components with stimuli responsive materials. *Scientific Reports*, *6*(1), 1-13.
[72] Mao, Y., Ding, Z., Yuan, C., Ai, S., Isakov, M., Wu, J., Wang, T., Dunn, M. L., & Qi, H. J. (2016). 3D Printed Reversible Shape Changing Components with Stimuli Responsive Materials. *Sci Rep*, *6*, 24761. https://doi.org/10.1038/srep24761
[73] Mao, Y. Q., Yu, K., Isakov, M. S., Wu, J. T., Dunn, M. L., & Qi, H. J. (2015). Sequential Self-Folding Structures by 3D Printed Digital Shape Memory Polymers. *Scientific Reports*, *5*. <Go to ISI>://WOS:000360793200001
[74] Masters, I., & Evans, K. (1996). Models for the elastic deformation of honeycombs. *Composite Structures*, *35*(4), 403-422.
[75] Mattacola, C. G., & Dwyer, M. K. (2002). Rehabilitation of the ankle after acute sprain or chronic instability. *Journal of Athletic Training*, *37*(4), 413.
[76] McKeon, P. O., & Mattacola, C. G. (2008). Interventions for the prevention of first time and recurrent ankle sprains. *Clinics in sports medicine*, *27*(3), 371-382.
[77] Meng, J., Deng, Z., Zhang, K., Xu, X., & Wen, F. (2015). Band gap analysis of star-shaped honeycombs with varied Poisson's ratio. *Smart Materials and Structures*, *24*(9). https://doi.org/10.1088/0964-1726/24/9/095011
[78] Monahan, K. (2005). *Local knowledge : a skipper's reference : Tacoma to Ketchikan*. Fine Edge. Table of contents http://www.loc.gov/catdir/toc/ecip055/2004029374.html

[79] Moraru, A., Ursachi, C., & Helerea, E. (2020). A New Washable UHF RFID Tag: Design, Fabrication, and Assessment. *Sensors*, *20*(12). <Go to ISI>://WOS:000553117000001
[80] Morgan, J., Magleby, S. P., & Howell, L. L. (2016). An approach to designing origami-adapted aerospace mechanisms. *Journal of Mechanical Design*, *138*(5).
[81] Neville, R. M., Scarpa, F., & Pirrera, A. (2016). Shape morphing Kirigami mechanical metamaterials. *Sci Rep*, *6*, 31067. https://doi.org/10.1038/srep31067
[82] Newman, T. M., Gay, M. R., & Buckley, W. (2017). Prophylactic ankle bracing in military settings: a review of the literature. *Military Medicine*, *182*(3-4), e1596-e1602.
[83] Nojoomi, A., Arslan, H., Lee, K., & Yum, K. (2018). Bioinspired 3D structures with programmable morphologies and motions. *Nat Commun*, *9*(1), 3705. https://doi.org/10.1038/s41467-018-05569-8
[84] Oeffner, J., & Lauder, G. V. (2012). The hydrodynamic function of shark skin and two biomimetic applications. *J Exp Biol*, *215*(Pt 5), 785-795. https://doi.org/10.1242/jeb.063040
[85] Papapostolou, A., & Chaouchi, H. (2011). RFID-assisted indoor localization and the impact of interference on its performance. *Journal of Network and Computer Applications*, *34*(3), 902-913.
[86] Park, Y., & Loh, K. J. (2020). Surface morphing of geometrically patterned active skins. *MRS Advances*, *5*(14), 743-750.
[87] Park, Y., Vella, G., & Loh, K. J. (2019). Bio-Inspired Active Skins for Surface Morphing. *Sci Rep*, *9*(1), 18609. https://doi.org/10.1038/s41598-019-55163-1
[88] Pikul, J. H., Li, S., Bai, H., Hanlon, R. T., Cohen, I., & Shepherd, R. F. (2017). Stretchable surfaces with programmable 3D texture morphing for synthetic camouflaging skins. *Science*, *358*(6360), 210-214. https://doi.org/10.1126/science.aan5627
[89] Pikul, J. H., Li, S., Bai, H., Hanlon, R. T., Cohen, I., & Shepherd, R. F. (2017). Stretchable surfaces with programmable 3D texture morphing for synthetic camouflaging skins. *Science*, *358*, 210-214.
[90] Priya James, H., John, R., Alex, A., & Anoop, K. R. (2014). Smart polymers for the controlled delivery of drugs - a concise overview. *Acta Pharm Sin B*, *4*(2), 120-127. https://doi.org/10.1016/j.apsb.2014.02.005
[91] Quan, M. H., Yang, B. W., Wang, J. X., Yu, H. F., & Cao, X. Y. (2018). Simultaneous Microscopic Structure Characteristics of Shape-Memory Effects of Thermo-Responsive Poly(vinylidene fluoride-co-hexafluoropropylene) Inverse Opals. *Acs Applied Materials & Interfaces*, *10*(4), 4243-4249. <Go to ISI>://WOS:000424728800122
[92] Rafsanjani, A., Zhang, Y., Liu, B., Rubinstein, S. M., & Bertoldi, K. (2018). Kirigami skins make a simple soft actuator crawl. *Sci Robot*, *3*(15). https://doi.org/10.1126/scirobotics.aar7555
[93] Rhon, D. I., Greenlee, T. A., Cook, C. E., Westrick, R. B., Umlauf, J. A., & Fraser, J. J. (2021). Fractures and Chronic Recurrence are Commonly Associated with Ankle Sprains: a 5-year Population-level Cohort of Patients Seen in the US Military Health System. *International Journal of Sports Physical Therapy*, *16*(5), 1313.
[94] Rodrigues, G. V., Fonseca, L. M., Savi, M. A., & Paiva, A. (2017). Nonlinear dynamics of an adaptive origami-stent system. *International Journal of Mechanical Sciences*, *133*, 303-318. https://doi.org/https://doi.org/10.1016/j.ijmecsci.2017.08.050

[95] Scalet, G. (2020). Two-way and multiple-way shape memory polymers for soft robotics: An overview. Actuators,
[96] Scarpa, F., & Tomlin, P. (2000). On the transverse shear modulus of negative Poisson's ratio honeycomb structures. *Fatigue & Fracture of Engineering Materials & Structures*, *23*(8), 717-720.
[97] Schenk, M., & Guest, S. D. (2013). Geometry of Miura-folded metamaterials. *Proc Natl Acad Sci U S A*, *110*(9), 3276-3281. https://doi.org/10.1073/pnas.1217998110
[98] Sevin, A., BAYILMIŞ, C., ERTÜRK, İ., EKİZ, H., & Karaca, A. (2016). Design and implementation of a man-overboard emergency discovery system based on wireless sensor networks. *Turkish Journal of Electrical Engineering & Computer Sciences*, *24*(3), 762-773.
[99] Shyu, T. C., Damasceno, P. F., Dodd, P. M., Lamoureux, A., Xu, L., Shlian, M., Shtein, M., Glotzer, S. C., & Kotov, N. A. (2015). A kirigami approach to engineering elasticity in nanocomposites through patterned defects. *Nat Mater*, *14*(8), 785-789. https://doi.org/10.1038/nmat4327
[100] Siegler, S., Block, J., & Schneck, C. D. (1988). The mechanical characteristics of the collateral ligaments of the human ankle joint. *Foot Ankle*, *8*(5), 234-242. https://doi.org/10.1177/107110078800800502
[101] Silverberg, J. L., Na, J. H., Evans, A. A., Liu, B., Hull, T. C., Santangelo, C. D., Lang, R. J., Hayward, R. C., & Cohen, I. (2015). Origami structures with a critical transition to bistability arising from hidden degrees of freedom. *Nat Mater*, *14*(4), 389-393. https://doi.org/10.1038/nmat4232
[102] SOBEL, M., GEPPERT, M. J., & WARREN, R. F. (1993). Chronic ankle instability as a cause of peroneal tendon injury. *Clinical Orthopaedics and Related Research®*, *296*, 187-191.
[103] Song, Z., Ma, T., Tang, R., Cheng, Q., Wang, X., Krishnaraju, D., Panat, R., Chan, C. K., Yu, H., & Jiang, H. (2014). Origami lithium-ion batteries. *Nature communications*, *5*(1), 1-6.
[104] Song, Z., Wang, X., Lv, C., An, Y., Liang, M., Ma, T., He, D., Zheng, Y. J., Huang, S. Q., Yu, H., & Jiang, H. (2015). Kirigami-based stretchable lithium-ion batteries. *Sci Rep*, *5*, 10988. https://doi.org/10.1038/srep10988
[105] Surjadi, J. U., Gao, L., Du, H., Li, X., Xiong, X., Fang, N. X., & Lu, Y. (2019). Mechanical Metamaterials and Their Engineering Applications. *Advanced Engineering Materials*, *21*(3). https://doi.org/10.1002/adem.201800864
[106] Swolfs, Y., & Pinho, S. T. (2019). 3D printed continuous fibre-reinforced composites: Bio-inspired microstructures for improving the translaminar fracture toughness. *Composites Science and Technology*, *182*, 107731.
[107] Tang, H.-W., Chou, W.-D., & Chen, L.-W. (2017). Wave propagation in the polymer-filled star-shaped honeycomb periodic structure. *Applied Physics A*, *123*(8). https://doi.org/10.1007/s00339-017-1124-x
[108] Taser, F., Shafiq, Q., & Ebraheim, N. A. (2006). Anatomy of lateral ankle ligaments and their relationship to bony landmarks. *Surg Radiol Anat*, *28*(4), 391-397. https://doi.org/10.1007/s00276-006-0112-1
[109] Tatiparthi, S. R., De Costa, Y. G., Whittaker, C. N., Hu, S. H., Yuan, Z. G., Zhong, R. Y., & Zhuang, W. Q. (2021). Development of radio-frequency identification (RFID) sensors

suitable for smart-monitoring applications in sewer systems. *Water Research*, *198*. <Go to ISI>://WOS:000651349000003
[110] Teyhen, D. S., Goffar, S. L., Shaffer, S. W., Kiesel, K., Butler, R. J., Tedaldi, A.-M., Prye, J. C., Rhon, D. I., & Plisky, P. J. (2018). Incidence of Musculoskeletal Injury in US Army Unit Types: A Prospective Cohort Study. *Journal of Orthopaedic & Sports Physical Therapy*, *48*(10), 749-757. https://doi.org/10.2519/jospt.2018.7979
[111] Theocaris, P. S., Stavroulakis, G. E., & Panagiotopoulos, P. D. (1997). Negative Poisson's ratios in composites with star-shaped inclusions: a numerical homogenization approach. *Archive of Applied Mechanics*, *67*(4), 274-286. https://doi.org/https://doi.org/10.1007/s004190050117
[112] Toms, S. R., Dakin, G. J., Lemons, J. E., & Eberhardt, A. W. (2002). Quasi-linear viscoelastic behavior of the human periodontal ligament. *Journal of biomechanics*, *35*(10), 1411-1415.
[113] Torp, D. M., Thomas, A. C., Hubbard-Turner, T., & Donovan, L. (2022). Effects of gait training with auditory biofeedback on biomechanics and talar cartilage characteristics in individuals with chronic ankle instability: A randomized controlled trial. *Gait & Posture*, *95*, 1-8.
[114] van Manen, T., Janbaz, S., & Zadpoor, A. A. (2017). Programming 2D/3D shape-shifting with hobbyist 3D printers. *Mater Horiz*, *4*(6), 1064-1069. https://doi.org/10.1039/c7mh00269f
[115] van Ochten, J. M., Mos, M. C., van Putte-Katier, N., Oei, E. H., Bindels, P. J., Bierma-Zeinstra, S. M., & van Middelkoop, M. (2014). Structural abnormalities and persistent complaints after an ankle sprain are not associated: an observational case control study in primary care. *British Journal of General Practice*, *64*(626), e545-e553.
[116] Waterman, B. R., Owens, B. D., Davey, S., Zacchilli, M. A., & Belmont, P. J. (2010). The epidemiology of ankle sprains in the United States. *J Bone Joint Surg Am*, *92*(13), 2279-2284. https://doi.org/10.2106/JBJS.I.01537
[117] Wikstrom, E. A., Cain, M. S., Chandran, A., Song, K., Regan, T., Migel, K., & Kerr, Z. Y. (2021). Lateral Ankle Sprain and Subsequent Ankle Sprain Risk: A Systematic Review. *J Athl Train*, *56*(6), 578-585. https://doi.org/10.4085/1062-6050-168-20
[118] Willems, T. M., Witvrouw, E., Delbaere, K., Mahieu, N., De Bourdeaudhuij, L., & De Clercq, D. (2005). Intrinsic risk factors for inversion ankle sprains in male subjects: a prospective study. *The American journal of sports medicine*, *33*(3), 415-423.
[119] Wu, Z. L., Moshe, M., Greener, J., Therien-Aubin, H., Nie, Z. H., Sharon, E., & Kumacheva, E. (2013). Three-dimensional shape transformations of hydrogel sheets induced by small-scale modulation of internal stresses. *Nature communications*, *4*. <Go to ISI>://WOS:000318873900040
[120] Xiao, Y. Y., Jiang, Z. C., Tong, X., & Zhao, Y. (2019). Biomimetic locomotion of electrically powered "Janus" soft robots using a liquid crystal polymer. *Advanced Materials*, *31*(36), 1903452.
[121] Xin, C., Jin, D., Hu, Y., Yang, L., Li, R., Wang, L., Ren, Z., Wang, D., Ji, S., & Hu, K. (2021). Environmentally Adaptive Shape-Morphing Microrobots for Localized Cancer Cell Treatment. *ACS nano*, *15*(11), 18048-18059.
[122] Xu, K., Lu, Y., Honda, S., Arie, T., Akita, S., & Takei, K. (2019). Highly stable kirigami-structured stretchable strain sensors for perdurable wearable electronics. *Journal of Materials Chemistry C*, *7*(31), 9609-9617.

[123] Yan, Z., Zhang, F., Wang, J., Liu, F., Guo, X., Nan, K., Lin, Q., Gao, M., Xiao, D., & Shi, Y. (2016). Controlled mechanical buckling for origami-inspired construction of 3D microstructures in advanced materials. *Advanced Functional Materials*, *26*(16), 2629-2639.
[124] Yang, H., Leow, W. R., Wang, T., Wang, J., Yu, J. C., He, K., Qi, D. P., Wan, C. J., & Chen, X. D. (2017). 3D Printed Photoresponsive Devices Based on Shape Memory Composites. *Advanced Materials*, *29*(33). <Go to ISI>://WOS:000408933600018
[125] Yong, K., De, S., Hsieh, E. Y., Leem, J., Aluru, N. R., & Nam, S. (2020). Kirigami-inspired strain-insensitive sensors based on atomically-thin materials. *Materials Today*, *34*, 58-65. https://doi.org/https://doi.org/10.1016/j.mattod.2019.08.013
[126] Zarek, M., Mansour, N., Shapira, S., & Cohn, D. (2017). 4D printing of shape memory-based personalized endoluminal medical devices. *Macromolecular rapid communications*, *38*(2), 1600628.
[127] Zarifi, M. H., Deif, S., & Daneshmand, M. (2017). Wireless passive RFID sensor for pipeline integrity monitoring. *Sensors and Actuators a-Physical*, *261*, 24-29. <Go to ISI>://WOS:000404494800004
[128] Zhang, H., Guo, X., Wu, J., Fang, D., & Zhang, Y. (2018). Soft mechanical metamaterials with unusual swelling behavior and tunable stress-strain curves. *Science advances*, *4*(6), eaar8535.
[129] Zhang, Q., Yan, D., Zhang, K., & Hu, G. K. (2015). Pattern Transformation of Heat-Shrinkable Polymer by Three-Dimensional (3D) Printing Technique. *Scientific Reports*, *5*. <Go to ISI>://WOS:000351137000004
[130] Zhao Dubuc, Y., Mazzone, B., Yoder, A. J., Esposito, E. R., Kang, T. H., Loh, K. J., & Farrokhi, S. (2022). Ankle sprain bracing solutions and future design consideration for civilian and military use. *Expert Review of Medical Devices*, *19*(2), 113-122.
[131] Zhao, Q., Wang, J., Cui, H., Chen, H., Wang, Y., & Du, X. (2018). Programmed shape-morphing scaffolds enabling facile 3D endothelialization. *Advanced Functional Materials*, *28*(29), 1801027.
[132] Zhao, W., Huang, Z., Liu, L., Wang, W., Leng, J., & Liu, Y. (2021). Porous bone tissue scaffold concept based on shape memory PLA/Fe3O4. *Composites Science and Technology*, *203*, 108563.
[133] Zirbel, S. A., Lang, R. J., Thomson, M. W., Sigel, D. A., Walkemeyer, P. E., Trease, B. P., Magleby, S. P., & Howell, L. L. (2013). Accommodating Thickness in Origami-Based Deployable Arrays1. *Journal of Mechanical Design*, *135*(11). https://doi.org/10.1115/1.4025372